Dissertation
submitted to the
Combined Faculties of the Natural Sciences and Mathematics
of the Ruperto-Carola-University of Heidelberg, Germany
for the degree of
Doctor of Natural Sciences

Put forward by
Tim Manfred Tugendhat
born in: Ulm
Oral examination: 16 May 2018

On the Impact and Usefulness of Intrinsic Alignments of Galaxies in a Composite Model on Weak Lensing in Tomographic Surveys

Referees: Prof. Dr. Björn Malte Schäfer
Prof. Dr. Volker Springel

Über den Einfluss und die Nützlichkeit von intrinsischen Ausrichtungen von Galaxien in einem gemischten Modell auf tomographische Messungen des schwachen Gravitationslinseneffektes

Zukünftige Messungen des schwachen Gravitationslinseneffektes werden wegen ihrer beeindruckenden statistischen Genauigkeit die systematischen Fehler mit größter Sorgfalt behandeln müssen.
Insbesondere sind intrinsische Ausrichtungseffekte (IA) der Galaxien, welche Elliptizitätskorrelationen zwischen Galaxien verursachen, ununterscheidbar vom Gravitationslinseneffekt. Ich stelle zwei bereits etablierte Modelle für IA-Effekte vor und werde diese den physikalischen Eigenschaften von zwei Galaxientypen, nämlich Spiralgalaxien und elliptischen Galaxien, zuordnen.
Ich bestimmte ihre relativen Amplituden zum Gravitationslinsen-Spektrum und bei einem realistischen Mischverhältnis der Modelle zeige ich den Einfluss von IA-Effekten auf eine tomographische Messung des schwachen Linseneffektes, wie sie mit dem Euclid-Satelliten möglich sein wird. Ich zeige, dass IA-Effekte signifikante systematische Fehler in geplanten Messkampagnen verursachen werden, besonders in den Parametern Ω_m, σ_8 h und n_s.
Desweiteren führe ich eine Methode vor, um mithilfe der Galaxie-Farbinformationen die Messung in rote und blaue Galaxien zu unterteilen und so das IA-Signal zu unterdrücken. Diese Methode kann auch benutzt werden, um stattdessen das Gravitationslinsensignal zu unterdrücken, was eine alleinige Behandlung eines IA-Signals ermöglicht, um beispielsweise ihre (relativen) Amplituden festzustellen. Zuletzt zeige ich eine Möglichkeit auf, das Signal des Modells für elliptische Galaxien und das Gravitationslinsensignal als gemeinsame Informationsquelle zu benutzen, um Abweichungen von der allgemeinen Relativitätstheorie (Gravitational Slip) quantitativ einzugrenzen und so die Ausrichtungseffekte als Signal zu nutzen anstatt sie als Rauschen in den Daten zu betrachten.

On the Impact and Usefulness of Intrinsic Alignments of Galaxies in a Composite Model on Weak Lensing in Tomographic Surveys

Future weak lensing surveys will be too precise for their own good: due to their impressive statistical precision, their systematics must be treated with extreme care.
In particular, intrinsic alignments (IA) of galaxies, which cause galaxy ellipticities to be correlated, are indistinguishable from gravitational lensing. I present two established models for IAs and will link them to the physical properties of two galaxy morphologies, namely spiral and elliptical galaxies.
I determine their amplitudes relative to the lensing spectrum and a realistic mix of galaxies for the model. Thus utilised, I predict the impact of IAs on a Euclid-like tomographic survey and its inferences on a cosmological parameter set. I will show that IAs will give rise to significant systematic errors (biases) in future surveys, particularly in the parameters Ω_m, σ_8 h and n_s.
Furthermore, I present a method for suppressing the IA signal by using colour information and separating the survey into subsamples of blue and red galaxies. This method can also be used to suppress the lensing signal instead, enabling the treatment of just IAs, e.g. for fitting their (relative) amplitudes. Finally, I will show a method of constraining deviations from General Relativity (Gravitational Slip) by using the model for elliptical galaxies alone and leveraging its signal against the one from weak lensing, thus promoting intrinsic alignments from noise to signal.

"The suppression of uncomfortable ideas may be common in religion and politics, but it is not the path to knowledge; it has no place in the endeavor of science."

Carl Sagan, Cosmos (1980)

Contents

1 Introductory Remarks

Only recently – and with considerable effort due to the complexity of the task – have gravitational waves been observed directly (Abbott et mult., 2016). The sheer amount of work and resources that have gone into building gravitational wave observatories over the last decades is stunning. The findings are in perfect agreement with predictions made more than a hundred years ago and are only the latest in a long history of successful substantiation of the underlying theory. Alongside the observed perihelion shift of Mercury, the concept of a gravitational lens was among the first empirical tests for Albert Einstein's geometric theory of gravity, General Relativity (Einstein, 1915; Einstein, 1916).

Einstein's theory would face this challenge so early in its development that he only published the correct predictions after the first expedition led by Erwin Finlay-Freundlich to measure this effect had had to return empty-handed (Hentschel, 1994) from Russia. Immediately after the interruption caused by what would later be called the first World War, astronomical observations by a British team would find the predictions made by German-born Einstein working in Berlin to be accurate (Dyson et al., 1920).

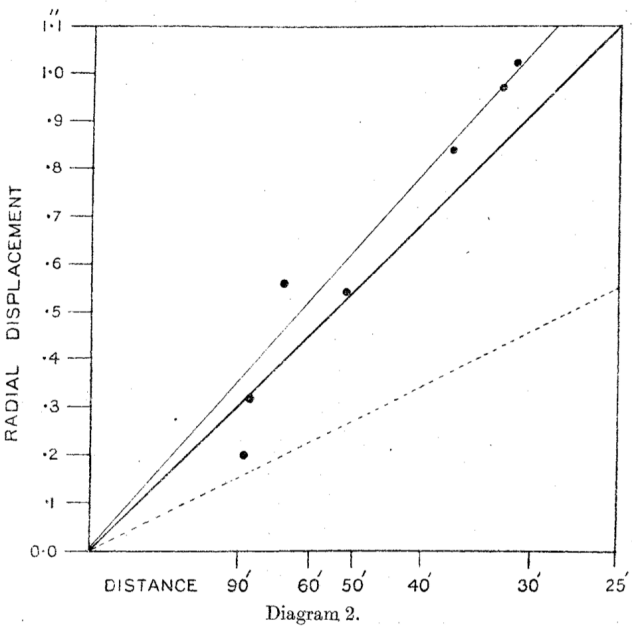

Figure 1.1: Radial displacement of background stars caused by the Sun's gravity.
Thick line: prediction by General Relativity, dotted line: prediction by Newtonian gravity, thin line: linear regression of the data.
Copied from Dyson et al. (1920).

From then, the success story of General Relativity is essentially unbroken until today, almost 100 years after Eddington's expedition; the first exact solutions to the field equations were published as early as 1916 (Schwarzschild, 1916) and the following 20 years saw the development of the basis of today's physical cosmology when the expansion of the Universe was starting to become apparent (Friedmann, 1922; Lemaître, 1927; Hubble, 1929). The next big leap in cosmology came when the cosmic microwave background radiation (CMB) was discovered (Penzias & Wilson, 1965), the relic radiation of a hot big bang that had long been speculated about (Regener, 1933; Finlay-Freundlich, 1954; Gamow, 1961; Dicke et al., 1965).

The years following saw the discovery that the rotation curves of galaxies weren't what people expected from Newtonian mechanics (Rubin & Ford, 1970), which could be explained by dark matter, which had been speculated about earlier (Zwicky, 1933). Gravitational lensing as a viable tool for cosmology re–surfaced when the first gravitationally lensed object, a quasar, was discovered (Walsh et al., 1979) and people started trying to probe the Universe with it (e.g. Falco et al., 1985). Weak gravitational lensing has first been successfully measured around galaxy clusters (Tyson et al., 1990), and since been used to deliver more evidence for Dark

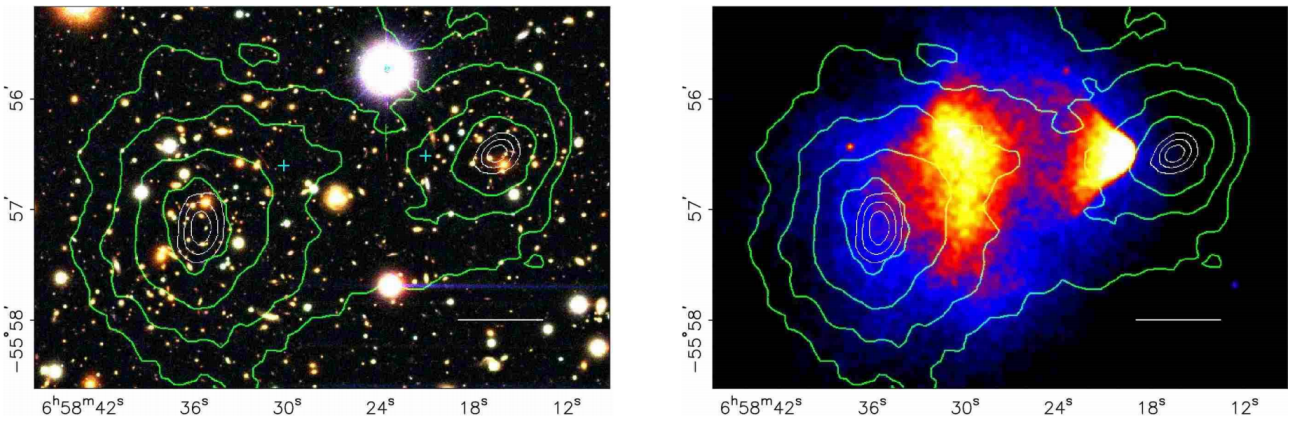

Figure 1.2: The Bullet cluster illustrates that most of the gravitational mass is not in the baryonic component of the galaxy clusters.
Left panel: Bullet cluster in visible light with projected mass density on top, right panel: Bullet cluster in X-ray with projected mass density on top. Copied from Clowe et al. (2006)

Matter in intragalactic dynamics. The so–called 'smoking gun', the Bullet cluster (Clowe et al., 2006), is as close to detection of dark matter can get without being a direct detection. The collaborators found that the centres of mass of two colliding galaxy clusters was in fact not where most of the visible material was (hot X-ray gas) but rather with the collisionless stellar population. Since much more mass is expected to be in the hot component, only a collisionless dark matter that is being traced by the stars can explain this phenomenon. Most alternative theories of gravitation cannot explain this behaviour entirely without dark matter.

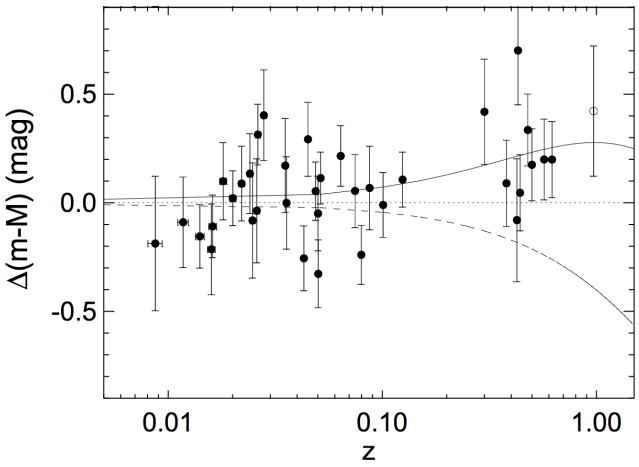

Figure 1.3: Original plot of SNIa data distance modulus against redshift relative to a universe with negative curvature (dotted line, $\{\Omega_m = 0.2, \Omega_\Lambda = 0.0\}$), a flat matter-only universe (dashed line $\{\Omega_m = 1.0, \Omega_\Lambda = 0.0\}$), and the best fit $\{\Omega_m = 0.24, \Omega_\Lambda = 0.76\}$ as solid line. Copied from Riess et al. (1998)

The observed accelerated expansion of the Universe (Riess et al., 1998; Perlmutter et al., 1999) in the late 90s brought back speculation about a cosmological constant that Einstein himself had ruled out when he accepted the expansion of the Universe. Taking the light curves of Supernovae Ia, independent groups had shown that they can be standardised in luminosity, i.e. used as standard candles in order to measure the luminosity distance to much greater distances than before. What they had found was that the standard candles were dimmer than expected in a mere matter–dominated universe and not even a negative curvature of space could explain such an effect without raising other questions. Since the discovery of accelerated expansion in the late cosmos, there have been attempts at explaining this on both sides of the Einstein equation: Either by a cosmological constant, a scalar degree of freedom, which the standard theory of general relativity allows (Lovelock, 1971, 1972), or by a dynamical substance called Dark Energy, which can be described by a scalar field (e.g. Wetterich, 1988). The other side of the Einstein equation would be to change the rule for deriving the Einstein tensor, i.e. changing the law of gravity. So far, however, there aren't any strong indications that general relativity might be incomplete as a description for gravitation. To-

day, the standard model for cosmology is ΛCDM, i.e. a cosmological constant coupled with cold dark matter. Cold dark matter takes its name from having no thermal energy, such that the clustering scales can be almost arbitrarily small (Blumenthal et al., 1984). Strong support for ΛCDM today comes from probes of the cosmic microwave background, such as Planck[1]. When the Planck collaboration published their first results (Planck Collaboration, 2013), most of the community was rather underwhelmed, as apart from a slightly lower Hubble constant than other probes, there had not been a big revolution. Today, this is seen as another success of the cosmological standard model. The first astronomical N-body simulations were carried out in the 1960s (von Hoerner, 1960, 1963), but the method came to fruition much later; today's awesome simulation methods and results have arguably become a third pillar in astrophysics, beside observation and theory. Since the Millennium run (Springel et al., 2005), there has been an explosive growth of codes and simulations, with detailed galaxy formation models, like the Eagle project[2], Illustris[3], and most recently Illustris TNG (see Fig. (1.5)). Some simulations specialize on post-Newtonian corrections, such as weak field gravity in order to simulate vector modes as well (Adamek et al., 2013). The main focus of this work is on the impact of intrinsic alignments (IAs) on Euclid[5], an upcoming weak lensing survey. Intrinsic alignments are correlations in galaxy shapes that manifest themselves physically, other than weak gravitational lensing, which is an observer-dependent effect. The issue with alignment is that it is principally undistinguishable from weak gravitational lensing effects and thus might significantly alter the inferences of cosmological parameter sets from weak lensing data. To model, understand, and correct for those alignment effects is a challenge for future weak gravitational lensing surveys that have a high statistical precision.

It isn't hard to argue that Euclid is to cosmic weak lensing what WMAP[6] was to the cosmic microwave background; after initial measurements by other probes and small-scale ground-based observation, a dedicated satellite is launched that will surpass all other previous surveys in terms of observational scale and thus inferred parameter precision. WMAP had to deal with secondary anisotropies in the cosmic microwave background (Aghanim et al., 2008), like the Sunyaev-Zel'dovich-effect (Sunyaev & Zeldovich, 1970, 1980), which locally increases the photon energies through inverse Compton scattering with hot intracluster gas. Nowadays, the SZ effect is used to identify galaxy clusters and can be removed from the CMB survey by masking. Intrinsic alignments are very similarly related to a weak lensing survey: they locally change the ellipticity correlations and thus are a nuisance in a survey for weak lensing. However, maybe their effects, once well enough understood and modelled, be used to gain new insights about galaxy formation and evolution or even gravitation. In order to put intrinsic alignments and weak lensing into the context of cosmology, I will spend the first part of this thesis introducing many concepts

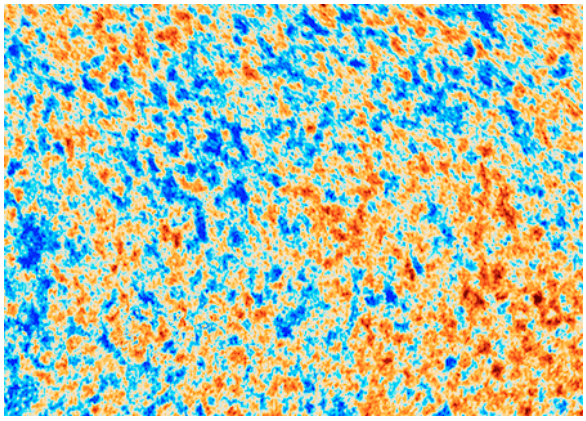

Figure 1.4: Temperature fluctuations in the CMB; the typical Temperature differences are of the order of 10^{-5}. Copyright: ESA[4]

[1] http://sci.esa.int/planck/
[2] http://icc.dur.ac.uk/Eagle/
[3] http://www.illustris-project.org/
[4] Source: https://www.cosmos.esa.int/web/planck/picture-gallery
[5] https://www.euclid-ec.org
[6] https://map.gsfc.nasa.gov/

and results from cosmology first. Then, I will describe weak lensing in more detail, including its strengths and weaknesses in inferring cosmological parameters and show a formalism to quantify just that.

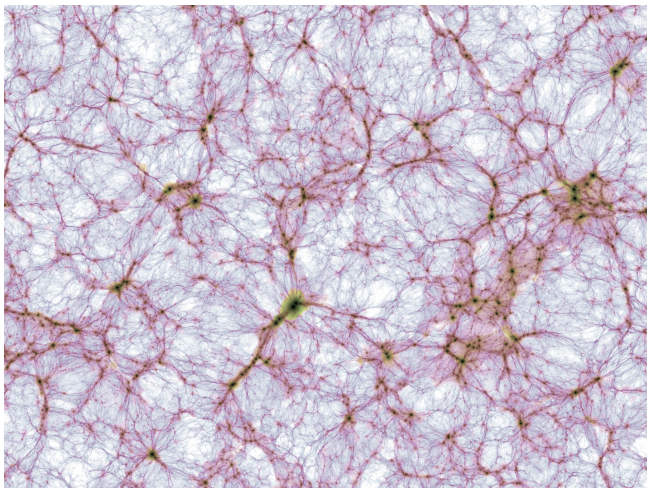

Figure 1.5: Projected gas density in the TNG300 simulation showing the baryons tracing the cosmic web. Copyright: the IllustrisTNG project[7]

From there, two physically motivated models for intrinsic alignments for each elliptical galaxies and spiral galaxies will be introduced and described in detail. I will motivate choices for their amplitudes from previous literature and through a determination of one of the alignment parameters. I will then calculate their resulting correlation functions and angular spectra and compare those with weak gravitational lensing. The parameter estimation of weak lensing is shown to be significantly off target when the intrinsic alignment spectra of the two models are introduced. I will then present a method to disentangle intrinsic alignments and weak lensing using the colour information of the galaxies – as redder galaxies tend to be ellipticals and bluer galaxies tend to be spirals, we can apply the models to each of the colour sets separately. In rotating the base for one of those colour sets, we can either maximise the weak lensing signal with respect to intrinsic alignments or minimise it in order to get a pure intrinsic alignment signal, which could then be fitted with the free parameters. Lastly, I will show a way of using the fact that elliptical galaxies are influenced by the Newtonian potential while lensing acts through the Weyl potential to constrain gravitational slip, i.e. test general relativity.

[7] source: `http://www.tng-project.org/media/`

Part I

Cosmological Background and Weak Gravitational Lensing

2 Cosmology

Physical cosmology is a relatively young field compared to others in physics. Even though there have been both remarkable and deep insights about the Universe before Einstein's time (e.g. Olbers' paradox[1]), the real revolution came with the theory of General Relativity (Einstein, 1915; Einstein, 1916) and its implications about the universe (Einstein, 1911, 1917). In the century since, cosmology has grown from a speculative endeavour to a precise and accurate field of the physical sciences.

In fact, depending on who one is talking to, cosmology's current ΛCDM paradigm competes with the incredibly successful Standard Model of particle physics for the shorthand 'Standard Model'.

The picture that this standard model – as I will refer to ΛCDM from now on – paints, is bleak and exceptionally wasteful. According to it, we live in a 13.7 billion years old Cosmos where the so-called baryonic matter, everything that the 'other' standard model so aptly describes: nucleons, electrons, photons, neutrinos, and so on, makes up about five per cent of the energy density of Everything. The rest is literally dark, namely about 27 per cent Cold Dark Matter (Davis et al., 1985, as opposed to Warm or Hot Dark Matter that feature thermal motion) and 68 per cent Dark Energy or cosmological constant Λ (Planck Collaboration & Ade et mult., 2016a). The model supposes that our place in the universe is not special. At least not spatially special, since the universe is postulated to be homogeneous on large scales. We happen to[2] live at an interesting time, however: Had our civilisation existed about 7 billion years earlier (or about at half our home planet's current age, so not entirely unrealistic in terms of cosmic age) we likely would have never known about a cosmological constant or Dark Energy.

In this chapter, I will attempt to quickly introduce the most important ideas, concepts, tools, and vocabulary of modern cosmology for this particular work. If not explicitly pointed out otherwise, the concepts introduced in this chapter are taken from standard books and reviews – particularly Peacock (2003); Dodelson (2006); Amendola & Tsujikawa (2010); Bartelmann (2010) for cosmology in general, and Bartelmann & Schneider (2001a) for gravitational (weak) lensing. There, the reader also has the opportunity to delve deeper into the matter if so inclined.

2.1 Homogeneous Cosmology

The starting point for every introduction in cosmology consists of formulating the cosmological principle:
On large enough scales, the universe is spatially homogeneous and isotropic.

Homogeneity would be broken if there were a special place in the universe, say a centre. But postulating homogeneity is in alignment with the ongoing trend of debunking human exceptionalism: from geocentrism via heliocentrism to having no centre at all. Isotropy makes a similar statement about directionality. The universe doesn't have a preferred direction, meaning that the universe looks (roughly) the same wherever we choose to look. An example that would break isotropy would be assuming a global rotation of the universe around an

[1] Olbers' paradox states that if the universe is infinitely old and infinitely large with an infinite number of stars, the night sky should be bright as day, since our eyes would always hit a star, no matter where we are looking. Obviously, this neglects absorption and other effects

[2] This is up for debate

axis, which would start designating different directions.

Evidence of isotropy and homogeneity may be taken from an abundance of In the framework of general relativity, a metric theory of gravity that characterises spacetime and its properties using the line element $\mathrm{d}s^2 = g_{\mu\nu}\mathrm{d}x^\mu \mathrm{d}x^\nu$, mathematically an invariant under diffeomorphisms and intuitively a measure for the infinitesimal distance between two points.

Its defining part is the metric tensor, or metric, $g_{\mu\nu}$. It is possible to encode the cosmological principle into a metric, namely the Friedmann-Lemaître-Roberton-Walker (hereafter FLWR) metric (Friedmann, 1922; Lemaître, 1927; Robertson, 1935; Walker, 1937), which gives the line element

$$\mathrm{d}s^2 = -c^2\mathrm{d}t^2 + a(t)\left[\mathrm{d}\chi^2 + f_K^2(\chi)\left(\mathrm{d}\theta^2 + \sin^2(\theta)\,\mathrm{d}\phi^2\right)\right]. \tag{2.1}$$

In this line element, the entire spatial part is scaled by a function $a(t)$, which only depends on the time t, as temporal homogeneity and isotropy are not postulated. Commonly it is normalised to $a_0 = 1$ today. The part in the brackets is called co-moving as it scales in its entirety with $a(t)$. There is no dependence on any of the angles (θ, ϕ), so isotropy is ensured. The radial distance χ however, appears in $f_K(\chi)$. This function sets the overall spatial geometry of the universe described by this metric. The universe is called open, flat, or closed, if its curvature K is negative, zero, or positive, respectively. In particular,

$$f_K(\chi) = \begin{cases} \sqrt{-K^{-1}}\sinh(\sqrt{-K}\chi) & \text{if } K < 0 \text{ (open)}, \\ \chi & \text{if } K = 0 \text{ (flat)}, \\ \sqrt{K^{-1}}\sin(\sqrt{K}\chi) & \text{if } K > 0 \text{ (closed)}. \end{cases} \tag{2.2}$$

Evidently, K is measured in units of length squared, just like the Gaussian curvature. It can be easily imagined what happens to two radial lines in those three geometries: In flat geometry, which corresponds to Euclidian geometry, the space between the lines will increase at a constant rate proportional to χ. In a closed geometry, this increase is smaller due to the fact that $\sin(x)$ around $x = 0$ is always smaller or equal to x. The opposite is true for an open geometry. Here, the two lines will diverge at a faster pace than in flat space, because $\sinh(x)$ grows faster than x.

Here it is already apparent that in the FLRW-metric that there is a separation of the temporal and spatial dimensions. In particular, there is a global time coordinate t, which means that spacetime can be foliated into three-dimensional subspaces of equal coordinate time.

In order to describe the evolution of the metric, we plug it into the Einstein field equations,

$$G_{\mu\nu} - \Lambda g_{\mu\nu} = \frac{8\pi G}{c^4} T_{\mu\nu}, \tag{2.3}$$

where $G_{\mu\nu}$ is called Einstein Tensor, a complex item calculated from second derivatives of $g_{\mu\nu}$, Λ the cosmological constant, a free scalar, and $T_{\mu\nu}$ the stress-energy tensor.

Plugging in equation (2.1) into equation (2.3) and assuming the stress-energy tensor to be that of a perfect fluid, one finds the Friedmann equations,

$$H^2 = \left(\frac{\dot{a}}{a}\right)^2 = \frac{8\pi G}{3}\rho - \frac{Kc^2}{a^2} + \frac{\Lambda c^2}{3}, \tag{2.4}$$

$$\frac{\ddot{a}}{a} = -\frac{4\pi G}{3}\left(\rho + \frac{3p}{c^2}\right) + \frac{\Lambda c^2}{3}. \tag{2.5}$$

The Friedmann equations describe the evolution of the scale factor a. Here, H is the Hubble parameter and ρ and p are the density and pressure respectively that enter the equation through $T_{\mu\nu}$.
It is customary to introduce the equation of state parameter w as

$$w = p/\rho c^2, \tag{2.6}$$

which is often just called equation of state. Furthermore, it is possible to absorb Λ into the density and pressure by setting $(\rho,p) \to (\rho - \rho_\Lambda, p - p_\Lambda)$ with

$$\rho_\Lambda = \frac{\Lambda c^2}{8\pi G} \text{ and } p_\Lambda = -\frac{\Lambda c^4}{8\pi G}. \tag{2.7}$$

The Friedmann equations (2.4 and 2.5) can be combined into the adiabatic equation

$$\frac{\mathrm{d}}{\mathrm{d}t}\left(a^3\rho c^2\right) + p\frac{\mathrm{d}}{\mathrm{d}t}\left(a^3\right) = 0, \tag{2.8}$$

which bears resemblance to the first law of thermodynamics in an adiabatic process ($\Delta U + p\mathrm{d}V = 0$). Alternatively this can be derived by requiring a divergence-free stress-energy tensor T, $\nabla_\nu T_{\mu\nu} = 0$ where ∇_μ denotes the covariant derivative. This is not necessarily what we would call classical energy conservation, as ∇_μ is sensitive to geometry as well. It becomes apparent by the scale factor a appearing in the above equation; it was originally part of the metric.
Integrating over equation (2.8) gives an expression of the density $\rho(a)$ using the aforementioned equation of state w,

$$\rho(a) = \rho_0\, a^{-3(1+w)}. \tag{2.9}$$

This equation is scaled such that at present (i.e. $a = 1$), $\rho = \rho_0$. Furthermore, a constant w was implied in its derivation. It will be noted lated that favouring Dark Energy instead of a cosmological constant will lead to a running $w(a)$, in which case the equation would read

$$\rho(a) = \rho_0\, \exp\left\{-3\int_1^a \mathrm{d}\ln(a')\ (1 + w(a'))\right\}. \tag{2.10}$$

Already, it can be derived how different forms of matter (expressed as perfect fluids) will dilute as the universe expands. In particular, the most commonly referred to fluids in this are

- highly relativistic matter with $w_\mathrm{r} = 1/3$, since $p_\mathrm{r} = 3\rho_\mathrm{r}c^2$,
  implying $\rho_\mathrm{r} \propto a^{-4}$,

- ordinary matter[3], sometimes called 'dust' in the literature, which has $w_\mathrm{m} = 0$, since $p_\mathrm{m} = 0$,
  implying $\rho_\mathrm{m} \propto a^{-3}$,

- curvature, which can also be associated with a density, with $w_K = -1/3$,
  implying $\rho_K \propto a^{-2}$,

[3]This includes Dark Matter as well as baryons

– cosmological constant, with $w_\Lambda = -1$, since $p_\Lambda = -\rho_\Lambda c^2$ (see equation (2.7)), implying the special case $\rho_\Lambda = \text{const.}$

In general, cosmologists call anything with $w < -1/3$ Dark Energy, where w is allowed to vary in time. In that sense, Λ is a static Dark Energy with $w = -1$. Extreme cases, such as 'phantom energy' ($w < -1$) will not be discussed.

There are many interesting points to make here, one of which is that matter is diluted as a^3, whereas photons are diluted with an additional factor of a. There are many ways to explain this difference intuitively. A usual explanation found in many textbooks is that as the photons get diluted with a^3, another channel for them to be influenced by expansion is their wavelength λ, which is stretched by an additional factor a. Thus the redshift,

$$z = \frac{\lambda_{\text{obs}} - \lambda_{\text{em}}}{\lambda_{\text{em}}}, \tag{2.11}$$

is defined. An example would be if a photon that was originally emitted at $\lambda_{\text{em}} = 4000\,\text{Å}$ is observed at $\lambda_{\text{obs}} = 8000\,\text{Å}$, its redshift is $z = 1$. In particular, redshift can be related to the scale factor a in an expanding Friedmann universe, given an observing time (today) and an observed wavelength λ_{obs} of a source of known emission wavelength λ_{em}, it is easy to determine what the scale factor must have been at the time of emission, namely

$$a(z) = \frac{1}{1+z}. \tag{2.12}$$

Therefore, in the case of $z = 1$, the scale factor must have been $a = \frac{1}{2}$, meaning the universe was one eighth of its current physical size at the time of emission.

But there is also another way of looking at the two different ways photons and matter particles are treated differently in general relativity: while matter particles travel in a timelike fashion, photons follow nullgeodesics. They each 'feel' different parts of the metric: timelike particles will only experience temporal curvature, which reverts to the Newtonian potential in the case of weak fields and small velocities, whereas photons have both temporal and spatial curvature to source their gravitational interaction.

An illustrative example of this is the stress–energy tensor for a perfect fluid, $T^\mu_\nu = \text{diag}\left(-\rho c^2, p, p, p\right)$, where matter will only have a non–vanishing 00 component. Only the density ρ sources gravitational fields in the case of matter.

This is also precisely why Newtonian physics cannot be used to arrive at the correct predictions for the gravitational lensing effect, which will be introduced in section 2.5.

Setting $K = 0$ for the moment, we can define the critical density ρ_{crit} by solving equation (2.4) for ρ,

$$\rho_{\text{crit}} = \frac{3H(a)^2}{8\pi G}. \tag{2.13}$$

This gives a natural density unit for a Friedmann universe. The critical density today $\rho_{\text{crit},0} = 3H_0/8\pi G$ is about $10^{-29}\,\text{g}\,\text{cm}^{-3}$ or about 10 hydrogen atom per cubic metre, which is incredibly thin. It can be used to express the aforementioned components ρ_i in dimensionless parameters Ω_i,

$$\Omega_i = \frac{\rho_i}{\rho_{\text{crit}}}, \quad i \in \{\text{r,m.}\Lambda\} \tag{2.14}$$

Since the Λ-term can be inserted into the density ρ as seen above, we can express the density as the total density parameter $\Omega = \sum \Omega_i$; this can be inserted back into equation (2.4) including the K-term to give at present day ($a_0 = 1$),

$$1 = \Omega_0 - \frac{Kc^2}{H_0^2} = \Omega_{\mathrm{r},0} + \Omega_{\mathrm{m},0} + \Omega_{\Lambda,0} + \Omega_{K,0}, \tag{2.15}$$

with $\Omega_K = -Kc^2/H_0^2$. This is more useful than it might seem: it is now possible to infer the curvature of the Universe simply by measuring whether all other components add up to the critical density. To get accurate measurements on the other parameters, can, however, be almost arbitrarily complicated.

If the present-day values for the density parameters are known, the Hubble function $H(a)$ can be conveniently expressed as

$$H^2(a) = H_0^2 E^2(a) = H_0^2 \left(\Omega_{\mathrm{r},0} a^{-4} + \Omega_{\mathrm{m},0} a^{-3} + \Omega_{K,0} a^{-2} + \Omega_{\Lambda,0}\right). \tag{2.16}$$

From this, it is immediately clear that given enough time, the Ω_Λ term will be dominant. In fact, this is the current cosmic era. Since the contribution from curvature is negligible and $\Omega_{\mathrm{m},0}$ is nonzero, the previous era was one where matter dominated, aptly named matter-domination. As there still is a measurable contribution from radiation as well (namely the cosmic microwave background), at even smaller a there lies an era of radiation domination.

In order to put some idea of numbers to the parameters used here, the current iteration of Planck (Planck Collaboration & Ade et mult., 2016a) gives $H_0 = 67.31 \mathrm{km\,s^{-1}\,Mpc^{-1}}$, $\Omega_{\mathrm{m},0} = 0.315$, $\Omega_{\Lambda,0} = 0.685$, whereas the other two components are negligible at $\Omega_{\mathrm{r},0} = O\left(10^{-5}\right)$ and $|\Omega_K| < 0.005$. A comprehensive list of numerical values complete with the ones used in the computations for this work is supplied in table (2.1). The respective redshifts that those values imply for the past cosmic eras are $z_{\mathrm{md}} \gtrsim 1$ for matter domination and $z_{\mathrm{rd}} \gtrsim 3000$ for radiation domination. There's a small zoo of cosmological distance measures; for this work, the most important ones are the comoving distance χ and the angular diameter distance D_{ang}. In order to find the comoving distance, we can start at with the differential $a\mathrm{d}x = c\mathrm{d}t$, which gives the distance $\mathrm{d}x$ that a photon travels in the time $\mathrm{d}t$. Integrating this one arrives at

$$\chi = c \int_{t(a)}^{t_0} \frac{\mathrm{d}t'}{a(t')} = c \int_a^1 \frac{\mathrm{d}a'}{a'^2 H(a')}, \tag{2.17}$$

where the substitution $\mathrm{d}a/\mathrm{d}t = aH$ was used. The angular diameter distance D_{ang} can be derived from the Euclidean analogue of an object of physical size Δx that appears under the angle θ,

$$\tan\theta = \frac{\Delta x}{D_{\mathrm{ang}}}. \tag{2.18}$$

If θ is used to measure the size of an object of small size compared to the sky, such as a distant galaxy, it is safe to assume $\tan\theta \approx \theta$. The physical size of the object can be expressed in terms of the comoving distance χ, scale factor a, and curvature function f_K: $\Delta x = a f_K(\chi(a))\,\theta$. Therefore,

$$D_{\mathrm{ang}} = a f_K(\chi) \tag{2.19}$$

By using 0 as a lower integration limit in the comoving distance equation (2.17), the Hubble-distance χ_H is obtained,

$$\chi_H = c \int_0^1 \frac{\mathrm{d}a'}{a'^2 H(a')} \approx \frac{c}{H_0}. \tag{2.20}$$

The Hubble-distance gives the length scale of the Universe, dividing by c would give the time scale of the Universe, or Hubble time t_H.

2.2 Inhomogeneous Cosmology

The cosmological principle stated that, on large enough scales (greater than $\sim 100\,\mathrm{Mpc}$), the Universe is homogeneous. On scales smaller than that, it evidently is not, as can be seen when looking at the night sky: There are patches of high density, such as solar systems, globular clusters, galaxies, and so on, and large voids between those structures. This section will shortly investigate how those inhomogeneities can be described and how their development can be calculated as cosmic time goes on.
First, the density contrast δ is defined, which is a measure for the local deviation from the background density $\langle\rho\rangle$,

$$\delta(\boldsymbol{x}, a) = \frac{\rho(\boldsymbol{x}, a) - \langle\rho(a)\rangle}{\langle\rho(a)\rangle}, \tag{2.21}$$

which has a lower limit of -1 if the local density is $\rho(\boldsymbol{x}) = 0$, but has no upper limit, as ρ can grow to an arbitrarily large number.
We have been treating the substrate of the cosmos like a perfect fluid, and we continue on doing so by assuming that hydrodynamical fluid equations hold for the densities ρ. In particular, they are
the Euler equation,

$$\frac{\partial \boldsymbol{v}}{\partial t} + (\nabla \cdot \boldsymbol{v})\boldsymbol{v} = -\frac{1}{\rho}\nabla p - \nabla\Phi, \tag{2.22}$$

the Poisson equation,

$$\nabla^2\Phi = 4\pi G\rho, \tag{2.23}$$

and the continuity equation,

$$\frac{\partial \rho}{\partial t} = -\nabla \cdot (\rho \boldsymbol{v}). \tag{2.24}$$

The velocity field is denoted by $\boldsymbol{v}$ and Φ is the gravitational potential. The implicit assumptions here are mass and momentum conservation.
In order to transform to comoving coordinates $\boldsymbol{r}$, remember that $\boldsymbol{x}(t) = a(t)\boldsymbol{r}(t)$, such that the velocities yield two terms,

$$\boldsymbol{v} = \dot{\boldsymbol{x}} = \dot{a}\boldsymbol{r} + a\dot{\boldsymbol{r}} = H(a)\boldsymbol{x} + a\boldsymbol{u}, \tag{2.25}$$

where the $H\boldsymbol{x}$ part is due to the background Hubble flow and $\delta\boldsymbol{v} = a\boldsymbol{u}$ the peculiar velocity.
Now explicitly assuming the limit of small perturbations δ, the three equations 2.22, 2.23, and 2.24 reduce, in first order, to

$$\frac{\partial \boldsymbol{u}}{\partial t} + 2H\boldsymbol{u} = -\frac{c_\mathrm{s}^2\nabla\delta}{a^2} - \frac{\nabla\delta\Phi}{a^2}, \tag{2.26}$$

$$\nabla^2\delta\Phi = 4\pi G\rho_\mathrm{bg}a^2\delta, \text{ and} \tag{2.27}$$

$$\frac{\partial \delta}{\partial t} = -\nabla \cdot \boldsymbol{u}. \tag{2.28}$$

Here c_s is the sound speed $c_\mathrm{s} = \sqrt{\partial p/\partial\rho}$, δ denotes the density contrast as introduced in equation (2.21), $\delta\Phi$ are fluctuations in the gravitational potential, and $\rho_\mathrm{bg} = \langle\rho\rangle$ for readability.
All these can now combined into one differential equation describing the linear growth of perturbations,

$$\ddot{\delta} + 2H\dot{\delta} = 4\pi G\rho_\mathrm{bg}\delta + \frac{c_\mathrm{s}^2\nabla^2\delta}{a^2}, \tag{2.29}$$

with the dot denoting partial derivatives w.r.t. time t. Or, in Fourier space, by decomposing δ into plane waves,

$$\delta(\boldsymbol{x},t) = \int \frac{\mathrm{d}^3k}{(2\pi)^3}\,\delta_k(\boldsymbol{k},t)\,\mathrm{e}^{-\mathrm{i}\boldsymbol{k}\cdot\boldsymbol{x}}\,, \tag{2.30}$$

with the comoving wave vector k and the amplitudes δ_k, equation (2.29) becomes, under the assumption of being able to decouple the spatial dependence of $\delta(\boldsymbol{x},t)$ from its time evolution, $\delta(\boldsymbol{x},t) = \delta(\boldsymbol{x})D(t)$,

$$\ddot{\delta}_k + 2H\dot{\delta}_k = \left(4\pi G\rho_\mathrm{bg} - \frac{c_\mathrm{s}^2k^2}{a^2}\right)\delta_k. \tag{2.31}$$

This will allow for a more detailed investigation of the behaviour of δ on different scales. Assuming the Hubble friction term to be 0, this reduces to an oscillator $\ddot{\delta}_k + \omega_0^2\delta_k = 0$ with natural frequency

$$\omega_0^2 = c_\mathrm{s}^2\frac{k^2}{a^2} - 4\pi G\rho_\mathrm{bg}, \tag{2.32}$$

which depends on the scale k. In particular, if $k \geq a/c_\mathrm{s}\sqrt{4\pi G\rho_\mathrm{bg}}$, the frequency ω_0 is real and the behaviour will be oscillatory, if k is smaller than that, ω is imaginary leading to an exponential solution, i.e. growing or decaying perturbations. The limiting case above can be re-written in terms of a comoving length scale,

$$\lambda_J = \frac{2\pi}{k} = \frac{c_\mathrm{s}}{a}\sqrt{\frac{\pi}{G\rho_\mathrm{bg}}}, \tag{2.33}$$

which is called the (comoving) Jeans length. Perturbations smaller than this will oscillate, ones greater than this will lead to growth or decay of perturbations. The validity of this can be argued very simply: The Jeans length is the distance that is covered in the gravitational free-fall time $1/\sqrt{G\rho}$ at the sound speed in the medium; in one case the gravitational interaction wins, in the other the dynamics of the medium.

It will be now assumed that the density perturbation that are described are matter, which is collisionless (so the p-terms in the original equations would vanish). This is obviously true by construction for Dark Matter. For baryonic matter, it is not entirely valid (see e.g. the ram pressure cones in Fig. (1.2)), but for the limits of tiny density fluctuations, $\delta \ll 1$ on a small background density $\langle\rho\rangle$, it certainly holds. Furthermore, only scales smaller than the horizon are considered. Using $4\pi G\rho_\mathrm{bg} = \frac{3}{2}\Omega_\mathrm{m}H^2$, the differential equation (2.29) simplifies to (Linder & Jenkins, 2003)

$$\ddot{\delta} + 2H\dot{\delta} - \frac{3}{2}H^2\Omega_\mathrm{m}\delta = 0. \tag{2.34}$$

In terms of derivatives with respect to a (denoted by a prime $'$), this leads to, assuming flatness,

$$\delta'' + \frac{3(1-w)}{2a}\delta' - \frac{3\Omega_\mathrm{m}}{2a^2}\delta = 0. \tag{2.35}$$

In the case of matter domination ($w = 0, \Omega_\mathrm{m} = 1$), there are two obvious solutions for δ with the ansatz $\delta(\boldsymbol{x}, a) = \delta_0(\boldsymbol{x})D(a)$, namely

$$D_+(a) = a \quad \text{and} \quad D_-(a) = a^{-3/2}. \tag{2.36}$$

The only interesting one is D_+, as this is the one that describes perturbation growth. A deviation from $D_+(a) = a$ is, in reverse, either an indication that another component of the Universe is starting to dominate or that the ansatz of factorising $\delta(\boldsymbol{x}, a)$ into spatial and time dependence is not valid anymore. The latter is equivalent with nonlinear structure formation setting in. In order to be able to have an expression for D_+ outside the special case of matter domination, Linder & Jenkins (2003) give a prescription for the growth function for dark energy cosmologies, which was used in the numerical computations of this work.

2.3 Statistics of inhomogeneities

It should be pointed out that the inhomogeneities discussed in section 2.2 can roughly be separated into two regimes with regards to their statistics: Linear and nonlinear. The origin of the terms linear and nonlinear stems from the only keeping terms of first order when going form equations (2.22), (2.23), and (2.24) to equations (2.26), (2.27), and (2.28) respectively. The primordial inhomogeneities are distributed in an almost perfectly Gaussian way, with non-Gaussanities being consistent with zero (Planck Collaboration & Ade et mult., 2016b). In fact, most simple models of inflation suggest only tiny deviations from Gaussian statistics in the initial conditions of the inhomogeneities (Maldacena, 2003). This makes calculating their evolution relatively straightforward, as it can be done analytically. As soon as the linearity of the evolution equations breaks down, however, higher orders are needed to arrive at useful predictions. In practice, one needs to resort to either the Zel'dovich approximation (Zel'dovich, 1970) or, if the nonlinearities are quite significant, fits from N-body simulations or analytically cumbersome methods (such as Blas et al., 2016; Bartelmann et al., 2016). The Zel'dovich approximation will appear again in section 4.2, when the generation of angular momentum in structures is discussed. In this work, I used the power spectrum fit provided by Smith et al. (2003), see Fig. (2.1).

One of the conveniences that comes with Gaussian distributions is that they are defined by two numbers, mean μ and variance σ^2. As $\langle\delta\rangle = 0$, by construction (see equation (2.21)) only the variance defines the statistics of δ – as long as it is Gaussian.
The variance can be expressed in terms of the correlation function ξ,

$$\xi(y) = \langle\delta(\boldsymbol{x})\delta(\boldsymbol{x} + \boldsymbol{y})\rangle\,, \tag{2.37}$$

where $\sigma^2 = \xi(0)$. Or, if δ is taken in the Fourier domain, the variance is expressed by the power spectrum $P(k)$,

$$\begin{aligned}\left\langle\delta_k(\boldsymbol{k})\delta_k(\boldsymbol{k}')\right\rangle &= (2\pi)^3\delta_D(\boldsymbol{k} - \boldsymbol{k}')\int \mathrm{d}^3y\,\xi(y)\,\mathrm{e}^{\mathrm{i}\boldsymbol{k}\cdot\boldsymbol{y}}\,,\\ &= (2\pi)^3\delta_D(\boldsymbol{k} - \boldsymbol{k}')\,P_\delta(k).\end{aligned} \tag{2.38}$$

Since the correlation function is unit-free, the power spectrum must therefore have the dimension of a volume. Here, δ_D is the Dirac-function. It keeps the different wave modes from coupling, which is exactly what happens if the distribution is not Gaussian and thus cannot completely be described by a single power spectrum. If this is the case, higher order correlators $\xi_N = \left\langle\delta^1\cdots\delta^N\right\rangle$, possibly infinitely many, are needed to completely describe the distribution. Reversely, the non-Gaussianity of a distribution can be measured by finding a higher

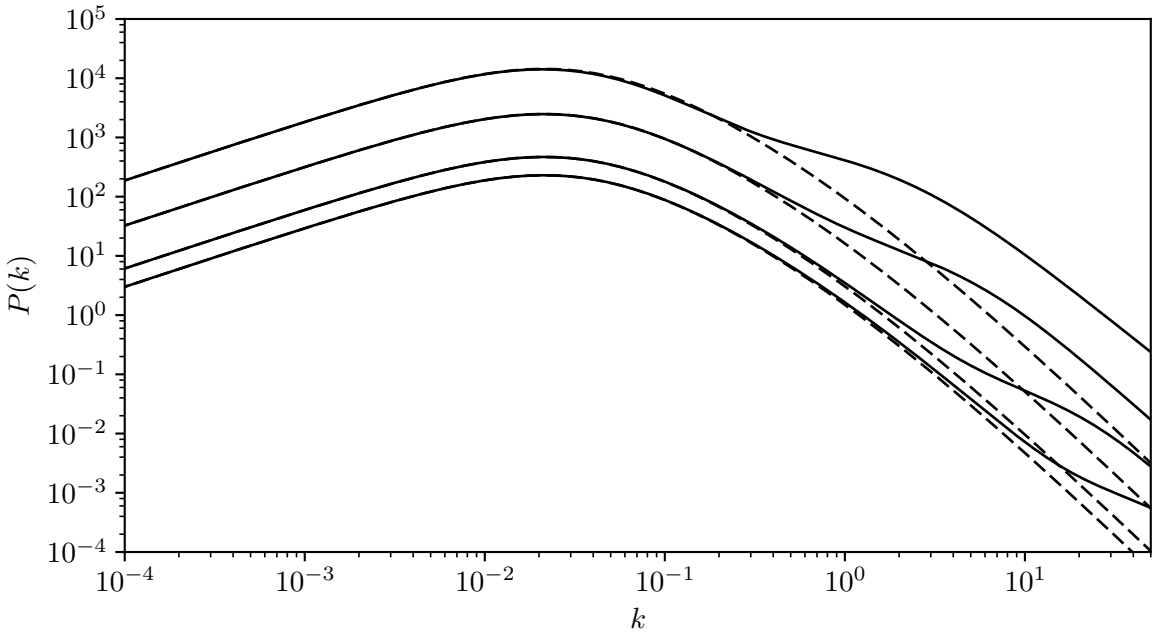

Figure 2.1: Linear (dashed lines) and nonlinear (solid lines) Power spectra calculated according to Smith et al. (2003) at different redshifts (from top to bottom) $z = 0, 2, 6, 9$.

order correlation. In particular, Gaussian distributions have no odd moments, due to the asymmetry of the integral. A nonzero bispectrum $B(\boldsymbol{k}_1,\boldsymbol{k}_2,\boldsymbol{k}_3)$ would be one such indication. Inflation predicts the initially seeded perturbations to have a nearly scale-invariant power law power spectrum (Baumann, 2007),

$$P(k) \propto k^{n_s} \tag{2.39}$$

with the spectral index n_s nearly 1. According to inflationary theory, it can't be exactly unity, as inflation had to stop at some point hence breaking scale invariance. It is indeed measured to be slightly smaller than unity (Planck Collaboration & Ade et mult., 2016a).

To set the amplitude of the power spectrum, the parameter σ_8 is a long-established tradition in cosmology. It is computed by finding the root mean square variance σ_R^2 of the random field within a real space rectangular (top-hat) window function $W(R)$ with width $R = 8\,\mathrm{Mpc}$. In Fourier space, this becomes a periodical window function W_k,

$$W_k(R) = \frac{3\,j_1(kR)}{kR}, \tag{2.40}$$

with the spherical Bessel function j_1, such that for the variance

$$\sigma_R^2 = \int \frac{k^2 \mathrm{d}k}{2\pi^2} W_k^2(R) P_\delta(k). \tag{2.41}$$

As long as it doesn't hit the nonlinear regime, the power spectrum can aptly be described by a factorisation into a- and k-dependence of the density perturbation. This is done with the growth function $D_+(a)$ and transfer function $T(k)$, so to compute the power spectrum, one has

$$P_\delta(k) \propto k^{n_s} \cdot T^2(k) \cdot D^2(a). \tag{2.42}$$

The transfer function sets the turnaround point $k*$, which is equal to the comoving horizon scale at matter-radiation equality $k* = k_{\mathrm{eq}}$: the modes small than that couldn't grow during radiation domination. The shape of the right side part of the power spectrum, which is for a the linear regime $\propto k^{n_s-4}$, is also set by the transfer function. In this work, I use the transfer function according to Bardeen et al. (1986) in order to calculate the linear power spectrum.

To link perturbations in the density perturbations δ_k and the unit-free potential Φ/c^2, equation (2.27) can be used to translate. In particular, in the k-domain,

$$-k^2c^2\Phi = \frac{3}{2a}H^2\Omega_{\mathrm{m}}\delta, \tag{2.43}$$

such that the respective power spectra $P_\Phi = \langle\Phi\Phi^*\rangle$ and $P_\delta = \left\langle\delta_k\delta_k^*\right\rangle$ are related by

$$P_\Phi(k,a) = k^{-4}\left(\frac{3\Omega_{\mathrm{m}}}{2a\chi_H^2}\right)^2 P_\delta(k,a). \tag{2.44}$$

2.4 Cosmological Constant, Dark Energy, or Modified Gravity?

When discussing the Einstein field equations (2.3), the Λ-term was introduced. Einstein (1917) originally thought it up in order to counteract gravitation and thus enable a static universe (which it was thought to be at the time). After the discovery of cosmological expansion (Hubble, 1929), Einstein quickly dismissed the idea of his λ. The freedom to include it in the field equations was however was promoted to a necessity by Lovelock (Lovelock, 1971, 1972): Lovelock's theorem states that in a metric theory of gravity in four dimensions, limited to up to second order derivatives of the metric, the most general field equations are the ones shown in equation (2.3). Now the nuisance parameter λ becomes the geometrical quantity Λ, called the cosmological constant, and there is no apparent need for it to vanish. Since the discovery of the accelerated expansion of the universe (Riess et al., 1998; Perlmutter et al., 1999), Λ has been able to explain these observations remarkably well. There are certain problems with it however. For one, there is the question of the numerical value of Λ. Trying to explain it with vacuum energy, quantum field theory famously overestimates its value by more than 100 orders of magnitude. This fine–tuning is very unsatisfactory to physicists in general, just like the fine-tuning of the curvature of the universe. Secondly, why are we observing it at all? Why do we live in a cosmic epoch of transition between matter and cosmological constant? Explaining this by citing the anthropic principle is also often not enough for many. Therefore, there is a whole branch of physics devoted to developing Dark Energy theories (Amendola & Tsujikawa, 2010), which act like a cosmological constant, but are dynamical in nature.

The fine-tuning problem in the initial curvature could be solved alongside the horizon problem (i.e. the remarkable homogeneity of the background) by the theory of inflation (Guth, 1981). Inflation and its implications on structure formation (Liddle, 1999; Baumann, 2007) have since become part of the ΛCDM paradigm. The idea behind it is to have a scalar field ϕ, often called the inflation, with the Lagrangian

$$\mathcal{L}_\phi = \frac{1}{2}g^{\mu\nu}\partial_\mu\phi\partial_\nu\phi - V(\phi). \tag{2.45}$$

From this, one can identify the entries in the stress–energy tensor $T^{\phi}_{\mu\nu}$ with density ρ and pressure p for a perfect fluid, as in section 2.1, which leads to

$$\begin{aligned} \rho_\phi c^2 &= \frac{\dot{\phi}^2}{2} + V(\phi), \\ p_\phi &= \frac{\dot{\phi}^2}{2} - V(\phi), \end{aligned} \tag{2.46}$$

and thus to the equation of state

$$w = \frac{\dot{\phi}^2 - 2V(\phi)}{\dot{\phi}^2 + 2V(\phi)}, \tag{2.47}$$

which is dynamical. Depending on the evolution of the potential V, one can have accelerated expansion ($w < -1/3$) in the early Universe, which inflates the initial curvature radius to several times the Hubble radius. Of course there are many models for the scalar field ϕ, including multi-field inflation; the Lagrangian shown in equation (2.45) is the most simple one; in practice, one would like to have some sort of coupling to matter as well.

The same principle can be applied to the late–time acceleration. Quintessence (Ratra & Peebles, 1988; Wetterich, 1988) uses a dynamical $w(a)$ in order to solve the fine–tuning and coincidence problems for Λ just like inflation.

Adding a dynamical Dark Energy into the cosmic mix means changing the consistence of the stress–energy tensor $T_{\mu\nu}$. Another –equivalent– way of changing the dynamics would be to change the laws of gravity, i.e. the left hand site of the Einstein equations. The class of theories that choose to change the laws of gravity are broadly called modified gravity. A rich subset of modified gravity theories can be expressed with a parameterisation given by Horndeski (1974) (Bellini & Sawicki, 2014), in particular quintessence and $f(R)$ gravity, which exchanges the Ricci scalar R in the Einstein–Hilbert action for a function f dependent on R. A more heuristic or phenomenological solution is to parametrise the departure from general relativity within the framework of cosmological perturbations. In particular, the scalar part of general the line element,

$$\mathrm{d}s^2 = -\left(1 + \frac{2\Psi}{c^2}\right)\mathrm{d}t^2 + a^2\left(1 - \frac{2\Phi}{c^2}\right)\mathrm{d}\boldsymbol{x}^2, \tag{2.48}$$

with the Bardeen potentials Ψ and Φ (Bardeen, 1980), can be perturbed to find evolution equations for both Ψ and Φ. In general relativity, the anisotropic stress, which is proportional to $\Phi - \Psi$, vanishes. Therefore, in standard gravity, $\Phi = \Psi$, which recovers the evolution equations from section 2.2. The gravitational slip, quantified by

$$\eta(\boldsymbol{k},a) = \frac{\Phi}{\Psi}, \tag{2.49}$$

can be used to relate the new potentials to the perturbations. The equation linking those two is the Poisson equation (2.27), which now has to be separated for Ψ and Φ:

$$-k^2\frac{\Psi}{c^2} = 4\pi G a^2 \mu(\boldsymbol{k},a)\rho_{\mathrm{bg}}\delta, \tag{2.50}$$

$$-k^2\frac{\Phi}{c^2} = 4\pi G a^2 \eta(\boldsymbol{k},a)\mu(\boldsymbol{k},a)\rho_{\mathrm{bg}}\delta. \tag{2.51}$$

$$\tag{2.52}$$

As well as

$$-k^2\frac{\Phi + \Psi}{c^2} = 4\pi G a^2 \left[\eta(\boldsymbol{k},a)\left(\mu(\boldsymbol{k},a) + 1\right)\right]\rho_{\mathrm{bg}}\delta. \tag{2.53}$$

The two functions η and μ are thus sufficient to parametrise the deviations from general relativity (Amendola et al., 2008). This can be shown to be equivalent to a Horndeski-parametrisation (Saltas et al., 2014). From the line element (8.1) it is apparent that Ψ is what in classical gravity would be called Newtonian potential. The Weyl potential $\Psi + \Phi$ is what defines null geodesics – therefore gravitational lensing is a measure for the sum of both. A local non–relativistic physical process can measure Ψ alone. One such process could be the alignment by tidal shear as seen in section 4.3. Hence, lensing and alignment processes can be used to measure gravitational slip or deviations from general relativity.

Currently, however, ΛCDM does not seem to be in disagreement with measurements, in fact, it fits the available remarkably well (Planck Collaboration, 2015). This is why only a small deviation from $\eta = \mu = 1$ is expected and is likely to be insignificant for alignments within weak lensing surveys compared to other systematics of the surveys.

2.5 Gravitational Lensing

Since the main focus of this work is an effect that changes measurements from weak gravitational lensing, understanding gravitational lensing is absolutely needed in order to understand intrinsic alignments. As mentioned in the introduction, gravitational light deflection was one of the first propositions to test general relativity. As a tool for cosmology and astrophysics, lensing is relatively new, however. The Twin Quasar Q0957+561 (Walsh et al., 1979) was the first lensed object to be detected, long after gravitational lensing had been theorised. However, only in the last 20 years have observations become a useful tool for inferences in cosmology and astrophysics.

Its realisations include strong lensing, an effect that changes the shape of a light source drastically, distorts images, and even produces multiple images with significantly different light paths. In microlensing, objects' luminosities get magnified by another object passing in front of it, focusing its light towards the observer temporarily. Both these applications are concerned with individual occurrences. Weak lensing is a statistical effect. This means that it is only observable with the knowledge of many background sources whose shape correlations are affected by their light passing by a gravitational lens, be it large scale structure like in cosmic shear measurements or a cluster like in the case of the Bullet cluster (Clowe et al., 2006).

Weak lensing and its language in particular will be discussed in detail in chapter 3. This section is to give a general overview of gravitational lensing and some of its observables. It orients itself closely along chapter 3 of the comprehensive review by Bartelmann & Schneider (2001a) with some minor differences in notation.

Firstly, the name gravitational lensing for the effect of light deflection by mass is very apt since there are many parallels between geometrical optics and gravitational lensing; in fact, most of this section will deal with geometry, as I find this to be the most illustrative derivation.

Before the geometry of gravitational lensing is discussed, however, let's again consider a lightly disturbed metric

$$\mathrm{d}s^2 = -c^2\left(1 + \frac{2\Psi}{c^2}\right)\mathrm{d}t^2 + \left(1 - \frac{2\Phi}{c^2}\right)a^2\mathrm{d}\boldsymbol{x}^2. \tag{2.54}$$

If we now want to examine light propagation, for a null geodesic $\mathrm{d}s = 0$, therefore

$$\left(\frac{\mathrm{d}\boldsymbol{x}}{\mathrm{d}t}\right)^2 = c^2\left(\frac{1 + \frac{2\Psi}{c^2}}{1 - \frac{2\Phi}{c^2}}\right) \approx c^2\left(1 + 2\frac{\Psi + \Phi}{c^2}\right), \tag{2.55}$$

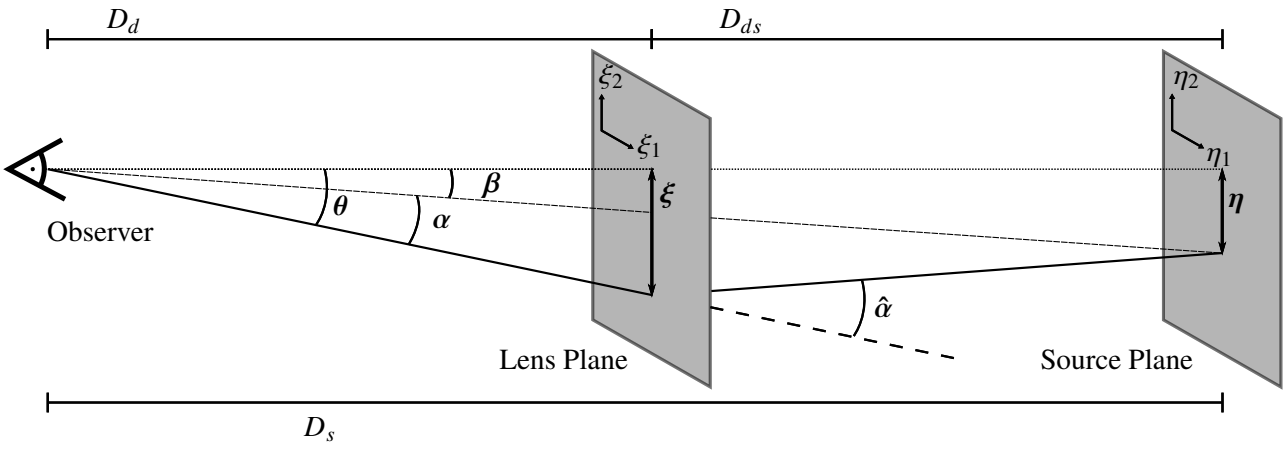

Figure 2.2: Setup of observer, lens plane, and source plane, adapted from Bartelmann & Schneider (2001a).

where the last step is valid as long as the perturbations are small, $\Phi \ll c^2$. The same assumption can be used again to find

$$c' = c\left(1 + \frac{\Psi + \Phi}{c^2}\right). \tag{2.56}$$

Now, c' is the effective speed of light in the refractive medium. It depends solely on the Weyl potential $\Psi + \Phi$, or, if we set $\Phi = \Psi$ (see section 2.4), 2Φ. Then the refractive index $n = c/c'$ of this metric is

$$n = 1 - \frac{2\Phi}{c^2}. \tag{2.57}$$

The time delay caused by this effectively reduced speed of light is the Shapiro delay (Shapiro, 1964), and can be observed even within the solar system by bouncing radar signals off other planets.
From equation (2.57), Fermat's principle would lead us directly to a relation between deflection angle $\hat{\boldsymbol{\alpha}}$ and gravitational potential Φ (Bartelmann & Maturi, 2017),

$$\hat{\boldsymbol{\alpha}} = -\frac{2}{c^2}\int \nabla_\perp \Phi \mathrm{d}\lambda, \tag{2.58}$$

but in order to introduce other quantities, it is more illustrative to get there via a small detour.

A simplified setup of a gravitational lens can be seen in Fig. (2.2). To draw this picture, a number of assumptions has already been made, first of all that all of the light deflection happens instantaneously in a single lens plane. This assumption will have to be reevaluated in a cosmic weak lensing setup as will be seen in chapter 3 where the extent of the mass distribution is comparable to the length of the light path. For the moment, a lens at angular diameter distance D_d is considered, which deflects light rays from a source at D_s. The distance from the lens to the source is D_{ds}. From Fig. (2.2), a relation between the physical size $\boldsymbol{\eta}$ of a source in the source plane, its apparent size $\boldsymbol{\xi}$ in the lens plane, and the deflection angle $\hat{\boldsymbol{\alpha}}$ can be found:

$$\boldsymbol{\eta} = \frac{D_s}{D_d}\boldsymbol{\xi} - D_{ds}\hat{\boldsymbol{\alpha}}. \tag{2.59}$$

Using the definition of the angular diameter distance (equation (2.18)), we can replace $\boldsymbol{\eta} = D_s\boldsymbol{\beta}$ and $\boldsymbol{\xi} = D_d\boldsymbol{\theta}$, such that we arrive at the lens equation,

$$\boldsymbol{\beta} = \boldsymbol{\theta} - \frac{D_{ds}}{D_s}\hat{\boldsymbol{\alpha}} = \boldsymbol{\theta} - \boldsymbol{\alpha}. \tag{2.60}$$

As pointed out in Fig. (2.2), the simple statement of the lens equation is that an un-lensed source at $\boldsymbol{\beta}$ is observed at $\boldsymbol{\theta}$.

Given a point mass M, it is possible to express the deflection angle as a function of the impact parameter ξ, if the light ray passes by M sufficiently far from its Schwarzschild radius, $\xi \gg R_S$, and has thus a small deflection $\alpha \ll 1$,

$$\hat{\alpha} = \frac{4GM}{c^2\xi}. \tag{2.61}$$

This is exactly twice the value that would be found in Newtonian gravity (von Soldner, 1804). If an ensemble of point masses is considered as lenses, a three-dimensional density $\rho(x_1,x_2,x_3)$ could describe the lens. Let coordinates of the ray's trajectory $(\xi_1(\lambda), \xi_2(\lambda), x_3(\lambda))$ parametrised by λ, chosen such that the light ray propagates along x_3. Now since the light deflection angle is small, the ray can be approximated by a straight line instead of a curved path. This assumption is commonly called the Born approximation as it is analogous to the one used in atomic physics. This helps by removing the dependency of $\boldsymbol{\xi}$ of the affine parameter λ and leads to an expression for $\hat{\boldsymbol{\alpha}}$ that projects the density ρ into a two-dimensional quantity $\Sigma(\xi)$,

$$\hat{\boldsymbol{\alpha}}(\boldsymbol{\xi}) = \frac{4G}{c^2}\int \mathrm{d}^2\xi'\Sigma(\xi')\frac{\boldsymbol{\xi}-\boldsymbol{\xi}'}{|\boldsymbol{\xi}-\boldsymbol{\xi}'|^2}, \tag{2.62}$$

with the surface mass density $\Sigma(\boldsymbol{\xi}) = \int \mathrm{d}x_3\rho\,(\xi_1,\xi_2,x_3)$. Lastly, let's rewrite this in terms of the observable angle $\boldsymbol{\theta}$. Using the lens equation (2.60), the relation $\boldsymbol{\xi} = D_d\boldsymbol{\theta}$, as well as the dimensionless surface mass-density (or convergence κ)

$$\kappa(\boldsymbol{\theta}) = \frac{\Sigma(\boldsymbol{\xi} = D_d\boldsymbol{\theta})}{\Sigma_{\mathrm{crit}}}, \text{ with } \Sigma_{\mathrm{crit}} = \frac{c^2}{4\pi G}\frac{D_s}{D_dD_{ds}}, \tag{2.63}$$

the scaled deflection angle $\boldsymbol{\alpha}(\boldsymbol{\theta})$ reads

$$\boldsymbol{\alpha}(\boldsymbol{\theta}) = \frac{1}{\pi}\int \mathrm{d}^2\theta'\kappa(\boldsymbol{\theta}')\frac{\boldsymbol{\theta}-\boldsymbol{\theta}'}{|\boldsymbol{\theta}-\boldsymbol{\theta}'|^2}. \tag{2.64}$$

The deflection angle can be expressed as a gradient of a deflection potential $\boldsymbol{\alpha} = \nabla\psi$, with

$$\psi(\boldsymbol{\theta}) = \frac{1}{\pi}\int \mathrm{d}^2\theta'\kappa(\boldsymbol{\theta})\ln|\boldsymbol{\theta}-\boldsymbol{\theta}'|. \tag{2.65}$$

Applying another differentiation operator to $\nabla\psi$ lets us arrive at a Poisson equation, $\nabla^2\psi = 2\kappa$. This is consistent with expectations, since κ expressed something like a dimensionless projected mass density and ψ is the projected deflection potential, completely analogous to equation (2.27). Note that e.g. adding a constant ψ_0 to ψ wouldn't change κ; there are transformations for ψ that won't change the convergence κ, thus there is a degeneracy when inferring ψ from κ. This is known as the mass sheet degeneracy. In particular, transformations of the kind

$$\psi(\boldsymbol{\theta},\chi) \to \psi'(\boldsymbol{\theta},\chi) = \frac{1-\lambda}{2}\boldsymbol{\theta}^2 + \lambda\psi(\boldsymbol{\theta},\chi) \tag{2.66}$$

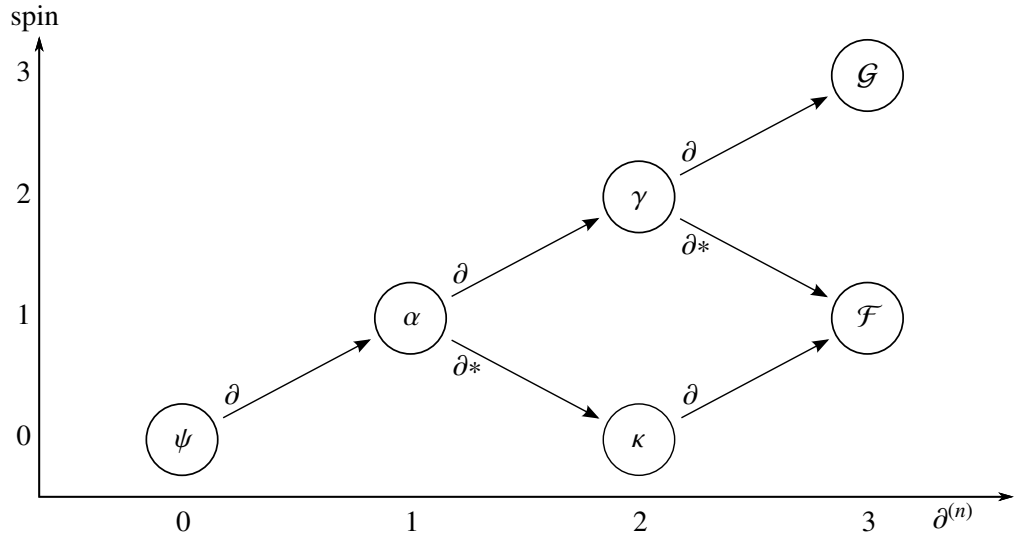

Figure 2.3: Potential, Deflection, Jacobian, flexion. Bacon & Schaefer (2009). Higher order deformation (Flexions) are shown for completeness.

with an arbitrary constant λ leave the relevant lensing observables (later introduced as reduced shear) invariant (Falco et al., 1985; Bradač et al., 2004).

The critical surface mass density Σ_{crit} gives a convenient point between strong and weak gravitational lensing. A mass distribution with $\Sigma > \Sigma_{\text{crit}}$ will produce multiple images for the same source. In this work, however, only weak gravitational lensing as a probe is considered.

The lens equation (2.60) can be locally linearised, if the lens properties do not change too much on the angular scale of the source, i.e. on that scale the change of $\boldsymbol{\beta}$ can be expressed to first order as

$$\delta\boldsymbol{\beta} = \frac{\partial\beta_i}{\partial\theta_j}\delta\boldsymbol{\theta} = \mathcal{A}_{ij}\,\delta\boldsymbol{\theta}. \tag{2.67}$$

Remembering that $\boldsymbol{\alpha} = \nabla\psi$, the Jacobian $\mathcal{A}$ can be expressed as

$$\mathcal{A}_{ij} = \frac{\partial\theta_i}{\partial\theta_j} - \frac{\partial^2\psi}{\partial\theta_i\partial\theta_j} := \delta_{ij} - \psi_{ij}. \tag{2.68}$$

In this case δ_{ij} denotes the Kronecker delta. This already shows that in the absence of a second derivative of the lensing potential ψ, the identity is recovered and no lensing takes place. Gravitational lensing is therefore to the first order a measure of the tidal shear of the lensing potential. As $\nabla^2\psi = 2\kappa$, the last degrees of freedom in $\mathcal{A}$ are the trace-free part and the off-diagonals, namely

$$\frac{1}{2}\left(\psi_{11} - \psi_{22}\right) := \gamma_1 \quad \text{and} \quad \psi_{12} := \gamma_2. \tag{2.69}$$

The shear γ can be written in terms of a complex number, as trace-free symmetric (2×2) matrices can.

$$\gamma = \gamma_1 + \mathrm{i}\gamma_2 = |\gamma|\mathrm{e}^{2\mathrm{i}\phi}\,. \tag{2.70}$$

Note that as a trace-free symmetric (2×2) matrix, the shear automatically has the same transformation properties as a spin 2 particle. The convergence κ has spin 0, as it does not change its components under rotation. See Fig. (2.3).

If a circular source with radius r is mapped with $\mathcal{A}$, it will develop two specific axes a and b,

$$a = \frac{r}{1-\kappa-\gamma} \quad \text{and} \quad b = \frac{r}{1-\kappa+\gamma}. \tag{2.71}$$

These are the semi-major semi-minor axes of an ellipse. The convergence κ changes the overall size of the circle, whereas γ induces an ellipticity ϵ

$$\epsilon = \frac{a-b}{a+b}. \tag{2.72}$$

The magnification of a source has the somewhat counter-intuitive effect that surface brightness, rather than total brightness, is conserved. From classical energy conservation, the naive expectation is that a larger source must be dimmer. However, this can be explained by the fact that the light from a lensed image has been collected from a larger area than would be in the unlensed case. For the magnification μ we write (assuming $\det \mathcal{A} \neq 0$),

$$\mu = (\det \mathcal{A})^{-1} = \det \mathcal{M} = \frac{1}{(1-\kappa)^2 - \gamma^2}. \tag{2.73}$$

The eigenvalues $\mu_{1,2}$ of $\mathcal{M}$ define two amplification directions,

$$\mu_{1,2} = \frac{1}{1-\kappa \mp \gamma}. \tag{2.74}$$

Locations where $(\mu_{1,2})^{-1} = 0$ define curves that theoretically have infinite magnification; this is practically of course never achieved. However, these curves are well-defined. Images formed close to those lines are said to be strongly lensed, far-away from them are cases of weak lensing.

It is worth mentioning that all of the above used nothing more than the fact that light travels on null geodesics in general relativity; therefore, there is no wavelength dependency in any of the lensing equations, unlike in optics, where a usually refractive index depends on the wavelength, leading to chromatic aberration and dispersion. Additionally, the polarisation directions of photons are unaffected by gravitational lensing (Dyer & Shaver, 1992; Faraoni, 1993).

2.6 Galaxies

Since the objects that are being observed by a weak gravitational lensing survey are actually galaxies, therefore it is advisable to reiterate the most important facts and define vocabulary. If not mentioned otherwise, Schneider (2015); Conselice (2014) can be used as a source for this section.

Structure formation in the Universe works bottom-up. This means that small structures form first and as cosmic time goes by, small objects interact, accumulate, or merge to form larger objects. The first stars expected to have formed around $z \lesssim 20$. To date, the oldest galaxy observed to date has a redshift of $z \sim 11$ (Oesch et al., 2016). Star formation peaked around $z = 1$ and has been going down since.

Galaxy classification is a difficult subject, as morphologies can become arbitrarily complex. However, current classifications still are reminiscent of Hubble's original scheme (Hubble, 1926) and there's general agreement on two morphological classes: elliptical galaxies and spiral galaxies.
Ellipticals are diffuse clouds of virtualised stellar mass with dust and gas. They usually ceased active star for-

mation and are among the older galaxies. They are more commonly found in high-density regions (Grützbauch et al., 2011) – the most massive galaxies known are all ellipticals. Today, they span a stellar mass range of

$$1 \times 10^7 \, M_\odot \lesssim m_{\mathrm{ell}} \lesssim 1 \times 10^{13} \, M_\odot. \tag{2.75}$$

Since the dark matter is not the dominant component within the galaxy, its total mass isn't much larger than this. The dark matter contribution increases with distance from the galactic centre, however, such that haloes can be much more massive[4]. It is also fairly certain that those haloes follow an NFW density profile (Navarro et al., 1996) in their intermediate and outer regions.

Elliptical galaxies are in general redder in appearance, i.e. their spectrum is dominated by higher wavelengths. This is in part due to the diffuse dust, but the largest contributor to this is the fact that the stars are generally much older in an elliptical galaxy and that star formation has ceased. There are notable exceptions, such as Blue Compact Dwarf galaxies, but they are both insignificant to any lensing survey due to their size and depending on the morphology definition not a 'real' elliptical. More massive blue ellipticals exist as well, but they seem to be the exception rather than the rule (McIntosh et al., 2014). The fact that they are mostly older than spiral galaxies makes the original Hubble nomenclature 'early-type' for ellipticals especially confusing. The intrinsic alignment model used in this work for ellipticals assumes that the galaxy reacts the same way its halo reacts to an outside tidal field (see section 4.3).

Spiral galaxies show a lot more structure in their stellar component; the stars form spiral arms that meet in a central bulge or bar, depending on the type. Most of the stars in the arms have a common rotational direction, giving rise to a more or less well-defined total angular momentum of the galaxy. The alignment model therefore relies upon the direction of the angular momentum vector $\boldsymbol{L}$, since this defines the direction of the disc as well (see section 4.2). In general, they aren't as massive as ellipticals,

$$1 \times 10^8 \, M_\odot \lesssim m_{\mathrm{spi}} \lesssim 1 \times 10^{12} \, M_\odot. \tag{2.76}$$

The observed flatness of the rotation curves of galaxies was one of the original problems that an invisible dark matter component solved. Spirals are also dominated by the stellar component in their core regions, but the dark matter halo surrounding the galaxy starts to be noticeable at some distance (a few kpc) from the core. Since spiral galaxies are in general younger and still star-forming – especially in the spiral arms, which cover most of their observable surface – they tend to be more prominent in blue than ellipticals. There are of course some exceptions to this rule, spiral galaxies seem to be 'going redder' as their star formation slows down or is cut off from outside effects (this is called quenching in the literature). However, these red spirals form a rather small minority within their morphological class (Tojeiro et al., 2013).

One debated question about galaxy and halo formation still is the issue on how our observations of galaxies are biasing the observations of the underlying halo structure. The galaxy bias b_{gal} is

$$\delta_{\mathrm{gal}} = b_{\mathrm{gal}} \delta_{\mathrm{dm}}. \tag{2.77}$$

Here it could be a function of mass ranges, redshift, environment, and so on. If this were the case, the power spectra of galaxies would carry additional information to the one of the dark matter. Practically, observations of b_{gal} are quite difficult, and both numerical simulations (e.g. Springel et al., 2018) and observations (e.g. Dvornik

[4]The combined haloes of galaxy clusters can go up to $1 \times 10^{15} \, M_\odot$ (Menanteau et al., 2012); this matches with the most massive objects in large simulation volumes (e.g. Pillepich et al., 2018)

et al., 2018) are in agreement that it is somewhere around unity and doesn't vary wildly e.g. across mass scales. In this work, I will set it to $b_{\mathrm{gal}} = 1$. In principle, it can be implemented, but any uncertainties would muddle the actual effects of intrinsic alignments, which is the main focus of this thesis.

Galaxy morphology depends not only on the age of the galaxies[5], but also heavily on environment (Dressler et al., 1997; Tasca et mult., 2009). Therefore, the mix of the galaxies one observes is different depending on their redshift and surroundings. In this work, however, I will assume a constant mix of galaxies with 70 per cent spirals and 30 per cent ellipticals. I will further motivate this decision in section 4.1, but roughly speaking the choice is well suited for the galaxies observed in a cosmic weak lensing survey such as Euclid, namely field galaxies with redshifts up to at most $z \sim 1.5$.

2.7 Different Observables in Cosmology

Before the toolset of weak lensing is introduced in chapter 3, I want to briefly mention other probes and observables that make modern cosmology as precise and accurate as it is. Until the detection of gravitational waves reaches a certain level of viability, our only window into the universe will be through the electromagnetic spectrum[6]. However, the amount of data that has been collected and cleverly combined is staggering. Weak lensing is by no means the only powerful tool in cosmology, it merely supplements an arsenal of observable phenomena today:

- The cosmic microwave background (CMB) was not only the first 'smoking gun' for a hot big bang (Penzias & Wilson, 1965) and later observations revealed a detailed picture of the initial conditions of the cosmos. It is sensitive on the size of the initial density perturbations, the ratio of dark matter vs. baryonic matter, it can detect galaxy clusters via the Sunyaev-Zel'dovich-effect, and since this is the oldest light signal that can reach us today, CMB measurements can very precisely determine the curvature of the Universe using a standard ruler (Durrer, 2008).

- Baryon Acoustic Oscillations (BAOs) can provide such a standard ruler. They can later still be measured in the galaxy density correlations, giving a consistent picture between $z > 1000$ and $z < 1$.

- Supernovae of type Ia were the key to measuring the accelerated expansion of the Universe (Riess et al., 1998; Perlmutter et al., 1999). They are standard(-isable) candles, thus effectively extending the reach of our distance measurements immensely.

In the near future, upcoming weak lensing surveys will try to catch up with the precision of other probes like Planck and possibly constrain the running of the Dark Energy equation of state. Also, the James Webb Space Telescope[7] will bring a fresh trove of near-optical observations that ageing telescopes like the Hubble Space Telescope wouldn't be able to, possibly opening up observational channels we haven't conceived yet. The 21 cm-line of atomic hydrogen will be an invaluable observable for cosmology with radio telescopes (Pritchard & Loeb, 2012; Zahn & Zaldarriaga, 2006). Radio telescopes can also be used for weak lensing, and particular the later stages of the Square Kilometre Array (SKA) might be able to supplement today's optical lensing data Aharonian et mult. (2013) with photon polarisation information, thus being able to distinguish lensing and intrinsic ellipticities, as the polarisation vector is not affected by lensing (Dyer & Shaver, 1992; Faraoni, 1993).

[5] Or in Hubble nomenclature, early-type galaxies are old and late-types young.
[6] Except for some cosmic ray and neutrino experiments
[7] `https://www.jwst.nasa.gov/`

	Planck 15 TT+lowP	Planck 15 max	used in this work
Ω_m	0.315 ± 0.013	0.3089 ± 0.0062	0.32
Ω_Λ	0.685 ± 0.013	0.6911 ± 0.0062	$1 - \Omega_\mathrm{m}$
$\lvert\Omega_K\rvert$	< 0.005	< 0.005	0
σ_8	0.829 ± 0.014	0.8159 ± 0.0086	0.83
n_s	0.9655 ± 0.0062	0.9667 ± 0.0040	0.96
h	0.6731 ± 0.0096	0.6774 ± 0.0046	0.68
w	-1 (ΛCDM)	-1 (ΛCDM)	-1

Table 2.1: Current measurements and values used in this work for selected cosmological parameters, the values marked Planck 15 are from Planck Collaboration & Ade et mult. (2016a), table 4. Left column: Planck 15 inferences from temperature two-point correlations and low ℓ polarisation information, middle column: Planck 15 inferences from maximum amount of combinations, including CMB lensing and external priors, right column: values used for the numerical calculations in this work. Note that all Planck–values other than Ω_K actually assume a flat geometry and only a lower bound for the curvature is listed for completeness.

Further down the road, ground-based and space-borne gravitational wave telescopes might be able to pick up signals left over from the end of inflation Chiara Guzzetti et al. (2016), which are now only looked for indirectly as artefacts in the polarisation of the CMB, but so far unsuccessfully (Planck Collaboration, 2013; Gott & Colley, 2017). Whether we will ever have a window beyond the last-scattering surface remains to be seen.

Whether neutrino-based observations will ever be feasible is an open question (Yanagisawa, 2014). Furthermore, searches aiming at direct interaction with for dark matter have so for not been successful either (e.g. Aprile et mult., 2017).

The great strides that have been made in the last 20 or so years cannot be ignored; we have a fairly good picture of what the Universe looks like compared to only 50 years ago. The current values for select cosmological parameters that are also referred to in this work can be found in table (2.1).

3 Weak Gravitational Lensing and Statistics

In this chapter, I will specialise the first results from section 2.5 to weakly lensed sources. This was defined by having magnifications μ that are far from infinity and is realised if $\kappa, \gamma \ll 1$, so if the second derivatives of ψ don't become comparable to unity.
In this chapter, I want to give an overview of the observables in weak lensing, which are in effect the ellipticities of galaxies, and how they are measured in practice. This will lead to the investigation of two dimensional two-point correlations of ellipticities and their Fourier transform, angular ellipticity power spectra. Then, a vital tool in modern weak lensing surveys is introduced, tomography, i.e. splitting up the source sample into N redshift bins and re-gaining some of the lost line-of-sight information by cross-correlating them. Since all of this requires the application of statistical analysis of the ellipticity correlations, we will investigate how good the information is that can be inferred from them and how measurements of a parameter set might be degenerated. In the last part of the chapter, a general overview of the effects of pre-correlated sources, so-called intrinsic alignments, is given as a preview for the next chapters. The first part of this chapter is, just like section 2.5, oriented along Bartelmann & Schneider (2001a).

3.1 Gravtitational Lensing Observables

As stated in section 2.5, the motivated linear projection by use of a Jacobian $\mathcal{A}$ will induce ellipticity in a circular source of the form

$$\epsilon = \frac{a-b}{a+b}. \tag{3.1}$$

With the semi-minor and semi-major axes a and b from equation (2.71), this becomes

$$\epsilon = \frac{a-b}{a+b} = \frac{\gamma}{1-\kappa} := g \approx \gamma. \tag{3.2}$$

Where g is called the reduced shear. In the case of weak lensing we can write $g \approx \gamma$, such that ellipticity becomes a measure of the shear γ. In an observation, the

How to measure galaxy ellipticities in the first place isn't a trivial task, especially in a world of limited resolutions, noisy data, and finite computing power. I will give an overview of the classic method mentioned in Bartelmann & Schneider (2001a) for reasons of didactic continuity. The classical method of choice is called KSB after Kaiser et al. (1995); it has a number of flaws: it assumes ellipticties to be small, whereas weak lensing only makes statements about the change of ellipticities, not their original values. KSB also is not able to completely account for an arbitrary PSF[1] (e.g. Viola et al., 2011). There are a number of different techniques for measuring elliptic ties which are used today, such as decomposing the galaxy brightness profiles into shapelets (e.g. Refregier & Bacon, 2003) or to fit them freely in Bayesian methods (e.g. Miller et al., 2007), but exploring the intricacies of those methods would go beyond the scope of this work.

[1] Point-spread function, an intrinsic property of a telescope of how a point source is projected on the image plane after passing through its optics.

Let $I(\boldsymbol{\theta})$ be the brightness function of a galaxy (assuming this function can be found or measured for a separated galaxy). The centre of brightness $\bar{\boldsymbol{\theta}}$ can then be defined as

$$\bar{\boldsymbol{\theta}} = \frac{\int \mathrm{d}^2\theta\, \boldsymbol{\theta} I(\boldsymbol{\theta})}{\int \mathrm{d}^2\theta\, I(\boldsymbol{\theta})}, \tag{3.3}$$

which is just the (normalised) first moment of the distribution. Then the second (quadrupole) moments

$$Q_{ij} = \frac{\int \mathrm{d}^2\theta \left(\boldsymbol{\theta} - \bar{\boldsymbol{\theta}}\right)_i \left(\boldsymbol{\theta} - \bar{\boldsymbol{\theta}}\right)_j I(\boldsymbol{\theta})}{\int \mathrm{d}^2\theta\, I(\boldsymbol{\theta})}, \tag{3.4}$$

can be set in a direct relation to the complex (observed) ellipticity ε,

$$\varepsilon_{\mathrm{gal}} = \frac{Q_{11} - Q_{22} + 2\mathrm{i}Q_{12}}{Q_{11} + Q_{22} - 2\left(Q_{11}Q_{22} - Q_{12}^2\right)^{1/2}}. \tag{3.5}$$

If the brightness moments are transformed with the Jacobian $\mathcal{A}$ from equation (2.68), $Q' = \mathcal{A}Q\mathcal{A}^T$, it becomes (Seitz & Schneider, 1997)

$$\varepsilon = \frac{\varepsilon_{\mathrm{gal}} + g}{1 + g^*\varepsilon_{\mathrm{gal}}}, \tag{3.6}$$

where g is the reduced shear and the star denotes a complex conjugate. In weak lensing $g \ll 1$ and $\gamma \approx g$, this observed ellipticity ε will reduce to an intuitive formulation: it consist of a some intrinsic ellipticity of the galaxy $\varepsilon_{\mathrm{gal}}$ and an added lensing shear γ,

$$\varepsilon = \varepsilon_{\mathrm{gal}} + \gamma, \tag{3.7}$$

and the idea is that averaging over many galaxies will average out the intrinsic ellipticities. So if galaxies are just randomly oriented before their light is lensed,

$$\langle\varepsilon\rangle = 0 + \langle\gamma\rangle\,. \tag{3.8}$$

Therefore, in this model, if the 'mean galaxy' in a region is not round, there has been a shearing effect due to lensing.

The shear tensor can be written as

$$\gamma = \begin{pmatrix} \varepsilon_+ & \varepsilon_\times \\ -\varepsilon_\times & \varepsilon_+ \end{pmatrix}, \tag{3.9}$$

where $\varepsilon_+ = |\varepsilon|\cos(2\varphi)$ and $\varepsilon_\times = |\varepsilon|\sin(2\varphi)$ in terms of the phase of the complex ellipticity $\varepsilon = |\varepsilon|\mathrm{e}^{2i\varphi}$. Then, the shear field can be written as a function of two scalar functions, Φ_E and Φ_B (Stebbins, 1996; Kamionkowski et al., 1997; Crittenden et al., 2002),

$$\gamma_{\alpha\beta} = \left(\partial_\alpha\partial_\beta - \frac{\delta_{\alpha\beta}}{2}\nabla^2\right)\Phi_E + \frac{1}{2}\left(\epsilon^{\mathrm{as}}_{\sigma\beta}\partial_\alpha\partial_\sigma + \epsilon^{\mathrm{as}}_{\sigma\alpha}\partial_\sigma\partial_\beta\right)\Phi_B, \tag{3.10}$$

where $\epsilon^{\mathrm{as}}_{\alpha\beta}$ is the anti-symmetric tensor. The decomposition discriminates a gradient and a curl part, which are named for their electromagnetic equivalents of electric and magnetic potentials E and B. The ellipticity field components are then

$$\varepsilon_+ = \gamma_{xx} = -\gamma_{yy} = \frac{1}{2}\left(\Phi_{E,xx} - \Phi_{E,yy}\right) - \Phi_{B,xy}, \tag{3.11}$$

and

$$\varepsilon_\times = \gamma_{xy} = \gamma_{yx} = \Phi_{E,xy} + \frac{1}{2}\left(\Phi_{B,xx} - \Phi_{B,yy}\right). \tag{3.12}$$

Again, the indices on the potential denote derivatives. The E and B parts can be isolated using ∇^4,

$$\nabla^4\Phi_E = 2\partial_\alpha\partial_\beta\gamma_{\alpha\beta} \quad \text{and} \quad \nabla^4\Phi_B = 2\epsilon^{\text{as}}_{\alpha\beta}\partial_\alpha\partial_\sigma\gamma_{\beta\sigma}. \tag{3.13}$$

Now we can define variables that make the E–B decomposition easier to compare to ellipticities, namely $2\gamma_{E,B} := \nabla^2\Phi_{E,B}$:

$$\begin{aligned}\nabla^2\gamma_E &= \partial_\alpha\partial_\beta\gamma_{\alpha\beta} = \left(\partial_x\partial_x - \partial_y\partial_y\right)\varepsilon_+ + 2\partial_x\partial_y\epsilon_\times \quad \text{and}\\ \nabla^2\gamma_B &= \epsilon^{\text{as}}_{\alpha\beta}\partial_\alpha\partial_\sigma\gamma_{\alpha\sigma} = \left(\partial_x\partial_x - \partial_y\partial_y\right)\varepsilon_\times - 2\partial_x\partial_y\epsilon_+.\end{aligned} \tag{3.14}$$

Just like the mass-sheet degeneracy in κ, γ_E and γ_B yield the same ellipticities if a linear or constant function is added.

Rotating the axes by $\pi/4$ will translate the +– and ×–ellipticities into one another: $\varepsilon'_+ = -\varepsilon_\times$ and $\varepsilon'_\times = \varepsilon_+$; however, this does not affect the measured quantities in E and B, as the positions are rotated as well. A rotation of the individual ellipticities by $\pi/4$ and keeping the vector positions fixed, however, will exchange E and B quantities: $\gamma'_E = -\gamma_B$ and $\gamma'_B = \gamma_E$. A sketch of their symmetries can be seen in Fig. (3.1): The E-modes are gradient-like and align tangentially or radially, the B modes are curl-like and form a 'windmill' pattern. The B-modes in particular have the properties of a pseudo scalar, as changing parity will induce a sign flip. In a normal weak lensing setup, where the shear can be expressed by a scalar potential, $\Phi_E = \psi$ and $\Phi_B = 0$, therefore there are no B-modes from weak gravitational lensing. This means that, reversely, checking for B-modes is a consistency check for systematics. By convention, E–modes with tangential alignment has a positive sign and a negative sign denotes radial alignment.

Plugging in $\Phi_E = \psi \propto \Phi$ for weak lensing, the complex shear γ for weak lensing is

$$\gamma(\Phi) \propto \Big(\underbrace{\Phi_{yy} - \Phi_{xx}}_{\gamma_+} + \mathrm{i}\,\underbrace{2\Phi_{xy}}_{\gamma_\times}\Big). \tag{3.15}$$

]

However, in cosmic weak lensing, we are interested in extended lenses, as the large-scale structure itself is the lens. Therefore, it is important to find an integral expression for the lensing potential (equation (2.65)). Remembering equation (2.58) gives

$$\psi(\theta,\chi) = \frac{2}{c^2}\int_0^\chi \mathrm{d}\chi' \frac{\chi - \chi'}{\chi\chi'}\Phi(\chi'). \tag{3.16}$$

We are implicitly assuming zero curvature again, as throughout this work. If one wanted to consider cases with non-negligible curvature, the χ would become $f_K(\chi)$. Projecting along χ with a probability distribution $n(z)$, which takes into account the fact that galaxies (i.e. the sources) are not uniformly distributed in χ, one finds the two-dimensional effective potential

$$\psi_{\text{eff}}(\theta) = \int_0^{\chi_H} \mathrm{d}\chi W(\chi)\,\Phi \tag{3.17}$$

with the weighting function W

$$W(\chi) = \frac{2}{a}\frac{G(\chi)}{\chi}, \tag{3.18}$$

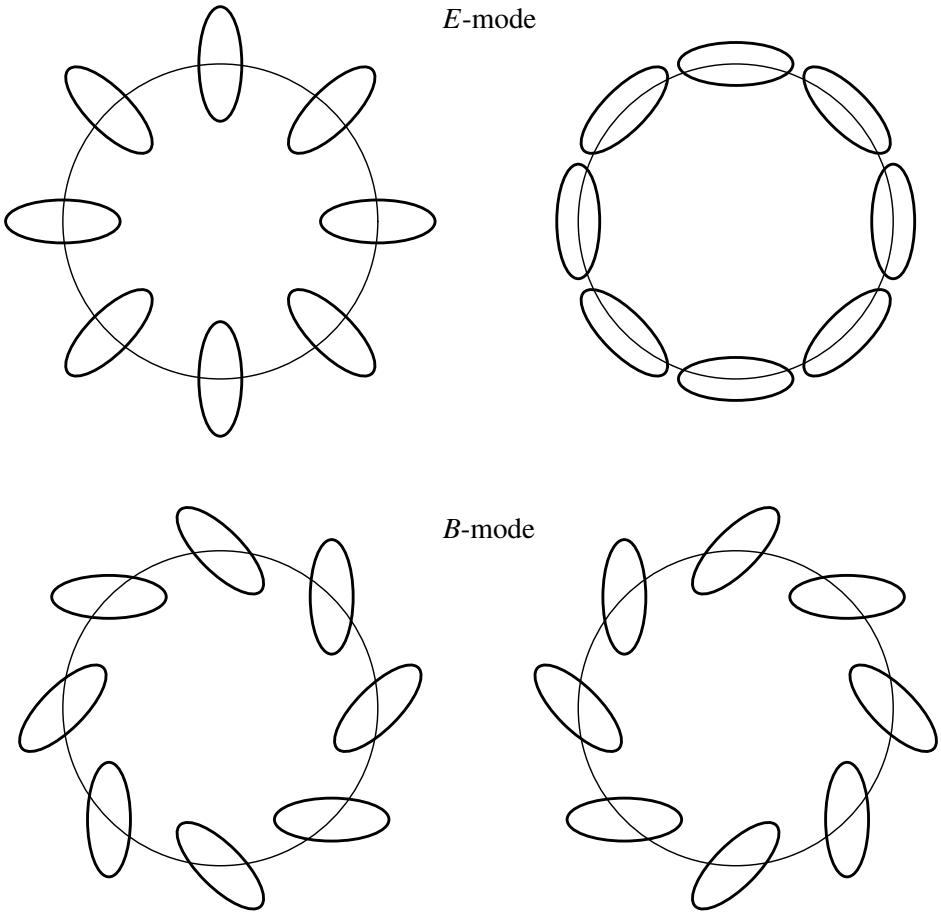

Figure 3.1: Sketch of E-modes and B-modes. Note that the curl-like B mode flips its sign under parity transformations such as looking at the sketch in a mirror.

which in turn contains the efficiency function $G(\chi)$ that combines the galaxy distribution and the lensing efficiency

$$G(\chi) = \int_{\chi}^{\chi_H} \mathrm{d}\chi' n(\chi) \frac{\mathrm{d}z}{\mathrm{d}\chi} \left(1 - \frac{\chi}{\chi'}\right). \tag{3.19}$$

Within this work, the galaxy distribution $n(z)$ is parametrised by the normalised function

$$n(z)\mathrm{d}z = \frac{\beta}{z_0 \Gamma(\frac{3}{\beta})} \left(\frac{z}{z_0}\right)^2 \exp\left\{-\left(\frac{z}{z_0}\right)^{\beta}\right\} \mathrm{d}z. \tag{3.20}$$

This distribution takes two free parameters, β and z_0. For a reference of values used, consider table (3.1), where z_0 is also called z_{median} for clarity. The parameter β is used to have a slightly steeper than exponential cutoff for large z, and is usually set to $3/2$. As measuring correlation pairs of ellipticities is statistically more powerful than measuring the mean shape of galaxies, the correlation function $\langle \gamma\gamma' \rangle$ is measured. This is also because the two-point correlation of the large-scale structure is known: $\langle \Phi\Phi' \rangle$ is related to the matter power spectrum. The two-point correlation $\langle \gamma\gamma' \rangle$ can be connected to the observed ellipticties $\langle \varepsilon\varepsilon' \rangle$. Because of the equation (2.65) and equation (3.2) we have

$$\langle \varepsilon\varepsilon' \rangle = \langle \gamma\gamma' \rangle = k^4 \langle \psi\psi' \rangle \tag{3.21}$$

3.2 From Correlations to Spectra

Now in order to calculate the two point correlator $\langle \gamma\gamma' \rangle$, we need to project a three-dimensional correlation onto the plane of the sky. This is done via the Limber equation (Limber, 1954). We are again following the explanation from Bartelmann & Schneider (2001b); the functions we are considering are of the form

$$g_i(\theta) = \int \mathrm{d}\chi \, q_i(\chi) \delta(\theta, \chi). \tag{3.22}$$

They form a correlator $C(\theta)$,

$$C(\theta) = \langle g_1(\theta) g_2(\theta') \rangle = \int \mathrm{d}\chi \int \mathrm{d}\chi' \, q_1(\chi) q_2(\chi') \left\langle \delta(\theta,\chi) \delta(\theta',\chi') \right\rangle. \tag{3.23}$$

Re-writing the δ as their Fourier transforms, the correlator becomes the matter power spectrum P_δ,

$$C(\theta) = \int \mathrm{d}\chi \int \mathrm{d}\chi' \, q_1(\chi) q_2(\chi') \int \frac{\mathrm{d}^3k}{(2\pi)^3} \frac{\mathrm{d}^3k'}{(2\pi)^3} \, \mathrm{e}^{-\mathrm{i}\chi \boldsymbol{k}_\perp \cdot \boldsymbol{\theta}} \, \mathrm{e}^{-\mathrm{i}k_3\chi} \, \mathrm{e}^{+\mathrm{i}\chi' \boldsymbol{k}'_\perp \cdot \boldsymbol{\theta}'} \, \mathrm{e}^{+\mathrm{i}k'_3\chi'} \, \delta_{\mathrm{D}}(\boldsymbol{k} - \boldsymbol{k}') P_\delta(k_\perp, \chi, \chi'). \tag{3.24}$$

The argument now is that over a certain coherence scale L_{coh}, the power spectrum effectively vanishes. Furthermore, q_i does not vary significantly in χ over scales smaller than L_{coh} such that it can be considered constant to be a fair approximation that $q_2(\chi') = q_2(\chi')$.

$$C(\theta) = \int \mathrm{d}\chi \, q_1(\chi) q_2(\chi) \int \frac{\mathrm{d}^2k_\perp}{(2\pi)^2} P_\delta(k_\perp, \chi) \mathrm{e}^{-\mathrm{i}\boldsymbol{k}_\perp \chi(\boldsymbol{\theta} - \boldsymbol{\theta}')} \, \mathrm{e}^{-\mathrm{i}k_3\chi} \int \frac{\mathrm{d}\chi'}{2\pi} \mathrm{e}^{+\mathrm{i}k_3\chi'}. \tag{3.25}$$

The remaining χ'-integral gives $\delta_{\mathrm{D}}(k_3)$, meaning we restrict ourselves to one plane in χ. Integrating over k_3 and renaming $(\boldsymbol{\theta} - \boldsymbol{\theta}') \to \boldsymbol{\theta}$ leaves us with

$$C(\theta) = \int \mathrm{d}\chi \, q_1(\chi) q_2(\chi) \int \frac{\mathrm{d}^2k_\perp}{(2\pi)^2} P_\delta(k_\perp, \chi) \mathrm{e}^{-\mathrm{i}\chi \boldsymbol{k}_\perp \cdot \boldsymbol{\theta}}. \tag{3.26}$$

Instead of angular correlations it is sometimes preferred to go to Fourier space and look at the angular power spectrum $C(\ell)$:

$$C(\ell) = \int \mathrm{d}^2\theta \, \mathrm{e}^{i\boldsymbol{\ell}\cdot\boldsymbol{\theta}} \, C(\theta), \tag{3.27}$$

The two exponentials can be combined and integration over θ leaves a $(2\pi)^2\delta_\mathrm{D}(\boldsymbol{\ell} - \boldsymbol{k}_\perp)$,

$$C(\ell) = \int \mathrm{d}\chi \, q_1(\chi) q_2(\chi) \int \mathrm{d}^2 k_\perp \, P_\delta(k_\perp, \chi) \delta_\mathrm{D}(\boldsymbol{\ell} - \chi \boldsymbol{k}_\perp), \tag{3.28}$$

fixing $k = l/\chi$, such that in the end the angular power spectrum is

$$C(\ell) = \int \frac{\mathrm{d}\chi}{\chi^2} q_1(\chi) q_2(\chi) P_\delta\left(k = \frac{\ell}{\chi}, \chi\right). \tag{3.29}$$

Since $P_\delta \propto k^4 P_\Phi$, the lensing spectra have a similar relation: $C_\kappa \propto l^4 C_\psi$.

Similarly to how we could define E– and B–modes in the shear field (cf. equation (3.13)), we can directly from the + and × decomposition of the ellipticities ε and their correlation functions (Kaiser, 1992) define E– and B–mode angular power spectra (Schneider & Kilbinger, 2007):

$$\begin{aligned} C^\gamma_+(\theta) &= \langle \gamma_+ \gamma'_+ \rangle + \langle \gamma_\times \gamma'_\times \rangle \,, \\ C^\gamma_-(\theta) &= \langle \gamma_+ \gamma'_+ \rangle - \langle \gamma_\times \gamma'_\times \rangle \,, \end{aligned} \tag{3.30}$$

can be transformed into E– and B–modes via

$$\begin{aligned} C^\gamma_E(\ell) &= \pi \int \theta \mathrm{d}\theta \left[C^\gamma_+(\theta) J_0(\ell\theta) + C^\gamma_-(\theta) J_4(\ell\theta) \right], \\ C^\gamma_B(\ell) &= \pi \int \theta \mathrm{d}\theta \left[C^\gamma_+(\theta) J_0(\ell\theta) - C^\gamma_-(\theta) J_4(\ell\theta) \right]. \end{aligned} \tag{3.31}$$

For weak lensing alone, this is a bit artificial, as there are no B–modes, but these relations will come in quite handy once there are ellipticity correlations from other effects such as intrinsic alignments.

3.3 Intrinsic Alignments, II– and GI–Correlations

Since galaxies are not perfect spheres to begin with, weak lensing can only work if the sample of galaxies is large enough. Intrinsic ellipticities are then averaged out (cf. equation (3.8)) and only the weak lensing shear is measured. This breaks down as soon as one measures correlations rather than averages and the original assumption of uncorrelated intrinsic ellipticities is challenged. In general, then the correlations become a bit more complicated,

$$\langle \varepsilon \, \varepsilon' \rangle = \left\langle \left(\gamma + \epsilon^\mathrm{i}\right) \, \left(\gamma + \epsilon^\mathrm{i}\right)' \right\rangle = \underbrace{\left\langle \gamma \, \gamma' \right\rangle}_{\mathrm{GG}} + \underbrace{\left\langle \gamma \, \epsilon^{\mathrm{i}'} \right\rangle}_{\mathrm{GI}} + \underbrace{\left\langle \epsilon^\mathrm{i} \, \gamma' \right\rangle}_{\mathrm{IG}} + \underbrace{\left\langle \epsilon^\mathrm{i} \, \epsilon^{\mathrm{i}'} \right\rangle}_{\mathrm{II}}. \tag{3.32}$$

The first part is the ordinary weak lensing correlation, sometimes called GG for galaxy–galaxy–lensing. The last part is the intrinsic non–zero correlation of galaxy ellipticities, sometimes dubbed II for intrinsic–intrinsic. The middle part is called GI–contribution as it is a mixture of lensing and intrinsic alignments. The idea is that while one galaxy can be aligned by a structure, a background galaxy is lensed by the same structure, therefore inducing a rather complicated correlation between the two ellipticities. This was first described by Hirata &

Seljak (2004). Fig. (3.2) illustrates the setup of the three types of ellipticity correlations. First, normal lensing by a correlated density field that both galaxies' light bundles pass through on their way to the observer. In that way, they probe the entire density field from the source to the observer, making this an integrative effect. The second setup shows two galaxies with correlated ellipticities due to their local environment. This effect is purely local, as the ellipticties are physically aligned. The third contribution, GI–correlations is a mix of both: a local galaxy is aligned with a local density field, which lenses a background source, correlating the nearby galaxy's ellipticity with the background galaxy's light bundle on its way to the observer. This evidently only works in the "GI" direction, as an "IG" would require a density field to change the ellipticity of a galaxy closer to the observer than itself.

Since these effects are all additive, the observed spectrum $C^{\varepsilon}_{\mathrm{obs}}(\ell)$ will be

$$C^{\varepsilon}_{\mathrm{obs}}(\ell) = C^{\gamma\gamma}_{E}(\ell) + C^{\gamma\epsilon}_{E}(\ell) + C^{\epsilon\epsilon}_{E}(\ell). \tag{3.33}$$

In order to compare the effects of intrinsic alignments to those of weak lensing and to determine their influence, a model is needed. Theoretically, if a 'perfect' model for intrinsic alignments could be constructed, the pure lensing spectrum could be recovered from an ideal observation with no other systematics. This work actually uses two different models to treat spiral and elliptical galaxies separately due to their vastly different physical properties. These models will be introduced in chapter 4.

3.4 Tomography

Accurate data for galaxy redshifts makes it possible to regain some of the information lost by the line-of-sight projection by sorting the sample of galaxies into different redshift bins and correlating those bins with each other; this technique is called tomographic weak lensing (Hu, 1999; Takada & White, 2004; Takada & Jain, 2004). The splitting is done within the weighting function of equation (3.17), such that ψ gains an index i:

$$\psi_i = \int_0^{\chi_H} \mathrm{d}\chi W_i(\chi)\Phi, \tag{3.34}$$

the index is handed through to the efficiency function $G_i(\chi)$ which appears in $W_i(\chi)$ (cf. equations (3.18) and (3.19)),

$$W_i(\chi) = 2\frac{D_+}{a}\frac{G_i(\chi)}{\chi}, \tag{3.35}$$

and finally appears either as condition on the galaxy distribution (as originally in Hu (1999)) or, more convenient for numerical evaluation, in the integration limits,

$$G_i(\chi) = \int_{\min(\chi,\chi_i)}^{\chi_{i+1}} \mathrm{d}\chi' n(\chi')\frac{\mathrm{d}z}{\mathrm{d}\chi'}\left(1 - \frac{\chi}{\chi'}\right). \tag{3.36}$$

Here, χ_i is the lower bound of bin i and χ_{i+1} both the upper bound of the ith bin as well as the lower bound of bin number $i+1$. For $i = 1$, evidently weak lensing as described before this section is recovered. This splitting along χ is not without alternative, e.g. Schaefer & Heisenberg (2012) show splitting up the galaxy sample according to orthonormal polynomials, which has some mathematical advantages because the cross-correlations between bins vanish but is much harder to accomplish than a simple splicing of the distribution along χ. The bins are chosen such that the same number of galaxies are in each bin, therefore the shot noise is the same across bins

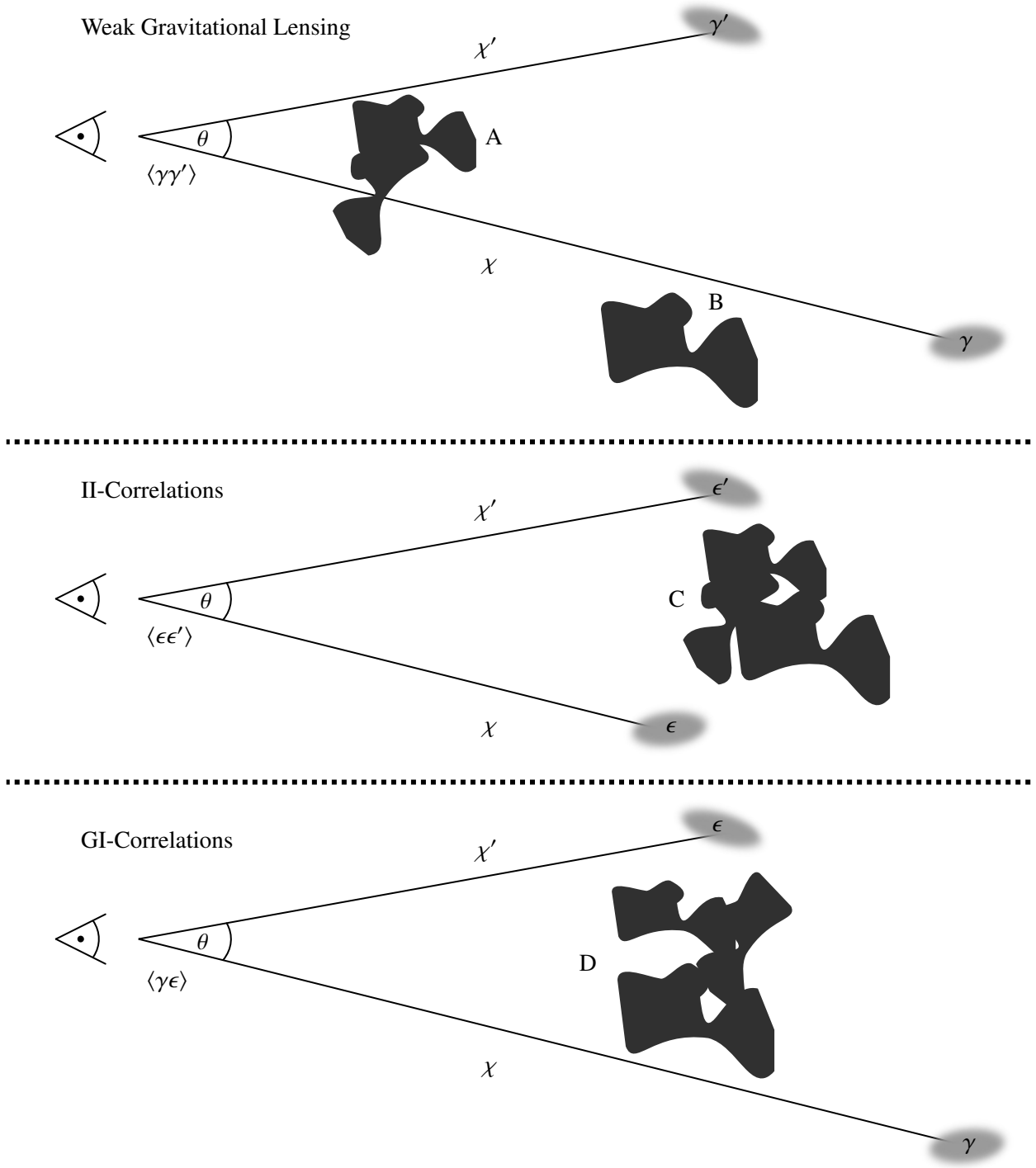

Figure 3.2: The three correlation types induced by nonvanishing intrinsic ellipticity correlations, GG–, II–, and GI–correlations respectively. The first is what we called weak lensing so far: a structure (A) correlates observed ellipticities as their light bundles pass through a correlated density field. This is integrated over χ, hence it is a nonlocal effect. The second is a purely local effect, with comparatively small range, as both ellipticities are physically correlated by a correlation in the local environment (C). GI–correlations are more subtle as a structure (D) that influences a nearby (local) galaxy lenses the light from a background galaxy. Note that this only works one way, i.e. there are no IG–correlations.

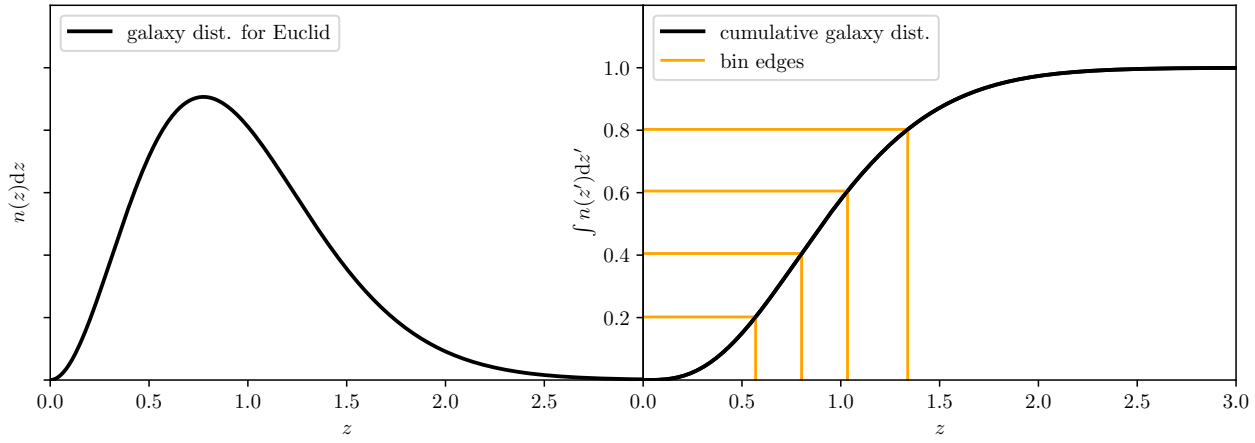

Figure 3.3: Differential and cumulative galaxy distribution for a Euclid-like survey ($z_0 = 0.64, \beta = 3/2$), split in five tomographic bins such that each has the same amount of galaxies in it, the bins are evenly spaced on the ordinate (probability) but are not necessarily the same size on the abscissa (redshift z).

and each bin holds the same amount of statistical weight. A sketch of the splicing can be seen in Fig. (3.3). Similarly to equation (3.29), the spectra are then,

$$C_{ij}^{\psi}(\ell) = \int_0^{\chi_H} \frac{\mathrm{d}\chi}{\chi^2} W_i(\chi) W_j(\chi) P_\Phi\left(k = \frac{l}{\chi}\right), \tag{3.37}$$

where ij denotes the i–j–bin correlation. Note that the explicit χ–dependence of $P(k)$ has been transferred to W_i as a factor of D_+. The spectrum is symmetric in ij, as W_i and W_j commute. This is not the case with GI/IG–alignments, but will be dealt with by symmetrising C_{ij} and thus enforcing statistical isotropy. Again, because of the choice of slicing W_i, the galaxies from bin i contain information about the potential in bins $1 \ldots i$. Therefore, C_{ij} is not diagonal and in particular, there will be shape noise of the form $\sigma_\epsilon^2 n_{\mathrm{bin}}/\bar{n}$ on the diagonal, which explicitly cancels if two different bins are correlated. The shear E–mode spectrum is equal to $\ell^4/4 C_{ij}^{\psi}(\ell)$. The lensing spectra and shape noise for five bins in a survey like Euclid is shown in Fig. (3.4). A measure for for statistical dependence is the correlation coefficient between different spectra,

$$R_{ij} = \frac{C_{ij}}{\sqrt{C_{ii}\, C_{jj}}} \in [0,1]. \tag{3.38}$$

It can be used to estimate the amount of new information gained by increasing the number of bins. Ideally, it is close to zero, meaning that different spectra carry different information. Being close to unity would point to a saturation, making adding more bins less statistically profitable. A typical number of bins for modern surveys is in the range of three to six, while future surveys such as Euclid could possibly sustain a few more. The highest number of bins considered in this work is seven.

3.5 Fisher Information and Bias Estimation

In order to quantify the statistical error, the Fisher formalism is the established method in the case of Gaussian statistics and can even be corrected for non-Gaussian cases (Sellentin, 2015). In the scope of this work, however, it is feasible to stay within the realms of Gaussianity, as there is even a way of quantifying systematic errors induced by fitting an oversimplified model to data (as is done when fitting a pure lensing likelihood to a signal

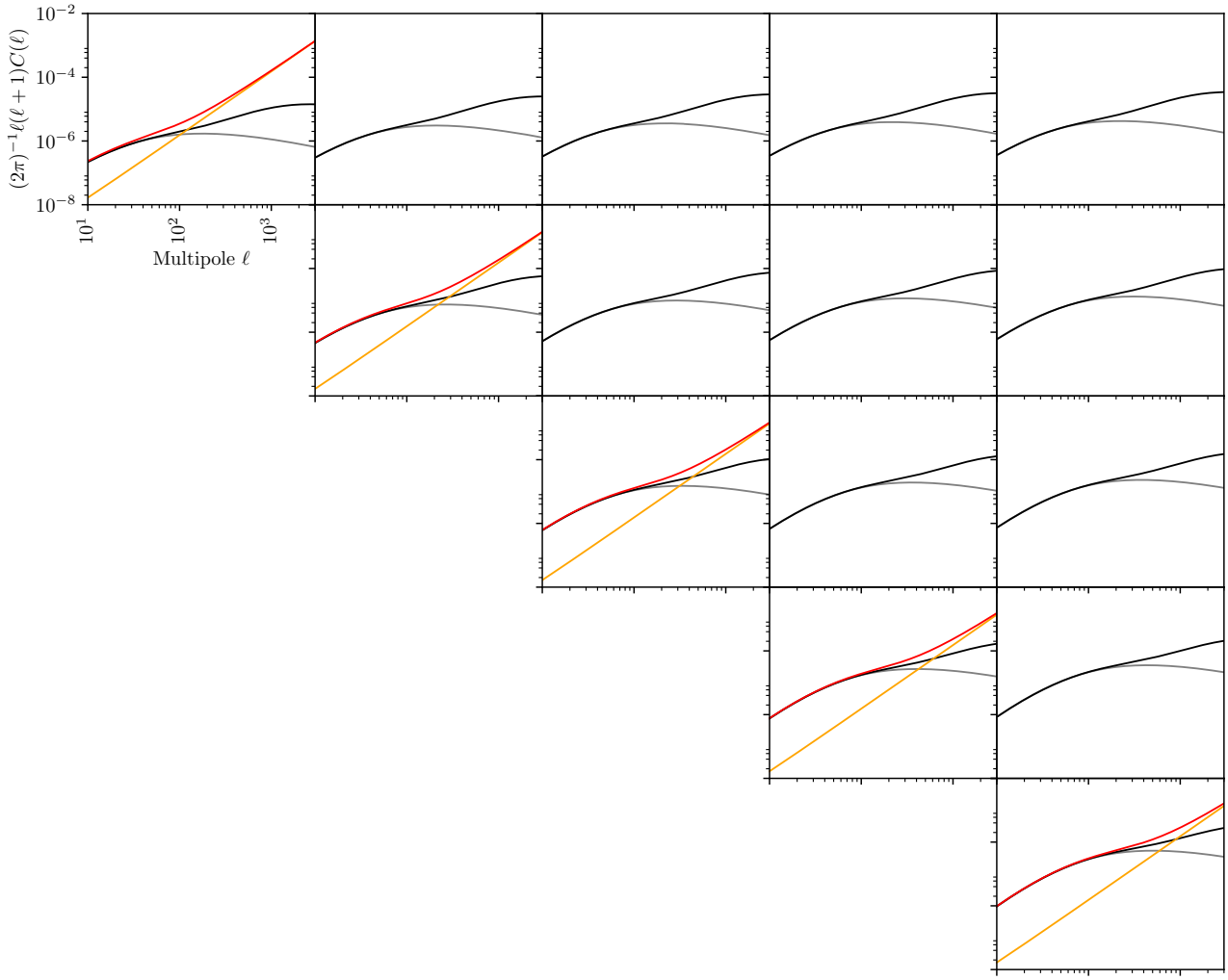

Figure 3.4: Tomographic weak lensing spectra for $n_{\mathrm{bin}} = 5$ for a Euclid-like survey. Black lines use the nonlinear power spectrum $P(k)$, grey lines show the linear power spectrum $P_{\mathrm{lin}}(k)$, the constant shape noise looks is shown in orange, and the observed (nonlinear) spectrum, i.e. $C^{\gamma}_{ij}(\ell) + \left(\sigma^2_{\epsilon} n_{\mathrm{bin}}/\bar{n}\right)$ in red.

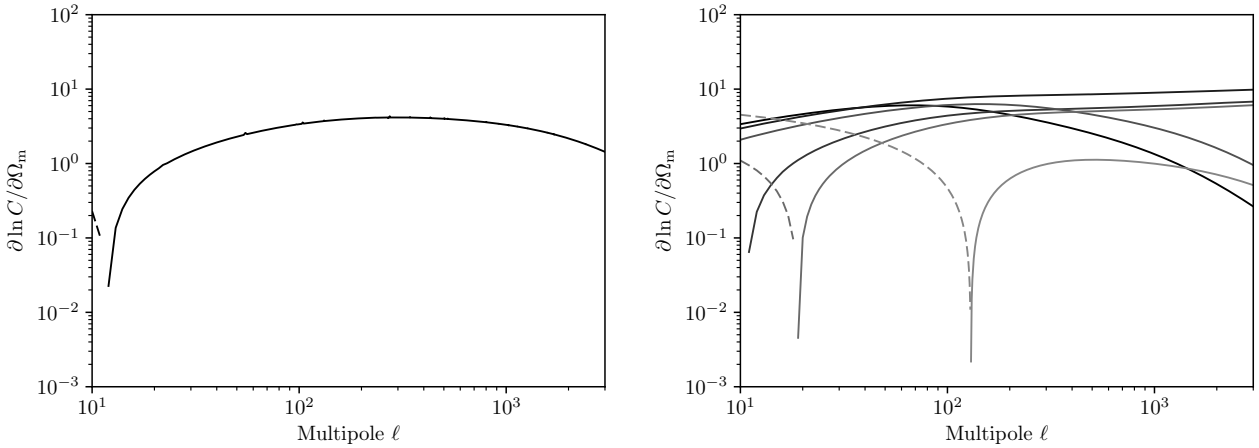

Figure 3.5: Log derivative of the (nonlinear) weak lensing spectra with respect to Ω_m. Left: one tomographic bin, right: three tomographic bins, dashed lines indicate negative values. In particular the sign flips are an interesting feature: they indicate on which angular scale the spectrum is not at all sensitive to a change in a parameter.

containing intrinsic alignments as well). The likelihood L quantifies how likely it is that a set of fitted parameters θ_i can explain a data set. The Fisher information matrix is defined via the curvature in parameter-space of the log-likelihood $\mathcal{L} = -\ln L$ (Tegmark et al., 1997):

$$F_{\mu\nu} = \left\langle \frac{\partial^2 \mathcal{L}}{\partial\theta_\mu \partial\theta_\nu} \right\rangle = \left\langle \mathcal{L}_{\mu\nu} \right\rangle \tag{3.39}$$

Assuming there's a global maximum of likelihood at $\boldsymbol{\theta} = \boldsymbol{\theta}_0$, it can be expanded around that point in θ, giving

$$\mathcal{L} \approx \mathcal{L}_0 + \frac{1}{2}(\boldsymbol{\theta} - \boldsymbol{\theta}_0)^T \mathcal{L}_{\mu\nu}(\boldsymbol{\theta} - \boldsymbol{\theta}_0). \tag{3.40}$$

Going back to the likelihood L, it's immediately obvious that it now follows a multivariate Gaussian with covariance $C^{-1} = \partial_\mu \partial_\nu \mathcal{L}$.

$$L \propto \exp\left(-\frac{1}{2}(\boldsymbol{\theta} - \boldsymbol{\theta}_0)^T C^{-1} (\boldsymbol{\theta} - \boldsymbol{\theta}_0)\right) \tag{3.41}$$

From which the Fisher matrix can be inferred (see appendix A.1)

$$F_{\mu\nu} = \frac{1}{2}\mathrm{tr}\left[C^{-1}\partial_\mu C\, C^{-1}\partial_\nu C\right]. \tag{3.42}$$

Up to an angular scale ℓ, there will be $2\ell + 1$ independent measurements due to multiplicity and statistical isotropy, therefore the total Fisher matrix becomes a sum over ℓ with the multiplicity factor. We furthermore need to correct for an incomplete survey of the sky by multiplying by f_sky, thus $F_{\mu\nu}$ becomes

$$F_{\mu\nu} = f_\mathrm{sky} \sum_\ell \frac{2\ell + 1}{2} \mathrm{tr}\left[C^{-1}\partial_\mu C\, C^{-1}\partial_\nu C\right]. \tag{3.43}$$

In Fig. (3.5), it becomes apparent why increasing the bin number increases precision. More spectra give rise to more information about how the spectra change with a parameter (here: Ω_m).

We find the conditional errors for a parameter μ as $\sigma_\mu^c = \sqrt{F^{-1}_{\mu\mu}}$ and the marginal errors $\sigma_\mu^m = \sqrt{(F^{-1})_{\mu\mu}}$.

Since the Fisher matrix measures statistical errors for Gaussian distributions, in our case, the signal to noise-ratio $\Sigma = S_0/\sigma_S$ is related to it. We can express the statistical error in terms of the Fisher matrix,

$$\frac{1}{\sigma_S^2} = f_{\rm sky} \sum_\ell \frac{2\ell+1}{2} \mathrm{tr}\left[C^{-1}\partial_{S_0} C\, C^{-1}\partial_{S_0} C\right], \tag{3.44}$$

if we can assume additivity, i.e. $C(\ell) = S(\ell) + N(\ell)$, where S is the signal we're interested in (be it intrinsic alignments or the lensing spectra) and N the noise part, wich includes the shape noise and anything we might classify as such (such as IAs again) and is independent of S, we can thus write generally

$$\Sigma^2 = f_{\rm sky} \sum_\ell \frac{2\ell+1}{2} \mathrm{tr}\left[C^{-1} S\, C^{-1} S\right]. \tag{3.45}$$

One source for noise that all of the applications in this work have in common, is the shape noise of the galaxies. As mentioned above, the shape noise $\sigma_\epsilon^2 n_{\rm bin}/\bar{n}$ increases with bin size, decreases with galaxy sample size, and has a free parameter that quantifies its amplitude. We set it to $\sigma_\epsilon = 0.3$ for this work. Furthermore, it is constant in ℓ, such that if $\propto \ell^2 C(\ell)$ is plotted, as is usual, the noise becomes a slope in a logarithmic plot.

One of the goals of this thesis is to set limits on the induced biases – or systematic errors – induced by intrinsic alignments on a cosmic weak lensing survey. So, we need to distinguish a true model, C_t, from a false (or oversimplified) model, C_f, which the data sampled from the true model is fitted. This will lead to an error in the best fit parameters, reducing the accuracy of parameter inference. To quantify this, we use the same formalism shown in Schaefer & Heisenberg (2012), a generalisation of Taburet et al. (2009) and Amara & Réfrégier (2008). A more detailed derivation can be found in appendix A.2

If we limit ourselves to small deviations from the true model and if we assume Gaussian statistics, we can quantify the systematic error δ_μ as

$$\delta_\mu = \sum_\nu G^{-1}_{\mu\nu} a_\nu \tag{3.46}$$

with

$$G_{\mu\nu} = \sum_\ell \frac{2(\ell+1)}{2} \mathrm{tr}\left[\left(C_f^{-1}\left(\partial_\mu\partial_\nu C_f\right)\left(C_f^{-1}C_t - \mathrm{id}\right)\right) - \left(C_f^{-1}\left(\partial_\mu C_f\right) C_f^{-1}\left(\partial_\nu C_f\right)\left(2C_f^{-1}C_t - \mathrm{id}\right)\right)\right], \tag{3.47}$$

and

$$a_\mu = \sum_\ell \frac{2(\ell+1)}{2} \mathrm{tr}\left[C_f^{-1}\left(\partial_\mu C_f\right)\left(\mathrm{id} - C_f^{-1}C_t\right)\right]. \tag{3.48}$$

In order to quantify the systematic error, a useful construct is the figure of bias Q,

$$Q^2 = \sum_{\mu\nu} F_{\mu\nu}\delta_\mu\delta_\nu, \tag{3.49}$$

which expresses the systematics of a parameter in terms of its statistical uncertainty. It is closely connected to the Kullback-Leibler-divergence $D_{\rm KL}$ (Kullback & Leibler, 1951), which quantifies how close two probability distributions are,

$$D_{\rm KL} = \int \mathrm{d}^N\theta \mathcal{L}_t(\boldsymbol{\theta}) \ln\left(\frac{\mathcal{L}_t(\boldsymbol{\theta})}{\mathcal{L}_f(\boldsymbol{\theta})}\right), \tag{3.50}$$

namely if $\mathcal{L}$ are Guassian, and if the covariance shift from t to f is small (which they are by definition), we have $D_{\mathrm{KL}} = Q^2/2$ (Tugendhat & Schaefer, 2018).

3.6 Euclid and the Future of Weak Lensing Surveys

Euclid[2] is a satellite mission dedicated to cosmology. It will map billions of galaxies up to a redshift of $z = 2$ and take photometric redshifts of most of them using four filters in the visible spectrum. The redshift measurements will include tens of millions of spectroscopic redshifts. This will bring an unprecedented wealth of data for weak lensing and BAO observations. The main goal is among others to further constrain the value of w, the dark energy equation of state. Euclid will be to weak lensing what WMAP was to the CMB, bringing precision that has not been achieved previously and mapping a great portion of the sky (as opposed to the limited sky coverage of ground–based observations in both cases).

One of the main features of Euclid will be the colour information. It might be possible to divide the lensing survey into red and blue subsets, which has a potential of bringing great improvements to the accuracy of the survey. Since Euclid is statistically so precise, it will run into problems with many systematics. One of which are the intrinsic alignments of galaxies. In order to be as accurate as WMAP was, Euclid has to deal with many of those, just like WMAP had to deal with secondary anisotropies. In the end, some of them ended up being great sources of information, like the Sunyaev–Zel'dovich-effect (Sunyaev & Zeldovich, 1970). Others were studied in detail as well, but were never quite observable, like the nonlinear integrated Sachs-Wolfe effect (Rees & Sciama, 1968). In order to know into which one of those categories intrinsic alignments fall, it is essential to model them and construct consistency checks in order to give observations the chance to detect their traces and determine which models can be used to describe them sufficiently.

Previous surveys have indeed seen the first glimpses of IAs (Heymans et al., 2013), and hence it is imporant to gauge whether the models work with available observational evidence.

Future surveys might open a whole new into lensing. A large radio survey like the square kilometre array[3] (SKA) or a second iteration of it might be able to see lensing in neutral hydrogen gas (e.g. Brown et al., 2015; Harrison et al., 2016), and thus could cross-correlate this with optical surveys. Since the hydrogen traces the halo differently than the stellar component, that might be an interesting source on the galaxy biasing mechanism and galaxy formation itself. Another possibility would be to measure the polarisation of the light as well as the sources' ellipticity, possibly in a radio survey (Brown & Battye, Brown & Battye); as polarisation is not affected by weak lensing, as discussed before (see section 2.3), this could be a way of effectively disconnect lensing and intrinsic ellipticities.

In table (3.1), the differences between current and future surveys can be seen. While Euclid is actually more shallow than the others, it is by an immense margin more complete in its sky coverage. This extreme width of the survey is whence most of its statistical superiority will come.

[2] https://www.euclid-ec.org
[3] https://www.skatelescope.org/

	Euclid	CFHTLenS	DES
z_{median}	0.64	0.7	0.68
β	1.5	1.5	1.5
f_{sky}	0.5	0.004	0.12
$n_{\text{mean, per sq arcmin}}$	40	11	12
$n_{\text{mean, per steradian}}$	4.727×10^8	1.23×10^8	1.42×10^8

Table 3.1: Applicable parameters for the galaxy distribution function (equation (3.20)) for three weak lensing surveys mentioned and used in this work, including f_{sky}. Note that $n_{\text{mean, per steradian}}$ is denoted as $\bar{n}$ in this work for convenience. Sources: Euclid: Laureijs et al. (2011) CFHTLenS: Heymans et al. (2013), DES: Weller et al. (2008).

Part II

Models for Intrinsic Alignments and their Effects and Implications

4 Two Models for Intrinsic Alignment of Galaxies

4.1 Using multiple models for Intrinsic Alignments

In this work, I will consider two distinct models for intrinsic alignments of galaxies, one for spiral galaxies and one for elliptical galaxies. Each model has been studied before – e.g. Theuns & Catelan (1997); Natarajan et al. (2001); Crittenden et al. (2001), Schaefer (2009), Kirk et al. (2010) ,Capranico et al. (2013) for tidal torquing and Hirata & Seljak (2004); Blazek et al. (2011) and Blazek et al. (2015) for tidal shearing and most recently Blazek et al. (2017) for something similar to this work.

Here, both are considered to apply to one morphological class at a time in a realistic mix of galaxies in the survey. I quantify this mix by the spiral fraction q, which gives the amount of spiral galaxies contained in the total galaxy sample.

The spiral fraction q is set to be of a constant value, as the main goal of this work was to investigate the relative effect of the alignment models and their mix on a near-future weak lensing survey. It is easily pointed out that the relative amount of spiral galaxies varies with time (i.e. redshift z), but also possibly with environment parameters of the galaxies in question such as local matter density, merger history, and so on. The largest impact would probably be q being a function of z, since redshift is a not only a parameter appearing in the calculations of ellipticity spectra but is also the dimension used for the tomographic splitting of the galaxy sample. Therefore, a heavy dependence of the spiral fraction on redshift would change the correlation strengths between different bins. Yet, the dependence of the spiral fraction on redshift is at least weak for smaller redshifts (see e.g. Dressler et al., 1997; Tasca et mult., 2009). Technically, it would be not a difficult task to replace q with a function $q(z, \delta, \dots)$; it would, however, blur our results for the important part of this work, i.e. determining the impact of the intrinsic alignment signal on a weak lensing survey. The same argument was made in Tugendhat & Schaefer (2018).

There are only three free parameters that describe the relation of the intrinsic alignment signal's amplitude strength to weak lensing: The mixing relation of both models that has just been discussed, the free amplitude parameter for the tidal torquing model, and the free amplitude parameter for the tidal shear. These are called q, A, and D in this work. Furthermore, all three are set to be constant. The reason for A and D to be set constant will be given in their respective sections.

4.2 Tidal Torque: Alignment of Spiral Galaxies

The idea that the angular momentum of galaxies is seeded by their initial conditions and surroundings is not a new one and has been both discussed analytically and investigated and confirmed via N-body simulations long before (Peebles, 1969; Doroshkevich, 1970; White, 1984). The idea behind tidal torquing is that a (proto)galaxy halo is sheared from gravitational tidal forces, whereby a torque is generated. Barring any interaction with other halos (such as mergers or close encounters), the halo and its stellar component keep this angular momentum after they decouple from the background evolution during collapse, increasing their rotational velocity. It should be noted that this process happens during the strictly linear structure formation period and is therefore only dependent on the statistics of the linear power spectrum $P_{\rm lin}(k)$. The foundations of this model are laid

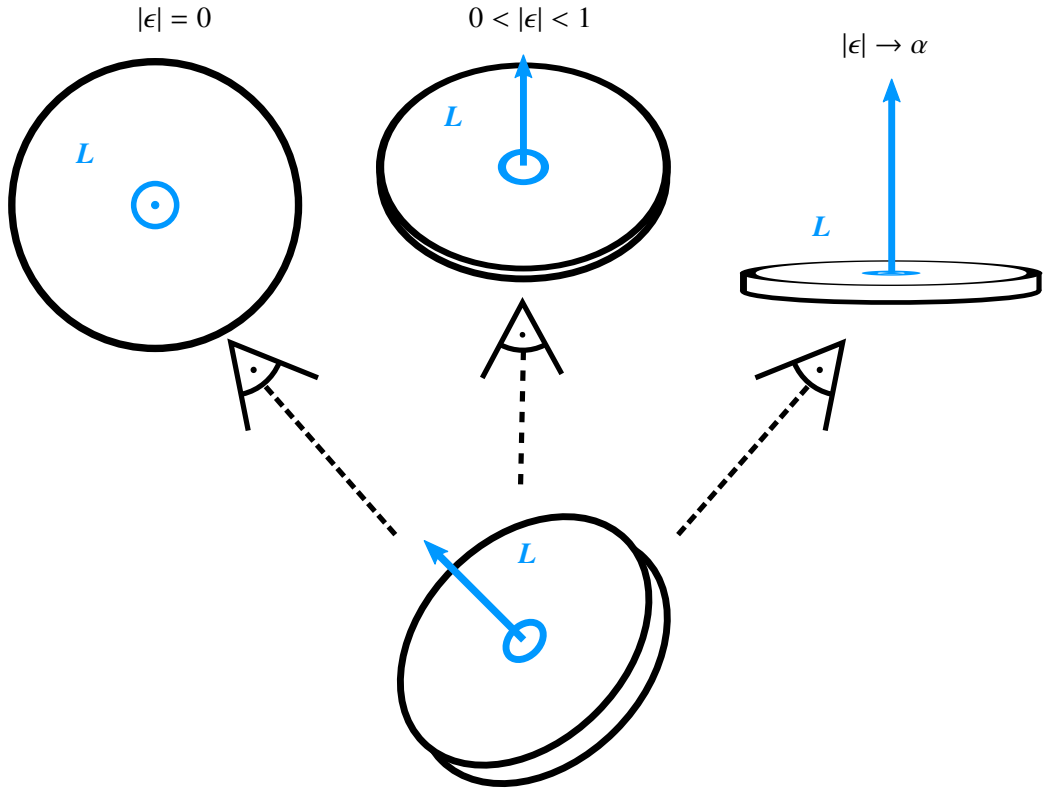

Figure 4.1: The observed ellipticity depends on the angle of the observer relative to the angular momentum vector $\boldsymbol{L}$. The smaller the projection of $\boldsymbol{L}$, the smaller the ellipticity. Due to finite disc thickness, the maximum ellipticity observed is $\alpha < 1$, which is set to $\alpha = 0.25$ in this work.

by e.g. Lee & Pen (2000) and Crittenden et al. (2001), but the derivation given here follows Schaefer (2009), Kiessling et al. (2015a), and Schaefer & Merkel (2015) in order to keep the notation in this work congruent.
A good starting point in dealing with spinning up galaxies is defining angular momentum $\boldsymbol{L}(t)$ in the Eulerian reference frame,

$$L_k(t) = \int_V \mathrm{d}^3 r \, (\boldsymbol{r} - \boldsymbol{r}')_i \boldsymbol{v}_j(\boldsymbol{r},t) \varepsilon_{ijk} \, \rho(\boldsymbol{r}, t), \tag{4.1}$$

where $\boldsymbol{v}$ is the local velocity, ρ is the local density, $\boldsymbol{r}'$ is the location of the centre of gravity and ε_{ijk} is the Levi-Cività-symbol. Note that the indices i and j here denote the three spatial coordinates x, y, z, not the tomographic bins.
This following calculation (as seen in e.g. Schaefer, 2009) is to show an important feature of the tidal torque model, namely that there can only be nonzero angular momentum iff the external tidal shear tensor and the tensor of inertia of the halo are misaligned, i.e. the same operation cannot bring them both into their respective eigensystems. The intuitive graphic representation of this fact is that in Fig. (4.3), the displacement-vectors must change in length or direction as a function of their origin in order to have rotation in the Lagrangian frame.

Let's assume $\rho(\boldsymbol{r},t) \simeq \rho_0$, since this initial angular momentum should be seeded at very early times, when $\delta \ll 1$. Changing from Eulerian coordinates $\boldsymbol{r}$ to Lagrangian coordinates $\boldsymbol{x}$ with initial positions $\boldsymbol{q}$, we can approximate the velocity $\dot{\boldsymbol{x}}$ with the Zel'dovic-approximation (Zel'dovich, 1970),

$$\begin{aligned} \boldsymbol{x}(\boldsymbol{q}, t) &= \boldsymbol{q} - D_+(t) \, \nabla\Phi(\boldsymbol{q}), \\ \dot{\boldsymbol{x}} &= -\dot{D}_+ \, \nabla\Phi(\boldsymbol{q}). \end{aligned} \tag{4.2}$$

Assuming that $\nabla\Phi$ can be approximated with a second order Taylor expansion, we get for $\dot{\boldsymbol{x}}$

$$\dot{x}_i = -\dot{D}_+ \left(\Phi_i(\boldsymbol{q}') + (\boldsymbol{q} - \boldsymbol{q}')_j \Phi_{ij}(\boldsymbol{q}')\right), \tag{4.3}$$

where $\partial_a \Phi := \Phi_a$. As $\Phi_a(\boldsymbol{q}')$ is just a constant displacement, we disregard it. We can also approximate $\boldsymbol{L}$ in terms of $\boldsymbol{q}$ instead of in terms of $\boldsymbol{x}$; furthermore, in co-moving coordinates, we gain a factor of a for each $\boldsymbol{r} \to \boldsymbol{x}$ and $\boldsymbol{v} \to \dot{\boldsymbol{x}}$ and another factor of a^3 for the volume $V \to V_\mathrm{L}$, such that

$$L_k(t) = -\dot{D}_+ \rho_0 a^5 \int_{V_\mathrm{L}} \mathrm{d}^3 q \, (\boldsymbol{q} - \boldsymbol{q}')_i \left((\boldsymbol{q} - \boldsymbol{q}')_l \Phi_{jl}(\boldsymbol{q}')\right) \varepsilon_{ijk}. \tag{4.4}$$

Now, exchanging the indices and using the antisymmetry of ε_{ijk}, the negative sign vanishes and we recognise that the inertia tensor I_{ij} is

$$I_{ij} = \rho_0 a^3 \int_{V_\mathrm{L}} \mathrm{d}^3 q (\boldsymbol{q} - \boldsymbol{q}')_i (\boldsymbol{q} - \boldsymbol{q}')_j, \tag{4.5}$$

which enables us to write the i-component of the angular momentum $\boldsymbol{L}$ in terms of the scale factor, the growth function, and both the tensor of inertia and the tidal shear tensor,

$$L_i(t) = a^2 \dot{D}_+ \varepsilon_{ijk} I_{jl} \Phi_{lk}. \tag{4.6}$$

Because of the l-summation, the antisymmetric Levi-Cività-symbol only projects out the antisymmetric part of the combination $I_{jl}\Phi_{lk}$. This part, in turn, is only nonzero if the commutator [I,Φ] does not vanish, meaning the two tensors must not share the same eigensystem if we require L_i to be nonzero, proving what I claimed more graphically above.

It has been shown (e.g. Teklu et al., 2015; Tenneti et al., 2016) that the link between angular momentum and initial conditions thus established can predict the direction of $\boldsymbol{L}$ reasonably well, albeit lacks this precision for its magnitude $|\boldsymbol{L}| = L$. As the observed ellipticity of a rotating disc model galaxy does not depend on the magnitude of the angular momentum but only on its direction (see Fig. (4.1)), it is permissable to continue with the normalised angular momentum $\hat{\boldsymbol{L}} = \boldsymbol{L}/L$ and the unit-normalised ($\hat{\Phi}_{ij}\hat{\Phi}_{ji} = 1$) traceless ($\hat{\Phi}_{ii}\hat{\Phi}_{ii} = 0$) tidal shear $\hat{\Phi}_{ij}$.

Starting with a gaussian distribution p for angular momenta $\boldsymbol{L}$ given a tidal shear $\Phi_{\alpha\beta}$,

$$p(\hat{\boldsymbol{L}}|\Phi_{ij}) = \left((2\pi)^3 \det C\right)^{-1/2} \exp\left\{-\frac{1}{2}\hat{L}_k (C^{-1})_{kl} \hat{L}_l\right\} \tag{4.7}$$

with the covariance matrix (Lee & Pen, 2001)

$$C_{ij} = \left\langle \hat{L}_i \hat{L}_j \right\rangle = \frac{1}{3}\left[\frac{1+A}{3}\delta_{ij} - A\hat{\Phi}_{il}\hat{\Phi}_{lj}\right], \tag{4.8}$$

with δ_{ij} denoting the Kronecker delta. The misalignment parameter A is the aforementioned free parameter in this model and quantifies the strength of the correlation between the angular momenta and the tidal shear. It is measured to be $A \simeq 0.25$ in numerical simulations for haloes of sizes typical of spiral galaxies. I will assume A to be constant with time because the angular momentum generation and the resulting alignment happens roughly at the same time for all observed galaxies, such that a later sudden change in A wouldn't affect the measurement at all.

Angular momentum and ellipticity are easily related once a coordinate system is chosen (see Fig. (4.1)); let's set z as the line of sight, such that

$$\begin{aligned}\epsilon_+ &= \alpha\frac{\hat{L}_y^2 - \hat{L}_x^2}{1+\hat{L}_z^2},\\ \epsilon_\times &= 2\alpha\frac{\hat{L}_x\hat{L}_y}{1+\hat{L}_z^2}.\end{aligned} \tag{4.9}$$

The thickness parameter α, chosen to be $\alpha = 0.25$, damps the influence of $\hat{L}$ on the ellipticity. Intuitively, as galaxies have finite thickness in reality, this prevents galaxies seen edge-on ($L_z = 0$) to have $|\epsilon| = 1$, which is illustrated by calculating the modulus of ϵ:

$$|\epsilon| = \alpha\frac{1-\hat{L}_z^2}{1+\hat{L}_z^2} \tag{4.10}$$

The complex ellipticity can then be expressed as (just as in Crittenden et al. (2001) eq. (28) or Schaefer & Merkel (2015) eq. (19))

$$\epsilon(\hat{\Phi}) = \frac{A\alpha}{2}\Big(\underbrace{\hat{\Phi}_{xj}\hat{\Phi}_{jx} - \hat{\Phi}_{yj}\hat{\Phi}_{jy}}_{\epsilon_+} - \mathrm{i}\underbrace{2\hat{\Phi}_{xj}\hat{\Phi}_{jy}}_{-\epsilon_\times}\Big). \tag{4.11}$$

Here, it is obvious why this model is also dubbed 'quadratic alignment' (in contrast to 'linear alignment for the model discussed in section 4.3): the tidal shear tensor appears in squared form $\hat{\Phi}_{ai}\hat{\Phi}_{ia}$, ($a \in \{x,y\}$).

The modulus of ϵ can also be calculated, $\epsilon_s = |\epsilon| = \sqrt{\epsilon_+^2 + \epsilon_\times^2}$:

$$\epsilon_s = \frac{3}{4}A\alpha\hat{\Phi}_{zj}\hat{\Phi}_{jz}, \tag{4.12}$$

where j is a summation index.

Two key differences to the linear model will become clear in section 4.3: For one, the quadratic model is independent of the magnitude of Φ_{ij}, hence the normalised versions. For another, since the induced angular momenta and ellipticities are only dependent on the initial conditions, the fully nonlinear power spectrum is not needed here.
The next step is usually to build ellipticity correlation functions and angular ellipticity spectra from this in order to compare it to weak lensing. This will be done in section 5.1.

It should be mentioned that other alignment models for angular momenta exist – such as starting with vorticity (Libeskind et al., 2013) rather than torquing.

4.3 Tidal Shear: Alignment of Elliptical Galaxies

For elliptical galaxies, I assume a much simpler model. The idea is that their ellipticities are directly and linearly linked to tidal shear. An external shear field affects the halo in which the elliptical galaxy sits by stretching and compressing different axes and thus affects the stellar component as well (Camelio & Lombardi, 2015).
Mathematically, this is rectified by showing the perturbation of a virialised system with spherical symmetry (see Tugendhat & Schaefer, 2018, this entire section follows the arguments given therein closely). The particles in such a setup adhere to the Jeans-equation, which has the anisotropic solution

$$\rho(\boldsymbol{x}) \propto \exp\left\{-\frac{\Phi(\boldsymbol{x})}{\sigma^2}\right\}, \tag{4.13}$$

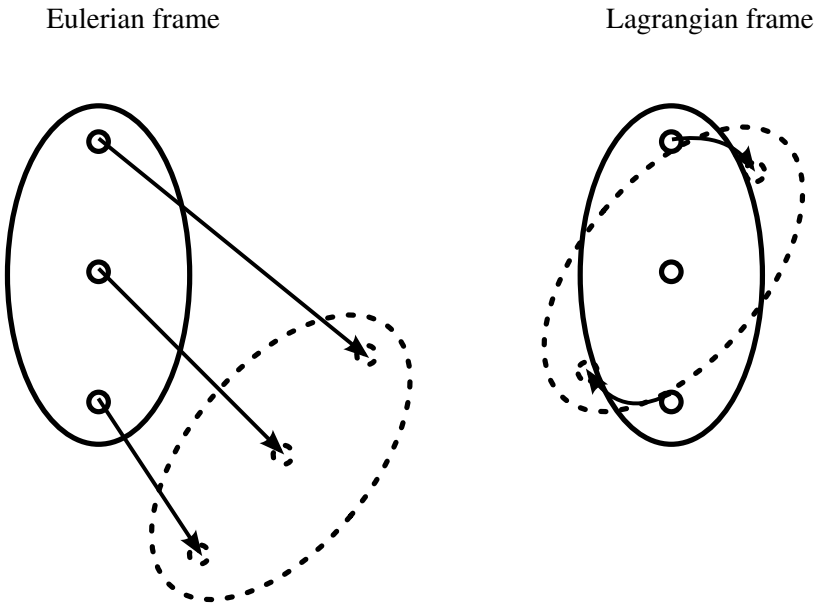

Figure 4.2: Tidal torquing. Adapted from Schaefer (2009), a nonspherical (proto-)halo, translated in a linear way in the Euler frame is experiences as a rotation in the Lagrangian frame of the object.

where ρ is the particle (or stellar) density and σ^2 is the velocity dispersion measure. Assuming the halo sits near a potential minimum, we can assume there to be a (much weaker) tidal shear and expand in the form of a quadrupole field (the first order would be zero as we are in a minimum):

$$\Phi(\boldsymbol{x}) \to \Phi(\boldsymbol{x}) + \frac{1}{2}\Phi_{ij}(\boldsymbol{x'})x_i x_j. \tag{4.14}$$

The tidal shear is evaluated at the centre of mass of the halo, $\boldsymbol{x} = \boldsymbol{x'}$. Plugging this new potential in equation (4.13), we have

$$\rho(\boldsymbol{x}) \propto \exp\left\{-\frac{\Phi(\boldsymbol{x})}{\sigma^2}\right\} \cdot \left(1 - \frac{1}{2\sigma^2}\Phi_{ij}(\boldsymbol{x'})x_i x_j\right), \tag{4.15}$$

where we can now identify the ellipticity with a linear function in Φ_{ij} by comparing ρ to the tensor of second brightness moments (see Bartelmann & Schneider, 2001a; Piras et al., 2017). The proportionality constant between the tidal shear and ellipticity shall be called D, and it can indeed be shown that it is constant in mass and redshift (Piras et al., 2017; Tugendhat & Schaefer, 2018):

Looking at the dimensions in equation (4.15), the tidal shear is measured in σ^2/R^2; assuming virial equilibrium, the specific kinetic energy must be equal to the specific potential energy GM/R. The specific kinetic energy in the 'thermal' motion is $\propto \sigma^2$. Furthermore is the mass M proportional to R^3. Then

$$\frac{\sigma^2}{R^2} = \frac{GM}{R^3} = \text{const.} \tag{4.16}$$

Thus, we don't expect D to vary over mass or redshift ranges. The ellipticity in this model is truly only linearly dependent on magnitude and direction of the tidal shear. Let me also point out that this model's inherent velocity scale seems to be σ^2, marking typical scales for galaxies (and the implicitly underlying Newtonian approach), whereas in 'vanilla' gravitational lensing, the velocity scale of the gravitational potential is c^2, the natural scale for Einsteinian Gravity.

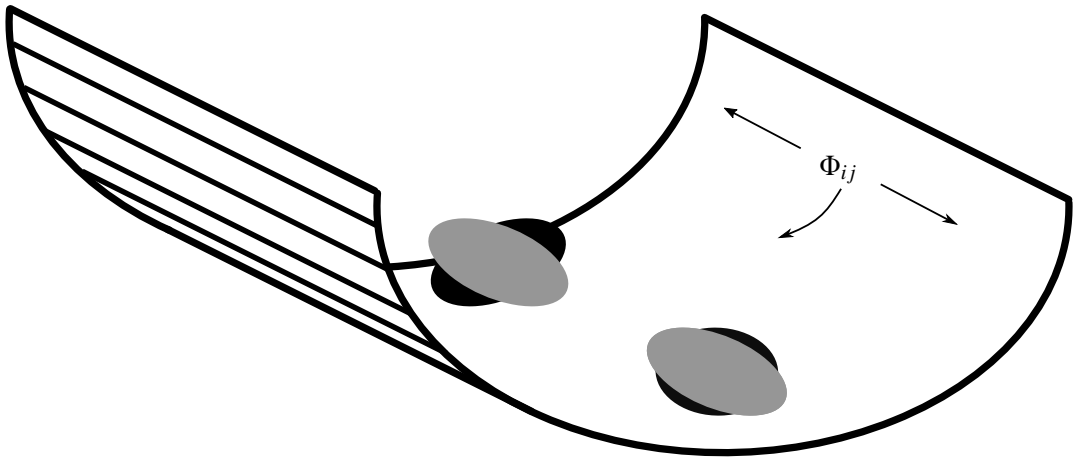

Figure 4.3: Tidal Shear: Adapted from Kiessling et al. (2015a), two original haloes (black ellipses) sit in a tidal shear field Φ_{ij} and end up with an ellipticity that is imposed by the external field (grey ellipses).

Choosing the z-axis to again act as the line of sight, this yields the complex ellipticity

$$\epsilon(\Phi) = D\Big(\underbrace{\Phi_{xx} - \Phi_{yy}}_{\epsilon_+} + \mathrm{i}\,\underbrace{2\Phi_{xy}}_{\epsilon_\times}\Big). \tag{4.17}$$

This model – just like the one in section 4.2 – assumes the galaxy to be non-interacting with its neighbouring environment save for the external fields. Recent interactions like mergers or close encounters would give rise to additional complications. Particularly in galaxy clusters, this model must be taken with a grain of salt (Hao et al., 2011). For a cosmic shear survey however, it is a good starting point to model alignment in elliptical galaxies.

5 Intrinsic Alignments within the Framework of Tomographic Weak Lensing

Now that the ellipticities for the galaxy types can be calculated from the tidal fields as shown in the previous chapter, we can find the correlation functions and then Fourier-transform to end up with an angular power spectrum.

Therefore, in this chapter, I will derive the correlation functions and angular power spectra for elliptical and spiral galaxy alignment analogous to Schaefer & Merkel (2015) and Tugendhat & Schaefer (2018), make the case for the choice of a smoothed power spectrum $\mathcal{S}[P_\Phi(k)]$ for calculating the alignment spectra for each model, fix the free parameter for the elliptical model D and show results from numerical calculations of the spectra.

5.1 Tidal Shear: From Correlation Functions to Angular Spectra

The correlation function $\left\langle \epsilon_a \epsilon'_b \right\rangle$ are going to contain the second derivatives of the potential, $\Phi_{\alpha\beta}$, therefore we calculate those first and will collect the results for the different ellipticity correlations. The two point correlation function of the tidal shear is

$$\begin{aligned}\left\langle \Phi_{\alpha\beta}(\boldsymbol{x})\Phi_{\gamma\delta}(\boldsymbol{x'}) \right\rangle = C_{\alpha\beta\gamma\delta}(r) = &\left(\delta_{\alpha\beta}\delta_{\gamma\delta} + \delta_{\alpha\gamma}\delta_{\beta\delta} + \delta_{\alpha\delta}\delta_{\beta\gamma}\right)\zeta_2(r) \\ &+ \left(\delta_{\alpha\beta}\hat{r}_\gamma\hat{r}_\delta + \delta_{\alpha\gamma}\hat{r}_\beta\hat{r}_\delta + \delta_{\alpha\delta}\hat{r}_\beta\hat{r}_\gamma + \delta_{\beta\gamma}\hat{r}_\alpha\hat{r}_\delta + \delta_{\beta\delta}\hat{r}_\alpha\hat{r}_\gamma + \delta_{\gamma\delta}\hat{r}_\alpha\hat{r}_\beta\right)\zeta_3(r) \\ &+ \left(\hat{r}_\alpha\hat{r}_\beta\hat{r}_\gamma\hat{r}_\delta\right)\zeta_4(r), \end{aligned} \tag{5.1}$$

with the weighted integrals over the power spectrum ζ,

$$\zeta_n(r) = \frac{(-1)^n}{r^{4-n}} \int \frac{k^{n+2}\mathrm{d}k}{2\pi^2} P_\Phi(k)\, j_n(kr). \tag{5.2}$$

The vector $\boldsymbol{r}$ between the two points is chosen such that $\boldsymbol{r} = r\,(\sin(\alpha), 0, \cos(\alpha))^T$, so that an expression for the correlators can be found that is dependent on r and α. For a full derivation see chapter B in the appendix. This yields the non-vanishing ellipticity correlations (Tugendhat & Schaefer, 2018),

$$\left\langle \epsilon_+ \epsilon'_+ \right\rangle(\boldsymbol{r}) = D^2\left(4\zeta_2(r) + 4\sin^2(\alpha)\zeta_3(r) + \sin^4(\alpha)\zeta_4(r)\right), \tag{5.3}$$

$$\left\langle \epsilon_\times \epsilon'_\times \right\rangle(\boldsymbol{r}) = 4D^2\left(\zeta_2(r) + \sin^2(\alpha)\zeta_3(r)\right), \tag{5.4}$$

$$\left\langle \epsilon_\mathrm{s} \epsilon'_\mathrm{s} \right\rangle(\boldsymbol{r}) = D^2\left(8\zeta_2(r) + 8\sin^2(\alpha)\zeta_3(r) + \sin^4(\alpha)\zeta_4(r)\right), \tag{5.5}$$

$$\left\langle \epsilon_\mathrm{s} \epsilon'_+ \right\rangle(\boldsymbol{r}) = D^2\left(-6\zeta_3(r) - \sin^4(\alpha)\zeta_4(r)\right). \tag{5.6}$$

This is all done in real space rather than Fourier-space as the tidal torque model also works in real space; the idea is to keep the two models comparable, in order to easily recognise their differences and common features.

Blazek et al. (2015) are doing the same in Fourier space and end up with equivalent results. Going now from ($\boldsymbol{r}$,α) to θ in order to end up with two-dimensional correlation functions requires a Limber projection in real space (Limber, 1954; Loverde & Afshordi, 2008),

$$\left\langle \epsilon_{a,i}\, \epsilon'_{b,i} \right\rangle(\theta) = \int_0^{\chi_H} \mathrm{d}\chi\ n_i(\chi) \int_{\chi_i}^{\chi_{i+1}} \mathrm{d}\chi'\, n_i(\chi') \left\langle \epsilon_a\, \epsilon'_b \right\rangle(\boldsymbol{r}(\chi,\chi')) \tag{5.7}$$

where $n(\chi)$ is the same galaxy distribution function as for weak lensing, the first index denotes the type, a,$b \in \{+,\times,s\}$, and the index i stands for the ith tomographic bin. It is noteworthy that for all the similarity and analogy with weak lensing (chapter 3, in particular section 3.2) in this case, the inner integration is not limited by the outer one, as in equation (3.36). This reflects the fact that alignment doesn't have to happen between the observer and the source. Two sources can be aligned by structures behind them (from the observer's point of view). Defining the appropriate correlation functions,

$$C^{\epsilon,II}_{+,i}(\theta) = \left\langle \epsilon_{+,i}\, \epsilon'_{+,i} \right\rangle + \left\langle \epsilon_{\times,i}\, \epsilon'_{\times,i} \right\rangle, \tag{5.8}$$

$$C^{\epsilon,II}_{-,i}(\theta) = \left\langle \epsilon_{+,i}\, \epsilon'_{+,i} \right\rangle - \left\langle \epsilon_{\times,i}\, \epsilon'_{\times,i} \right\rangle, \tag{5.9}$$

$$C^{\epsilon,II}_{S,i}(\theta) = \left\langle \epsilon_{s,i}\, \epsilon'_{s,i} \right\rangle, \tag{5.10}$$

$$C^{\epsilon,II}_{C,i}(\theta) = \left\langle \epsilon_{s,i}\, \epsilon'_{+,i} \right\rangle, \tag{5.11}$$

we can calculate the E– and B–mode parity modes as well as the scalar- and cross-spectra via a Fourier transform,

$$C^{\epsilon,II}_{E,i}(\ell) = \pi \int \theta \mathrm{d}\theta\ \left(C^{\epsilon,II}_{+,i}(\theta)\, J_0(\ell\theta) + C^{\epsilon,II}_{-,i}(\theta) J_4(\ell\theta) \right), \tag{5.12}$$

$$C^{\epsilon,II}_{B,i}(\ell) = \pi \int \theta \mathrm{d}\theta\ \left(C^{\epsilon,II}_{+,i}(\theta)\, J_0(\ell\theta) - C^{\epsilon,II}_{-,i}(\theta) J_4(\ell\theta) \right), \tag{5.13}$$

$$C^{\epsilon,II}_{S,i}(\ell) = 2\pi \int \theta \mathrm{d}\theta\ C^{\epsilon,II}_{S,i}(\theta)\, J_2(\ell\theta), \tag{5.14}$$

$$C^{\epsilon,II}_{C,i}(\ell) = 2\pi \int \theta \mathrm{d}\theta\ C^{\epsilon,II}_{C,i}(\theta)\, J_0(\ell\theta). \tag{5.15}$$

The above results are all part of the II–alignment, as we're only considering ϵ–autocorrelations.

As already stated in section 3.3, there are in fact two types of alignment correlations; the cross–correlation between weak lensing and alignment is called GI–alignment. Their correlations are straightforward to find, as they only differ by a sign and their respective weighting – by definition of the two ellipticities, (equations 3.15 and 4.17). Therefore,

$$\langle \gamma_+ \epsilon'_+ \rangle(\boldsymbol{r}) = -\int_0^{\chi_H} \mathrm{d}\chi\ \frac{W(\chi)}{D}\ \langle \epsilon_+\, \epsilon'_+ \rangle(\boldsymbol{r}), \tag{5.16}$$

$$\langle \gamma_\times \epsilon'_\times \rangle(\boldsymbol{r}) = \int_0^{\chi_H} \mathrm{d}\chi\ \frac{W(\chi)}{D}\ \langle \epsilon_\times\, \epsilon'_\times \rangle(\boldsymbol{r}), \tag{5.17}$$

$$\langle \gamma_s \epsilon'_s \rangle(\boldsymbol{r}) = \int_0^{\chi_H} \mathrm{d}\chi\ \frac{W(\chi)}{D}\ \langle \epsilon_s\, \epsilon'_s \rangle(\boldsymbol{r}), \tag{5.18}$$

$$\langle \gamma_s \epsilon'_+ \rangle (\boldsymbol{r}) = -\int_0^{\chi_H} \mathrm{d}\chi \ \frac{W(\chi)}{D} \ \langle \epsilon_s \, \epsilon'_+ \rangle (\boldsymbol{r}). \tag{5.19}$$

The Limber projections works analogous to the II–case,

$$\left\langle \gamma_{a,i} \, \epsilon'_{b,j} \right\rangle (\theta) = \mp \int_0^{\chi_H} \mathrm{d}\chi \ \int_{\chi_j}^{\chi_{j+1}} \mathrm{d}\chi' \frac{W_i(\chi) \, n_j(\chi')}{D} \ \left\langle \epsilon_a \, \epsilon'_b \right\rangle \left(\boldsymbol{r}(\chi, \chi') \right). \tag{5.20}$$

Again, $n(\chi)$ is the galaxy distribution, W_i is the lensing weighting function, the first index stands for the type, a,$b \in \{+, \times, s\}$ and the negative sign is for $a \vee b = +$ and the positive one for $a \wedge b \neq +$. Here, we have two indices for the tomographic bins, i and j. This is because GI–alignments don't vanish on the off-diagonals; we can also immediately see that GI/IG–alignments are asymmetric, and exchanging i and j would turn IG into GI and vice-versa. However, gravitational lensing can only work with structures in front of the sources, thus IG-correlation aren't physically observable.

In order to keep statistical isotropy, however, I will symmetrise the correlation matrix and thus discard the information that in a GI-correlation the more distant galaxy is the lensed one, which is would be readily available with galaxy redshifts. Therefore, by hand I set

$$C^{GI}_{a,ij}(\theta) = C^{GI}_{a,ji}(\theta) = \frac{1}{2} \left\langle \gamma_{a,i} \, \epsilon'_{a,j} \right\rangle. \tag{5.21}$$

The correlation functions analogous to the II case are then

$$2 \, C^{\epsilon,GI}_{+,ij}(\theta) = \left\langle \gamma_{+,i} \, \epsilon'_{+,j} \right\rangle + \left\langle \gamma_{\times,i} \, \epsilon'_{\times,j} \right\rangle, \tag{5.22}$$

$$2 \, C^{\epsilon,GI}_{-,ij}(\theta) = \left\langle \gamma_{+,i} \, \epsilon'_{+,j} \right\rangle - \left\langle \gamma_{\times,i} \, \epsilon'_{\times,j} \right\rangle, \tag{5.23}$$

$$2 \, C^{\epsilon,GI}_{S,ij}(\theta) = \left\langle \gamma_{s,i} \, \epsilon'_{s,j} \right\rangle, \tag{5.24}$$

$$2 \, C^{\epsilon,GI}_{C,ij}(\theta) = \left\langle \gamma_{s,i} \, \epsilon'_{+,j} \right\rangle, \tag{5.25}$$

and finally the angular GI-spectra are

$$C^{\epsilon,GI}_{E,ij}(\ell) = \pi \int \theta \mathrm{d}\theta \ \left(C^{\epsilon,GI}_{+,ij}(\theta) \, J_0(\ell\theta) + C^{\epsilon,II}_{-,ij}(\theta) J_4(\ell\theta) \right), \tag{5.26}$$

$$C^{\epsilon,GI}_{B,ij}(\ell) = \pi \int \theta \mathrm{d}\theta \ \left(C^{\epsilon,GI}_{+,ij}(\theta) \, J_0(\ell\theta) - C^{\epsilon,II}_{-,ij}(\theta) J_4(\ell\theta) \right), \tag{5.27}$$

$$C^{\epsilon,GI}_{S,ij}(\ell) = 2\pi \int \theta \mathrm{d}\theta \ C^{\epsilon,GI}_{S,ij}(\theta) \, J_2(\ell\theta), \tag{5.28}$$

$$C^{\epsilon,GI}_{C,ij}(\ell) = 2\pi \int \theta \mathrm{d}\theta \ C^{\epsilon,GI}_{C,ij}(\theta) \, J_0(\ell\theta). \tag{5.29}$$

The derived spectra are not all statistically independent; the C– and S–modes use the same information as the E– and B–modes, but their knowledge enables consistency checks, which is why I will calculate them along the E– and B–mode spectra.

The presence of B-modes from GI–alignment can be explained by its inherent asymmetry: 'G' has to come before 'I', therefore this effect is not parity invariant at all. The II–alignment is completely symmetrical, which is why I would not expect there to be B–modes present.

Note that the contributions from the GI–correlations are for the most part negative because of the negative sign of the ϵ_+-component with regard to γ_+. Something like a second-order IG–alignment could be argued to be the lensing of already aligned galaxies (Giahi-Saravani & Schaefer, 2014). This will not be discussed in this work.

The alignment parameter D will be discussed more in detail in section 5.3. I determined a numerical value of $D = 9.5 \times 10^5$ in the units used in this work from the alignment signal found in Heymans et al. (2013), cf. Fig. (5.1). The value of the parameter depends on the choice of units because, unlike A, the alignment of ellipticals in this model depends on the absolute value of the gravitational field.

The power spectrum used in calculating the alignment of elliptical galaxies (both GI and II) will the non–linear one, as the alignment probes tidal fields in the evolved gravitational fields, just like weak lensing. However, the power spectrum will be smoothed on the mass scale $m_{\rm ell}$ of elliptical galaxies, i.e. on a spatial scale determined by $m_{\rm ell} = 4\pi/3\, R^3 \Omega_{\rm m} \rho_{\rm crit}$ (Crittenden et al., 2001; Schaefer & Merkel, 2015). I choose a value of $m_{\rm ell} = 10^{13} M_\odot/h$ for this scale, a typical halo mass for a field elliptical. The smoothing will be a Gaussian with the scale R,

$$P_\Phi(k) \to P_\Phi(k) \exp\left(-(kR)^2\right), \tag{5.30}$$

which is equivalent with the smoothing discussed in Kiessling et al. (2015b).

The correlation functions (equations 5.22 and 5.23) are shown in Fig. (5.5), the resulting E– and B–mode spectra in Fig. (5.6), together with the lensing signal (lensing E–mode for the IA B–mode spectra for comparability). Figures 5.7, 5.8, 5.9, and 5.10 show the E–, B–, S–, and C–mode spectra in a matrix-like arrangement for five tomographic bins.

5.2 Tidal Torque: From Correlation Functions to Angular Spectra

The tidal torque correlation functions and spectra work very similarly, and for the most part the principles can be seen in the previous section, although the results presented here (Schaefer & Merkel, 2015) came chronologically before the ones for the tidal shear (Tugendhat & Schaefer, 2018).

Since the tidal torque model is dependent on the square of the tidal shear, the correlations will end up being four-point correlators (Crittenden et al., 2001), but can be expressed with help of the Wick-theorem (which also implicitly needs Gaussianity) as

$$\left\langle \hat{\Phi}_A(\boldsymbol{x}) \hat{\Phi}_B(\boldsymbol{x})\, \hat{\Phi}_C(\boldsymbol{x}') \hat{\Phi}'_D(\boldsymbol{x}') \right\rangle = \frac{1}{(14\zeta_2(0))^2} \left(\tilde{C}_{AC} \tilde{C}_{BD} + \tilde{C}_{AD} \tilde{C}_{BC} \right), \tag{5.31}$$

where the letters indicate pairs of indices. Now the four non-zero correlation functions of the ellipticities as defined in section 4.2, one arrives at the non-zero correlations (Schaefer & Merkel, 2015):

$$\langle \epsilon_+ \epsilon'_+ \rangle = \frac{1}{144} \left(\frac{A\alpha}{14\zeta_2} \right)^2 (A_{++} \cos(4\alpha) + B_{++} \cos(2\alpha) + C_{++}), \tag{5.32}$$

$$\langle \epsilon_\times \epsilon'_\times \rangle = \frac{1}{18} \left(\frac{A\alpha}{14\zeta_2} \right)^2 (B_{\times\times} \cos(2\alpha) + C_{\times\times}), \tag{5.33}$$

$$\langle \epsilon_+ \epsilon'_s \rangle = \frac{1}{324} \left(\frac{A\alpha}{14\zeta_2} \right)^2 (A_{+s} \cos(4\alpha) + B_{+s} \cos(2\alpha) + C_{+s}), \tag{5.34}$$

$$\langle \epsilon_s \epsilon'_s \rangle = \frac{1}{108} \left(\frac{A\alpha}{14\zeta_2} \right)^2 (A_{ss} \cos(4\alpha) + B_{ss} \cos(2\alpha) + C_{ss}). \tag{5.35}$$

For a more detailed overview and the full A, B, and C coefficients, consider section B.2 in the appendix.

For the alignment parameter in this model, I choose a value of $A = 0.25$ which is found in numerical simulation of tidal torquing (Crittenden et al., 2001) and has been used in previous work (Schaefer & Merkel, 2015). This parameter does not need special treatment of its units, as it doesn't measure the gravitational field strength. Rather, it quantifies how much the angular momentum of the host halo is connected with the ellipticity of the spiral galaxy in it. Another factors going into this conservative choice is the fact that galactic discs are not uniformly bright, therefore their measured ellipticity can scatter intrinsically, depending on the measurement method used.

The power spectrum used for the calculation the alignment of spiral galaxies in this work is linear. This is because the angular momentum generation happens in cosmic times when linearity is still given, i.e. only the initial conditions play a role in determining the spectra. Assuming linearity, and therefore Gaussianity, is the reason for vanishing GI–alignment for spirals, as opposed to Blazek et al. (2017). In that work, however, spirals also react to the strength of the gravitational fields.

The linear power spectrum will further be smoothed on the mass scale m_{spir} of spiral galaxies, just like in the previous section for ellipticals. I choose a value of $m_{\mathrm{ell}} = 10^{12} M_\odot/h$ for this scale, about the halo mass for a Milky Way-sized galaxy. The smoothing will be a Gaussian, just like in the previous section.

The correlation functions (equations 5.22 and 5.23) are shown in Fig. (5.4), the resulting E– and B–mode spectra in Fig. (5.6). Figures 5.7, 5.8, 5.9, and 5.10 show the E–, B–, S–, and C–mode spectra in a matrix-like arrangement for five tomographic bins.

5.3 Determining D

Here, I show a way of determining D by using the signal to noise-ratio Σ that has been measured for the intrinsic alignment amplitude for elliptical ("early-type") galaxies by Heymans et al. (2013). The ratio Σ can also be defined by

$$\Sigma = \frac{\mu}{\sigma}, \tag{5.36}$$

for a Gaussian distribution. Considering Fig. (5.1), Heymans et al. (2013) measure the amplitude with $\Sigma \approx 2$. Of course, their likelihoods aren't Gaussian, but they are symmetrical enough that equation (5.36) can be

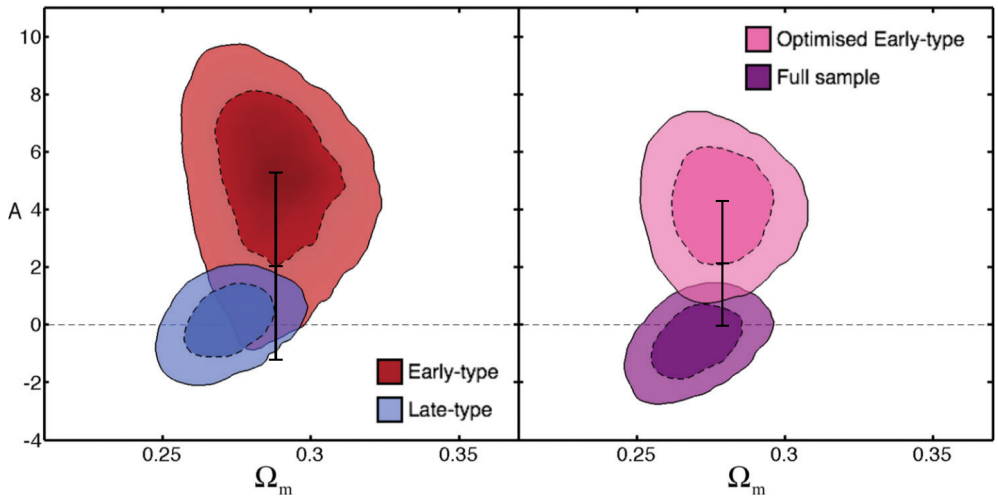

Figure 5.1: Figure 11 of Heymans et al. (2013). They detect an alignment signal of "early type" galaxies, i.e. ellipticals in this work, with $\lesssim 2\sigma$. This was used as a gauge for determining the proportionality constant D. Black guides in the figure added are for clarification.

applied to estimate the signal to noise-ratio. This can also be calculated for elliptical galaxies within my model assumptions as

$$\Sigma^2 = f_{\rm sky} \sum_\ell \frac{2\ell+1}{2} {\rm tr}\left[C^{{\rm tot},-1} C^\epsilon\, C^{{\rm tot},-1} C^\epsilon\right], \tag{5.37}$$

where $C^\epsilon_{ij} = C^{\epsilon,II}_{E,i} + C^{\epsilon,GI}_{E,ij}$ is the total IA covariance and $C^\gamma_{ij} = C^{\rm tot}_{ij} + C^\epsilon_{ij} + \sigma^2_\epsilon n_{\rm bin}/\bar{n}$ is the total ellipticity measured, consisting of weak lensing, intrinsic alignments, and shape noise. The survey parameters for CFHTLenS are found in table (3.1) and for the work cited above, six tomographic bins were used with a field of view of 1.5 arcmin $\leq \theta \leq$ 35 arcmin, which corresponds to angular scales of between $\ell_{\rm min} \approx 310$ and $\ell_{\rm max} \approx 720$.

Their alignment signal for spirals is consistent with zero ($\Sigma < 1$), which is reproduced by $A = 0.25$, thereby at least reenforcing that parameter choice.

So basically what was done is a sweep of $D - \Sigma$ space by different choices of D. The final iterations of this can be seen in Fig. (5.2). Overall, the slope is very shallow, allowing for values up to 30–50 per cent higher or lower still being consistent with the findings by CFHTLenS. The outer values reveal that the relation between D and Σ is not linear. In fact, I expect it to be $\Sigma \propto D^{1\ldots1.5}$, since the GI signal provides a D for the amplitude, whereas the II signal is proportional to D^2. However, the number of bins with GI–amplitudes outnumbers those with an II–amplitude by

$$\frac{n_{GI\text{-bins}}}{n_{II\text{-bins}}} = \frac{n_{\rm bin}+1}{2}. \tag{5.38}$$

There's also a slight dependence on the smoothing scale employed for ellipticals and other factors, such as the spiral fraction q. The dependence on σ_8 is almost none, since both elliptical alignment and weak lensing scale equally strong with it. This would be different with spirals.

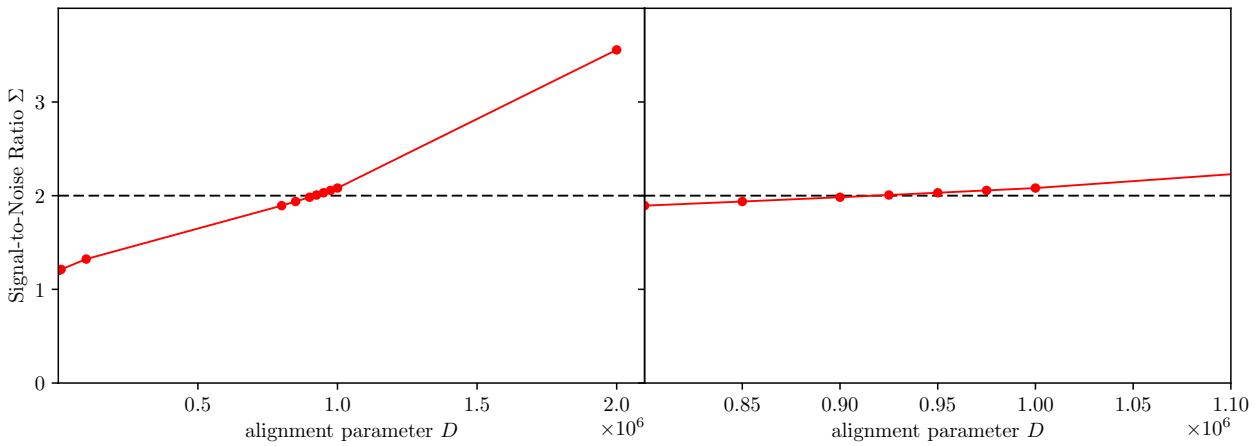

Figure 5.2: Sweep of $D - \Sigma$ in the vicinity of $\Sigma \approx 1 \ldots 2$, with a later reiteration at $\Sigma \approx 2$. The relation is not quite linear, as can be seen in the left panel.

This result can be compared to other measurements of the amplitude of linear alignments, such as Hilbert et al. (2016) from the Illustris[1] simulation. The amplitude is called χ_τ in that work, referring to Joachimi et al. (2011). That amplitude parameter is defined as

$$\chi_\tau = \frac{AC_1\rho_{\mathrm{crit}}\Omega_{\mathrm{m}}}{D(z)}, \tag{5.39}$$

where $C_1\rho_{\mathrm{crit}} = 0.0134$ and D is the usual linear growth function. In their work Hilbert et al. (2016) present a result of $A = 0.03$ for matter density/intrinsic ellipticity correlations, but suppose that can go up to $A = 0.9$ for larger scales. With $\Omega_{\mathrm{m}} = 0.2726$, such that $\chi_\tau \approx 1.096 \times 10^{-4}/D(z) \ldots 33 \times 10^{-4}/D(z)$. Going back to the definition of C_I (Hirata & Seljak, 2004), the difference between the choice in this work, D, is a factor of $4\pi G$. Therefore, this works out to

$$\frac{D}{\chi_\tau} = \frac{4\pi G D}{1.1 \times 10^{-4} \ldots 33 \times 10^{-4}/D(z)} = 7.3 \ldots 0.24 D(z), \tag{5.40}$$

which is fairly consistent considering that D doesn't lead to inconsistent Σ within 50 per cent of its chosen value. Since these are two completely different ways of determining the alignment parameter, they show a good agreement. Note that the value for D was obtained with a unit-free potential that's measured in the velocity dispersion σ^2, so that D should be written $D = 9.5 \times 10^5 c^2$. But as this is implicitly true for χ_τ as well, those factors will cancel. As argued before, in this work I assume that D is constant with redshift and scale.

5.4 Ellipticity Correlation Functions of the Intrinsic Alignment Models

In this section, I show correlation functions and spectra for intrinsic alignment as well as weak lensing spectra for three and five tomographic bins. All of them have been calculated with the `libtomo` C library[2], which I developed out of the existing `tomo`–code by Björn Malte Schäfer. Almost all of the calculations were done on the BwUniCluster in Karlsruhe.

The detectability of intrinsic alignment correlations by Euclid is outstanding, in both the positive and negative sense of the word. Fig. (5.3) shows that the mix of both signals, especially, has something like $\Sigma \approx 200$ for

[1] `http://www.illustris-project.org/`
[2] available at `https://gitlab.com/tugi/tomo-ia`

$\ell \geq 1000$. Clearly, the ellipticals make out the brunt of this due to their GI–signal, even though they make out less than half of the galaxies in the sample.

Fig. (5.5) shows the correlation functions for the tidal shearing model. Note that the weak lensing–alignment cross–correlation is in fact negative, but can occasionally lead to a positive GI-spectrum (cf. Fig. (5.6)), this is due to the negative sign in the Fourier–transform. By about an order of magnitude larger than the ellipticals' correlation functions are the ones for the spirals, Fig. (5.4), but their overall shape is extremely similar. Note that the much larger cutoff scale for the ellipticals, at about 200 arcmin, whereas the spirals' correlation is already negligible at 30 arcmin. This will lead to differences in the spectra as well: Spiral alignment is much more prominent at high ℓ, whereas ellipticals come at lower ℓ, but experience a cutoff due to the smoothing scale (cf. equation (5.30)). The GI spectra don't experience this cutoff on either side of the scales since their interaction can have a much longer reach due to the interaction with lensing and even at small angles they're not cut off since the background galaxies will have a considerable distance in three dimensions. However their contributions to the overall IA signal is lowest at intermediate ℓ, possibly due to dwindling lensing efficiency.

Another way of plotting the spectra is in a plot–array, as in Fig. (5.7), which shows the contributions of each bin–cross–correlation as they would appear in a matrix. This helps understanding the impact of GI correlations: while on the diagonal, the shape noise (orange) and the three intrinsic alignment are present alongside the ordinary lensing signal, the off-diagonals show that the GI correlations can contaminate bin cross–correlations as well. In fact, the GI signal on the off-diagonals is stronger as a general rule, because the lensing efficiency function suppresses lenses that are too close to the aligned structures.

In the same matrix form are the B–modes (Fig. (5.8)), S–modes (Fig. (5.9)), and C–modes (Fig. (5.10)). The B–modes show what was expected: No B–modes for ellipticals, except for the GI–part, which is asymmetrical by its nature. The spirals generate B-modes because of their quadratic dependency on $\Phi_{\alpha\beta}$.

The S– and C–mode spectra are consistent with the previous results, however it is noteworthy that the GI–alignments peak at intermediate ℓ and then decrease. This is likely due to the fact that for both these spectra ϵ_s is needed, and at large ℓ, the modulus of the ellipticity due to a combined lensing–alignment effect is likely much lower than at low or intermediate angular separation.

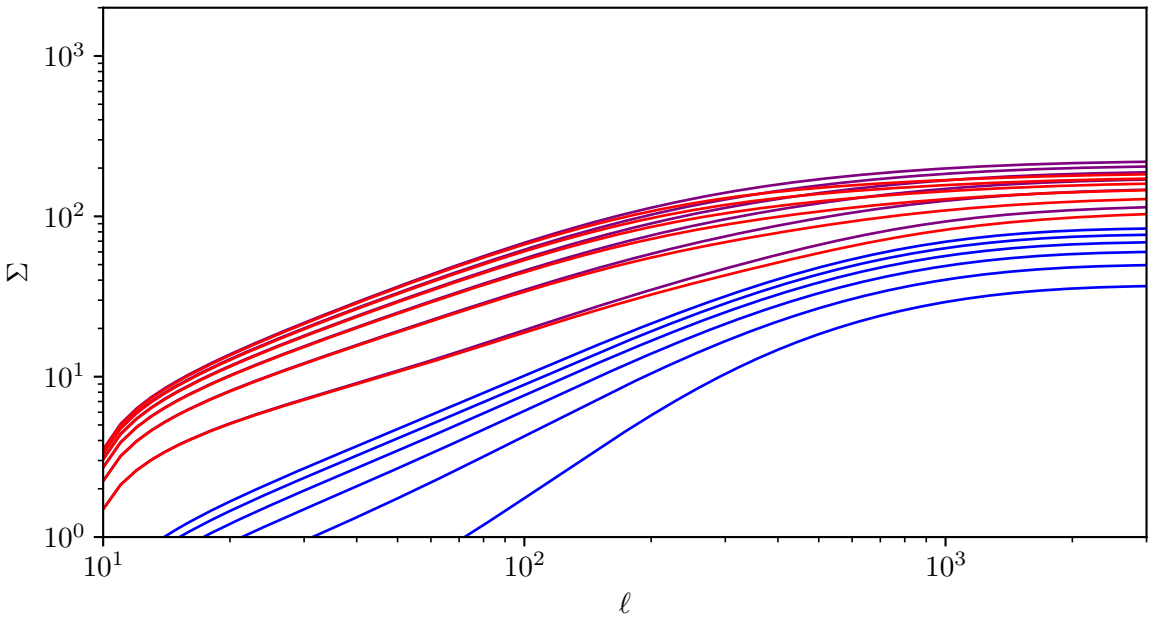

Figure 5.3: Signal to noise-ratio Σ for the IA signal from elliptical galaxies (red), spiral galaxies (blue) and a mix of both (purple) for 2 . . . 7 tomographic bins.

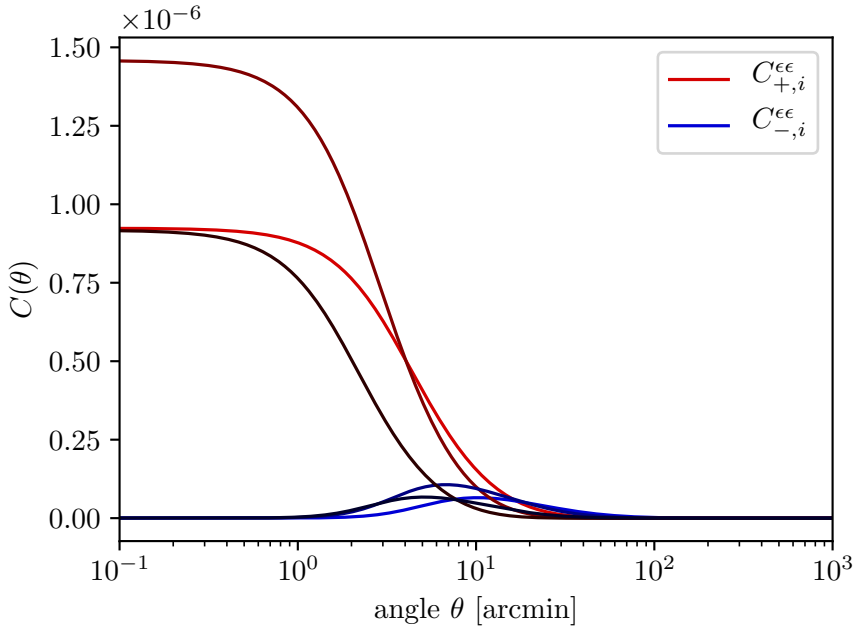

Figure 5.4: Correlation functions C_+ (red) and C_- (blue) for spirals, i.e. the tidal torquing model. II–alignment only. Three tomographic bins mean that there are three spectra for the II–alignment signal.

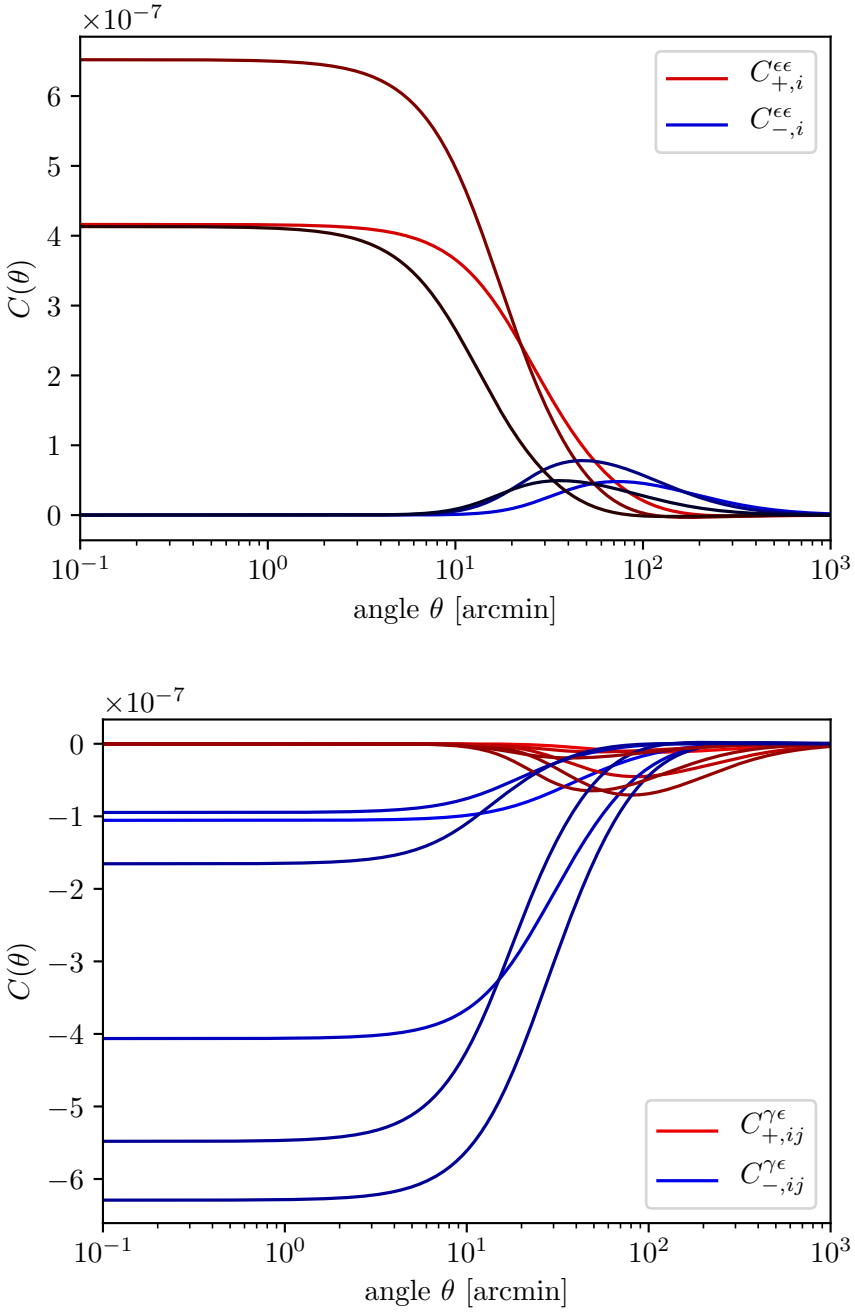

Figure 5.5: Correlation functions C_+ (red) and C_- (blue) for ellipticals, i.e. the tidal shearing model. Left panel: II–alignment, right panel: GI–alignment. Three tomographic bins mean that there are three spectra for the II–alignment signal and $3(3+1)/2 = 6$ for the GI–alignment, where off–diagonals don't vanish. Note that the correlation functions are negative for GI–alignment.

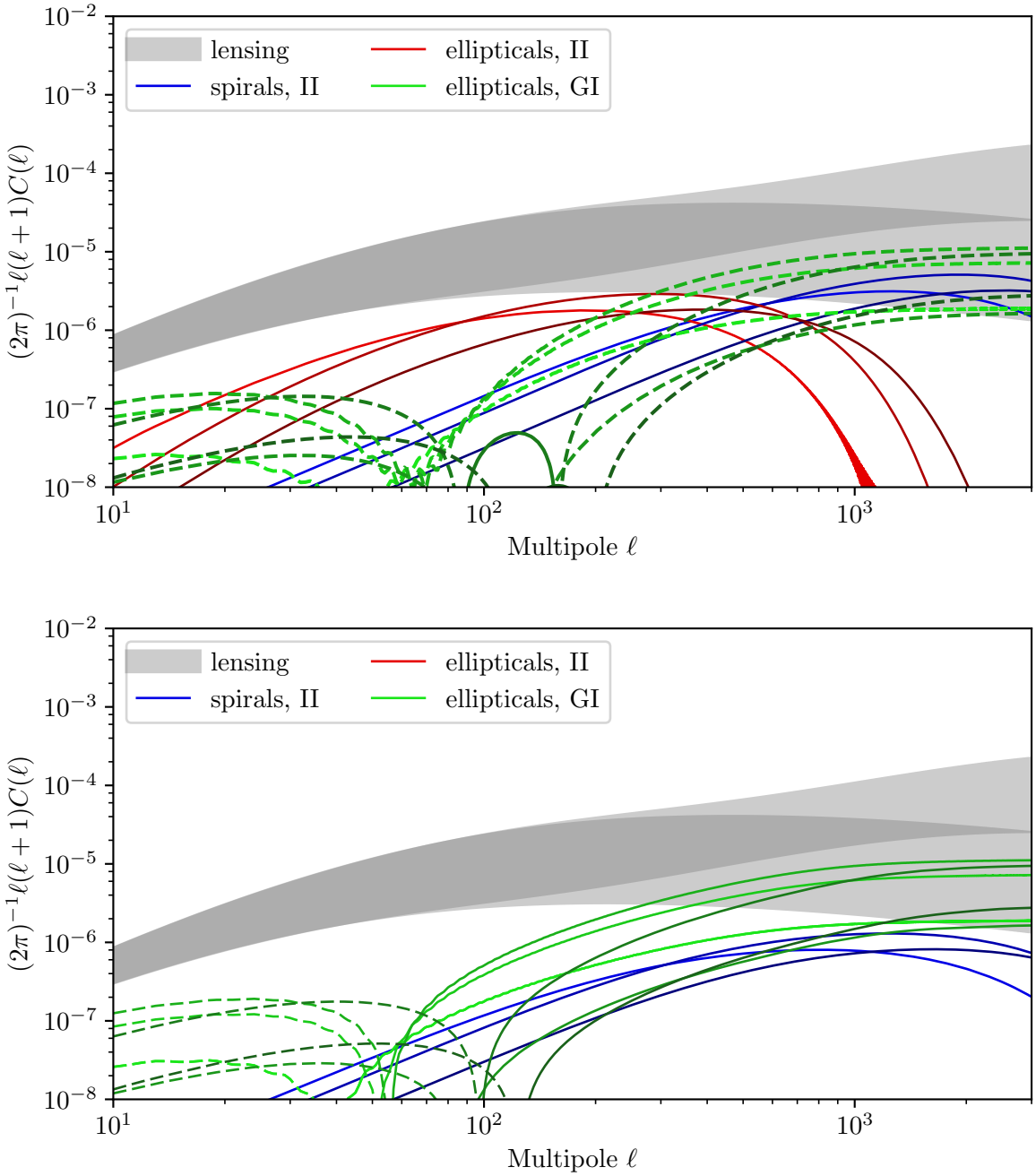

Figure 5.6: Resulting IA and lensing spectra for three tomographic bins. Upper panel: *E*–modes, lower panel: *B*–modes. The grey shaded area represents the lensing *E*–mode in both panels, with the upper fork using the non-linear power spectrum and the lower fork using the linear one. Red: ellipticals II, green: ellipticals GI, blue: spirals II. Negative values are represented by dashed lines.

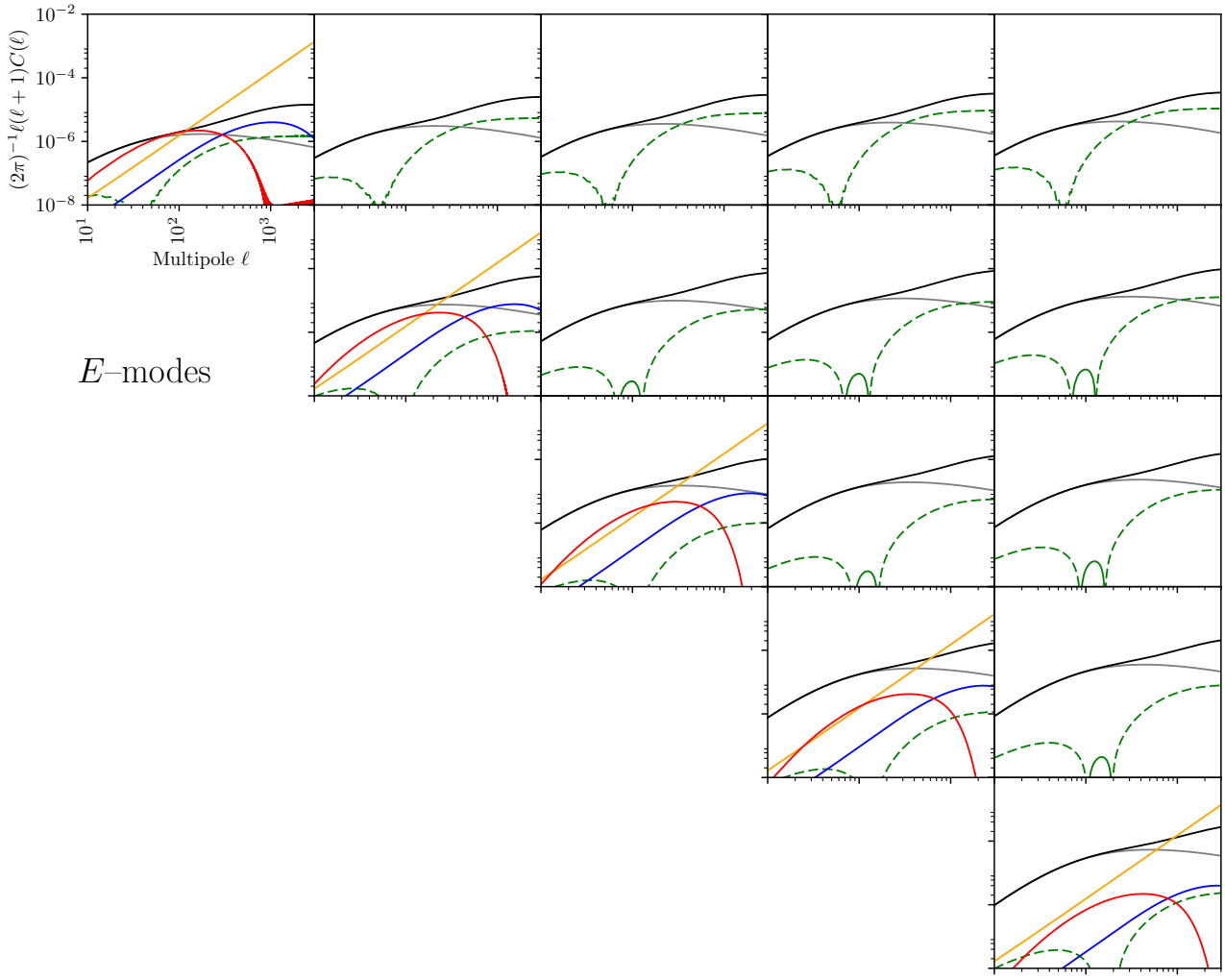

Figure 5.7: E-mode spectra $C^{\gamma}_{E,ij}(\ell)$, $C^{\epsilon,GI}_{E,ij}(\ell)$ and $C^{\epsilon,II}_{E,ij}(\ell)$ for five tomographic bins: the bin correlations are ordered the same way a matrix would be from top left $C_{E,11}$ to bottom right $C_{E,55}$. Black curves show the weak lensing signal from a nonlinear power spectrum and its grey fork shows the same for a linear power spectrum. Ellipticity spectra are blue for spirals, red for ellipticals (both II), and green for ellipticals' GI spectra. Solid lines indicate positive value, whilst dashed lines show negative values. The orange lines show the ellipticity shape noise $\sigma^2_\epsilon n_{\rm bin}/\bar{n}$ for five tomographic bins.

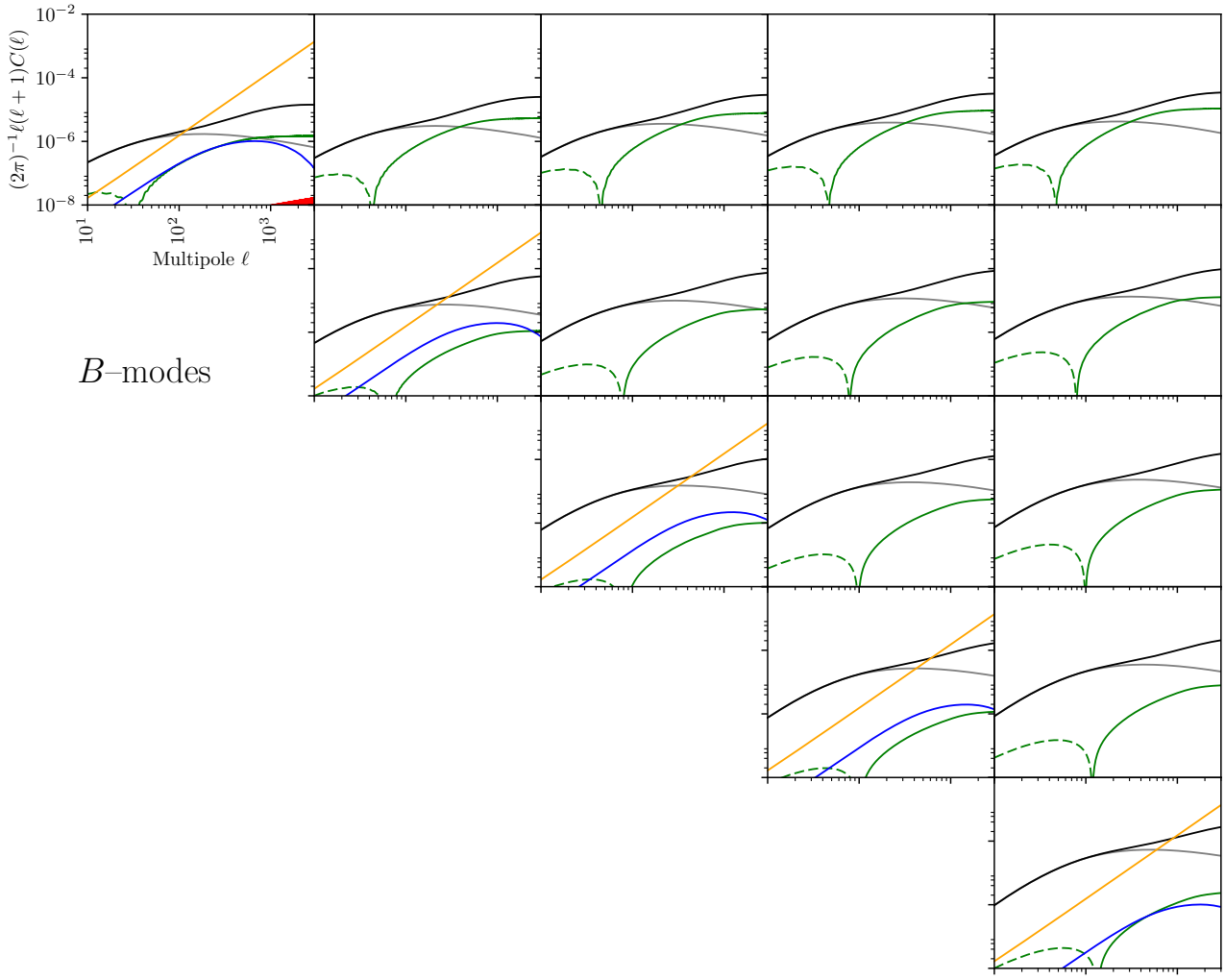

Figure 5.8: B-mode spectra $C^{\epsilon,GI}_{B,ij}(\ell)$ and $C^{\epsilon,II}_{B,ij}(\ell)$ for five tomographic bins: the bin correlations are ordered the same way a matrix would be from top left $C_{B,11}$ to bottom right $C_{B,55}$. Black curves show the weak lensing E-mode signal $C^{\gamma}_{E,ij}(\ell)$ from a nonlinear power spectrum and its grey fork shows the same for a linear power spectrum for comparison. Ellipticity spectra are blue for spirals, red for ellipticals (both II), and green for ellipticals' GI spectra. Solid lines indicate positive value, whilst dashed lines show negative values. The orange lines show the ellipticity shape noise $\sigma^2_\epsilon n_{\rm bin}/\bar{n}$ for five tomographic bins.

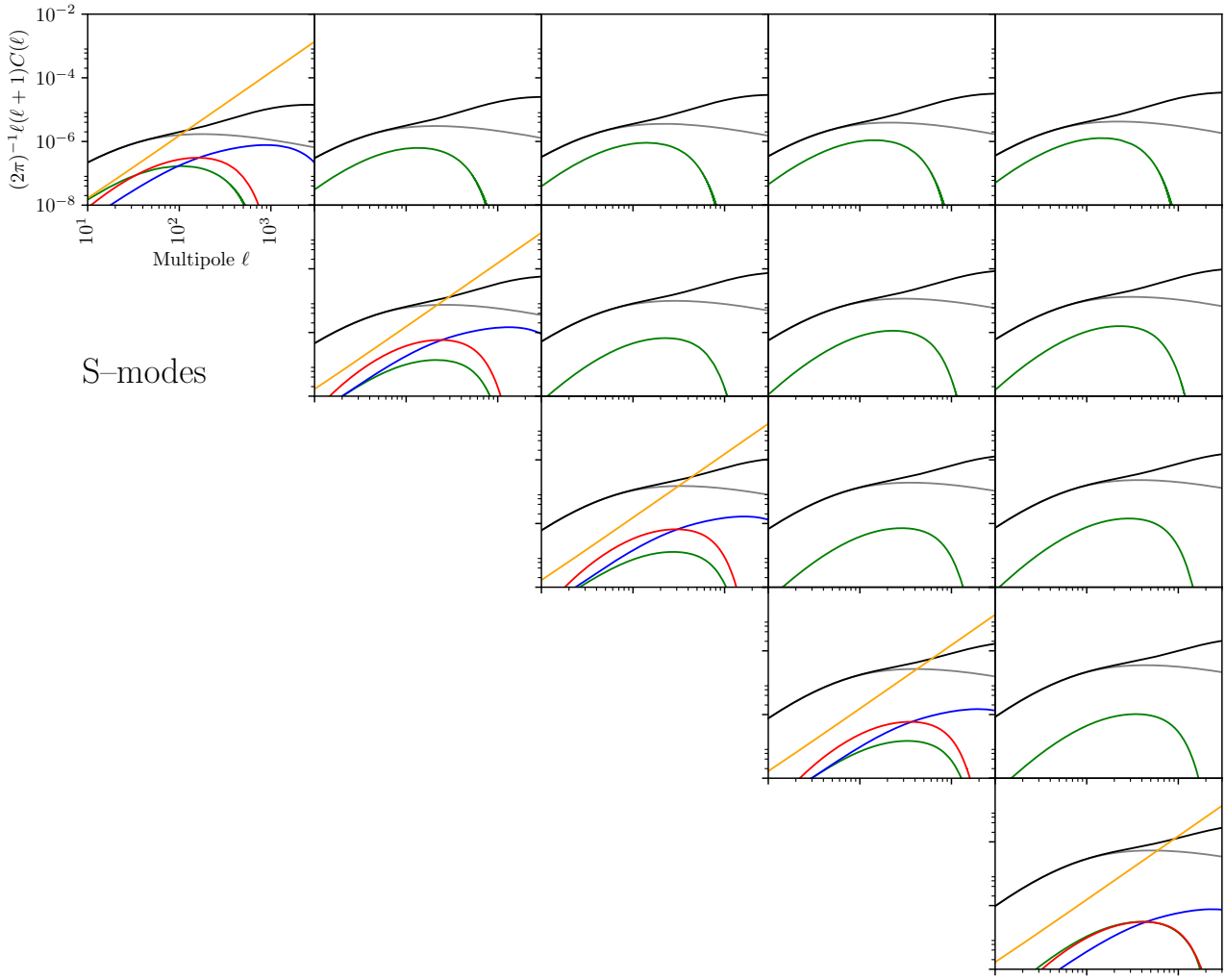

Figure 5.9: S-mode spectra $C^{\epsilon,GI}_{\mathrm{S},ij}(\ell)$ and $C^{\epsilon,II}_{\mathrm{S},ij}(\ell)$ for five tomographic bins: the bin correlations are ordered the same way a matrix would be from top left $C_{\mathrm{S},11}$ to bottom right $C_{\mathrm{S},55}$. Black curves show the weak lensing E-mode signal $C^{\gamma}_{E,ij}(\ell)$ from a nonlinear power spectrum and its grey fork shows the same for a linear power spectrum for comparison. Ellipticity spectra are blue for spirals, red for ellipticals (both II), and green for ellipticals' GI spectra. The orange lines show the ellipticity shape noise $\sigma^2_\epsilon n_{\mathrm{bin}}/\bar{n}$ for five tomographic bins.

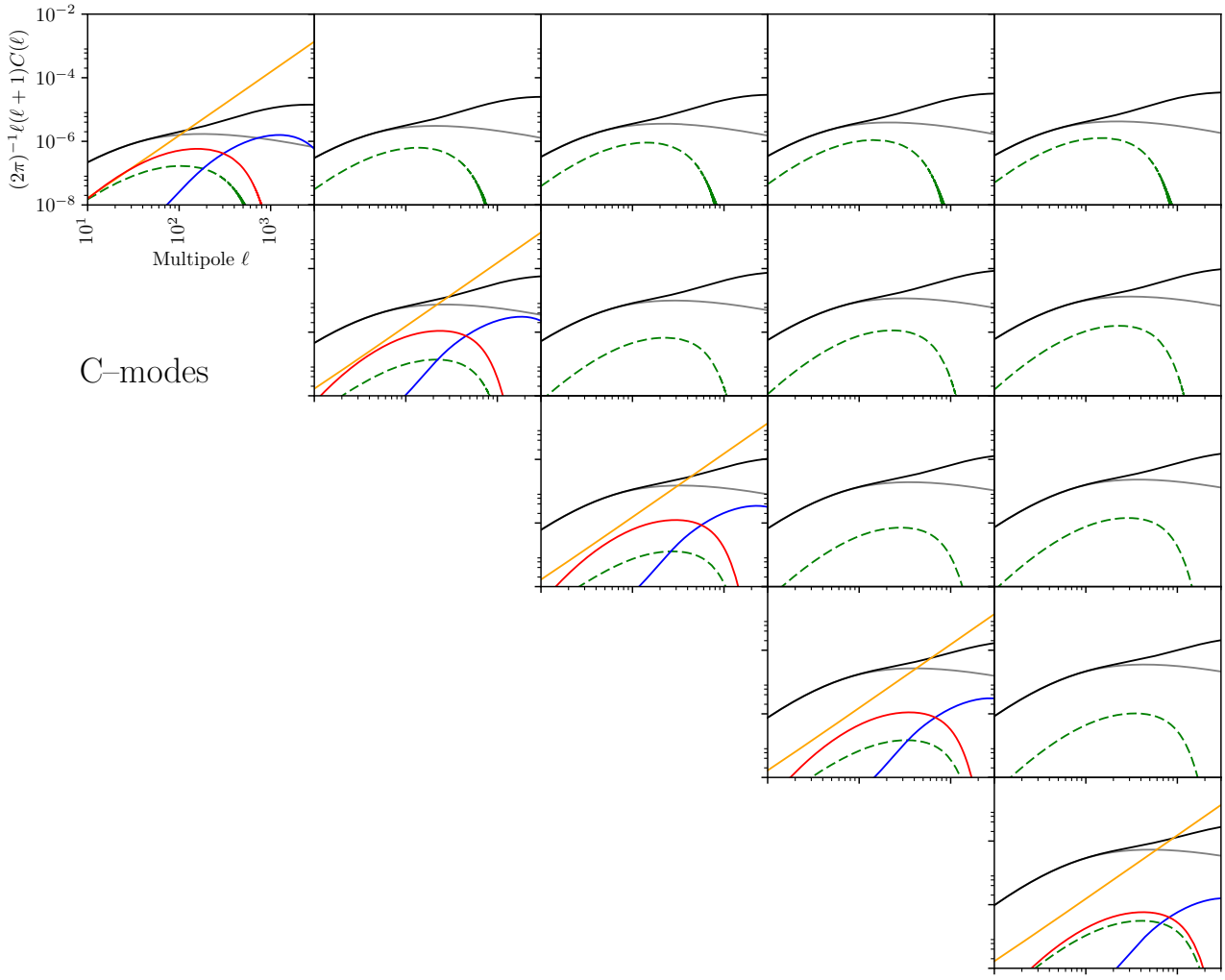

Figure 5.10: C-mode spectra $C^{\epsilon,GI}_{\mathrm{C},ij}(\ell)$ and $C^{\epsilon,II}_{\mathrm{C},ij}(\ell)$ for five tomographic bins: the bin correlations are ordered the same way a matrix would be from top left $C_{\mathrm{C},11}$ to bottom right $C_{\mathrm{C},55}$. Black curves show the weak lensing E-mode signal $C^{\gamma}_{E,ij}(\ell)$ from a nonlinear power spectrum and its grey fork shows the same for a linear power spectrum for comparison. Ellipticity spectra are blue for spirals, red for ellipticals (both II), and green for ellipticals' GI spectra. The orange lines show the ellipticity shape noise $\sigma^2_\epsilon n_{\mathrm{bin}}/\bar{n}$ for five tomographic bins.

6 Effects of Intrinsic Alignments on Tomographic Weak Lensing Measurements

In this chapter, I will present the effects of the composite model as well as each individual model on parameter inference. The bias induced by fitting the ellipticity spectra with the wrong (weak lensing–only) one is compared with the true best fit value. The basis for this has been laid in section 3.5. Firstly, I will show the bias for seven tomographic bins and discuss the implications. The second part will be about quantifying the bias using the figure of bias, which can be converted to the Kullback-Leibler divergence. Furthermore, the inferred parameter set will be put into the context of a prior with the Bayesian evidence $2\ln(k)$, which is quantifies the offset the parameter set has compared to an unbiased one from CMB observations.

As described in section 3.5, we're now considering how to infer a set of wCDM parameters from an observed spectrum, although the w is constant in time, such that $w = -1$ would be referred to as standard ΛCDM.

6.1 Parameter Estimation Biases

Depending on which model was used to describe the intrinsic alignments, the true and false covariance matrices are described by

$$C_{t,ij}(\ell) = C^{\epsilon,\mathrm{IA}}_{E,ij}(\ell) + C^{\gamma}_{E,ij}(\ell), \tag{6.1}$$

$$C_{f,ij}(\ell) = C^{\gamma}_{E,ij}(\ell), \tag{6.2}$$

where $C^{\epsilon,\mathrm{IA}}_{E,ij}(\ell)$ is the total intrinsic alignment amplitude of the chosen model (elliptical, spiral, or both together); summation over the indices i,j not implied. The bias δ_μ is obtained by solving equation (3.46) with the given covariance matrices and derivatives. If the intrinsic alignment amplitude $C^{\epsilon,\mathrm{IA}}_{E,ij}(\ell)$, the bias reduces to $\delta_\mu = 0$ because the date was fitted with the correct model and no systematic error is induced. The logarithmic derivatives of the respective spectra is shown in Fig. (6.1) for three tomographic bins. It is noticeable that the elliptical–model curves are almost always covered by the curves from the mixed model. This is due to the fact that those two are taken from the nonlinear power spectrum whereas the spirals' curves assume the linear power spectrum. However, there are indeed differences between all three biases: Fig. (6.2) shows the thus computed biases for all three cases. The underlying error ellipses are Fisher ellipses taken of the spectrum without any intrinsic alignment pollution. Schaefer & Reischke (2016) show that for small deviations from the fiducial values, the fisher matrices can be approximated by an infinitesimal linear transformation; for our purposes I will leave them as-is, as small changes in the ellipses won't change the overall outcome. So to read Fig. (6.2) correctly: In case of e.g. the spiral model applying, the error ellipse at the fiducial values would be shifted to the blue points, sometimes lying entirely outside its original location with no overlap in 1σ or 2σ even. This would mean that the systematic error is larger than the e.g. 2σ region of the statistical one, sometimes even outside the 3σ region. There have been reports (Joudaki et al., 2016) of slight tension between the Ω_m and

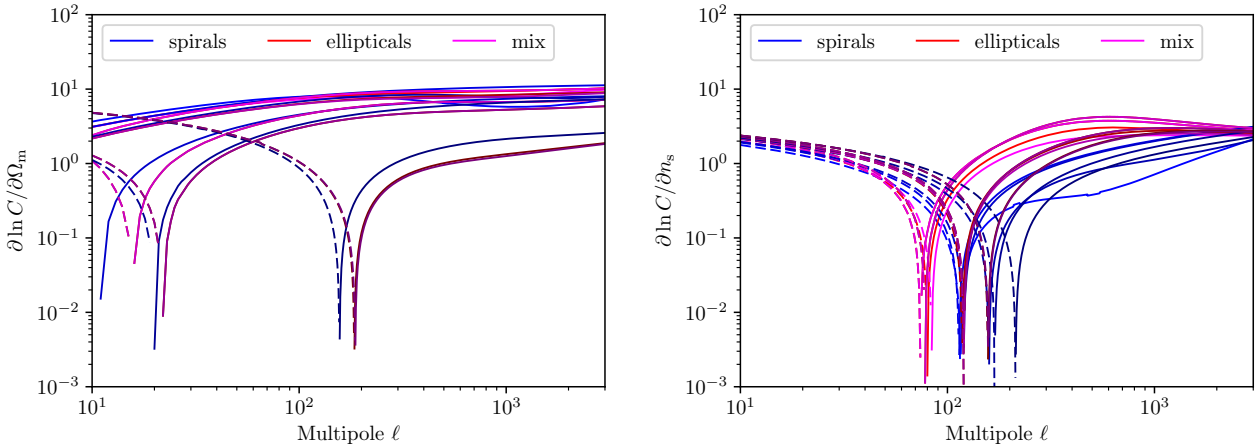

Figure 6.1: Logarithmic derivatives of the ellipticity spectra for three tomographic bins using just one or both models. All three sets of spectra have the weak lensing spectrum $C^{\gamma}_{E,ij}$ as their base; they only differ in which IA model is added on top.

σ_8 inferences of weak lensing surveys, KiDS[1], and CMB measurements. In particular the elliptical and mixed models would systematically underestimate both parameters.

Note that the naïve assumption that 'purple = red + blue' is false. The bias due to elliptical galaxies the one due to spiral galaxies will not, in general, additively give the same results for the bias of the mixed model. This is because the derivatives of the three different (true) spectra

$$C^{\mathrm{red}}_{t,ij}(\ell) = C^{\epsilon,\mathrm{II,e}}_{E,ij}(\ell)\delta_{ij} + C^{\epsilon,\mathrm{GI}}_{E,ij}(\ell) + C^{\gamma}_{E,ij}(\ell), \tag{6.3}$$

$$C^{\mathrm{blue}}_{t,ij}(\ell) = C^{\epsilon,\mathrm{II,s}}_{E,ij}(\ell)\delta_{ij} + C^{\gamma}_{E,ij}(\ell), \tag{6.4}$$

$$C^{\mathrm{purple}}_{t,ij}(\ell) = C^{\epsilon,\mathrm{II,s}}_{E,ij}(\ell)\delta_{ij} + C^{\epsilon,\mathrm{II,e}}_{E,ij}(\ell)\delta_{ij} + C^{\epsilon,\mathrm{GI}}_{E,ij}(\ell) + C^{\gamma}_{E,ij}(\ell), \tag{6.5}$$

are, in general, not additive (see Fig. (6.1)). Such properties make it hard to predict the mixed model from from the individual behaviour of each model.

The additivity of the two models is also affected by the spiral fraction q, which appears as $\propto q^2$ in the II–spectra and as $1 - q$ in the GI–spectra, which makes addition even less linear. An additionally wildly changing q over cosmic time or galaxy environment would make the mixed model almost stochastic, which is also why q was set to a constant in this work, although it can be easily implemented to be a function of almost any parameter, but this would make the three model cases less comparable, which is part of the aim of this work. Further reasons were given in section 4.1.

Some parameters, like the dark energy equation of state, are not affected greatly and the systematics fall within the statistical errors, which makes it hard to believe that intrinsic alignments would favour a dynamical dark energy model $w(a)$ instead of a ΛCDM model. The biases for h are quite highly significant, which might add some talking points to the inferred H_0 from weak lensing surveys, as there is still tension between Planck and other measurements of H_0. The scalar spectral index n_s is significantly over–estimated, which might have to do with the model trying to explain an excess of power by a steeper power spectrum – this is especially true for models with varying power on top of the lensing power spectrum, which the mixed model provides clearly with the spirals coming in late and the ellipticals (II) peaking in the intermediate range, while the GI– part of the

[1] `http://kids.strw.leidenuniv.nl`

ellipticals becomes important at small scales. A correlation between n_s, A, and D is likely highly degenerate. Fig. (6.3) shows the individual error for each parameter normalised by its marginalised statistical standard deviation $\sigma = \sqrt{(F^{-1})_{\mu\mu}}$, so it is easier to see which parameters lie well inside or outside their statistical error bars. The evolution with increasing number of bins is also interesting, as the bias changes as the error ellipse shrinks. In some cases, like with w, this does not change the situation much, whereas in the case of σ_8 the increasing number of bins cause a greater systematic error. Here, we can see again that the spiral model is designed not to be sensitive to the strength of the gravitational field; it doesn't alter the inference of σ_8 much, whereas the elliptical and mixed models do. Therefore, the elliptical model – unlike the spiral one – itself can be used as a probe for the local gravitational field.

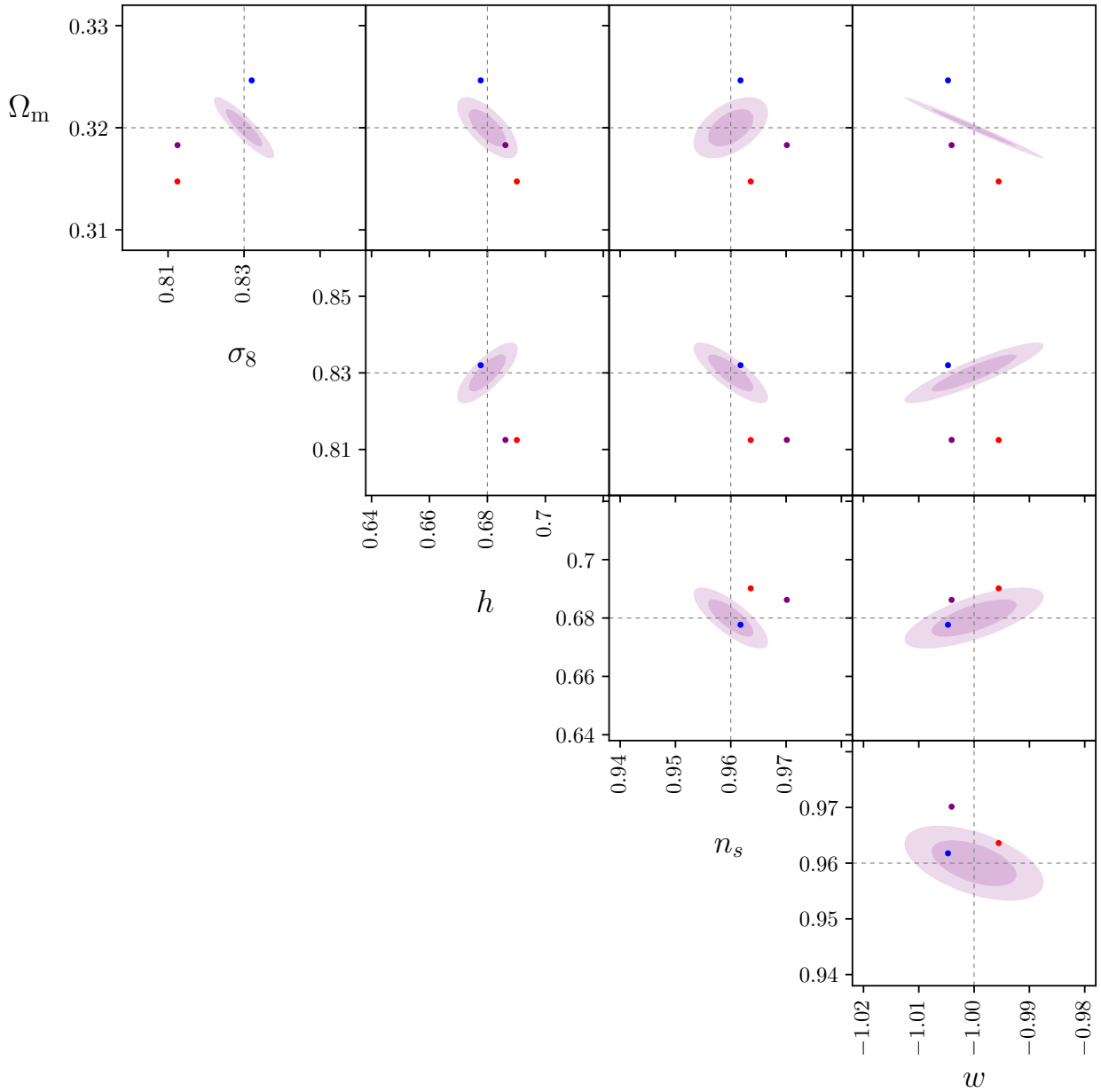

Figure 6.2: Parameter estimation biases for 7 tomographic bins in a Euclid–like survey together with marginalised error ellipses of 1σ and 2σ. The purple dots represent the new best–fit point when fitting the data to the false (lensing–only) covariance with a mixed model, the red dots do the same for a pure elliptical galaxy model and the blue ones for an all spiral–alignment model.

6.2 Figure of Bias and Bayesian Evidence

The figure of bias $Q^2 = \sum_{\mu,\nu} \delta_\mu F_{\mu\nu} \delta_\nu$ (Schaefer & Merkel, 2015; Tugendhat & Schaefer, 2018) is a measure of how much a given distribution $F_{\mu\nu}$ is affected by a bias δ_μ or the scale of the bias relative to the statistical error. The Kullback–Leibler–divergence (see section 3.5) is given as

$$D_{\mathrm{KL}} = \int \mathrm{d}^N\theta \, \mathcal{L}_t(\boldsymbol{\theta}) \ln\left(\frac{\mathcal{L}_t(\boldsymbol{\theta})}{\mathcal{L}_f(\boldsymbol{\theta})}\right), \tag{6.6}$$

with the two likelihoods for the true and the false model respectively. In case of Gaussian likelihoods, this reduces to

$$D_{\mathrm{KL}} = \frac{1}{2}\left(\mathrm{tr}\left[C_f^{-1} C_t\right] + \sum_{\mu\nu} \left(C_f^{-1}\right)_{\mu\nu} \delta_\mu \delta_\nu - n_{\mathrm{bin}} + \ln\left(\frac{\det C_f}{\det C_t}\right)\right). \tag{6.7}$$

Now, for small shifts δ_μ we can write $C_t \approx C_f$ (see Schaefer & Reischke (2016)), and as $C_t^{-1} = F$ and $\mathrm{tr}\left[C_t^{-1} C_t\right] = n_{\mathrm{bin}}$, this becomes

$$D_{\mathrm{KL}} = \frac{1}{2}\left(N + \sum_{\mu\nu} F_{\mu\nu}\delta_\mu\delta_\nu - N + \ln\ 1\right) = \frac{Q^2}{2}. \tag{6.8}$$

According to Fig. (6.4), surprisingly, the elliptical model alone is much worse than the mixed model. But this can already somewhat seen in Fig. (6.3), as the red elliptical model is regularly further from the fiducial parameter than the purple mixed one. Apparently, the influence of the spiral alignment is in fact a bit of a correction back towards less extreme biases. The overall figure of bias Q is quite constant with the bin number, which is encouraging, as more bins promise more information up until a certain point. I can reproduce the finding of Schaefer & Merkel (2015) that Q for the spiral model hovers around $Q = 20$.

A measure of the compatability of two models is the Bayesian evidence k, given by

$$k = \frac{\int \mathrm{d}^N\theta \, p(\theta_\mu)\, \mathcal{L}_t(\theta_\mu)}{\int \mathrm{d}^N\theta \, p(\theta_\mu)\, \mathcal{L}_f(\theta_\mu)}, \tag{6.9}$$

with the usual nomenclature of the true and false likelihoods. The distribution $p(\theta_\mu)$ is a prior; it can be a completely different measurement of the same parameters, as long as it has the same dimensionality (if it doesn't, it can still be marginalised to the correct parameter space). Intuitively, it is the ratio of the integrated probability overlap of the prior and the two rivalling posteriors. It therefore compares two models $\mathcal{L}_t$ and $\mathcal{L}_f$ with an existing, established one p. For a sample case, I took a Planck–like CMB prior und a BAO prior[2] to test the Bayesian evidence for those two cases and the biased weak lensing distribution. The situation is illustrated in Fig. (6.7) and Fig. (6.6). The numerical evaluation of the Bayesian evidence with respect to a CMB prior is shown in Fig. (6.5). Here, the mixed model is by far worse than the other two. This is due to the fact that for Bayesian evidence, not only the distance to the fiducial value plays a role, but also the direction of degeneracy of the different matrices, see Fig. (6.6). For the BAO–prior, the numerical evaluation didn't converge, as the shifted weak lensing likelihood was much too far away from the fiducial values in terms of the tiny BAO error ellipses. As values above $2\ln k = 10$ on the Jeffrey's scale (Kass & Raftery, 1995; Nesseris & Garcia-Bellido, 2013) is considered a 'very strong incompatibility', the false lensing likelihoods would support the (wrong) conclusion, that the two measurements are absolutely incompatible. Even more dramatic, this

[2] Both provided by Robert Reischke.

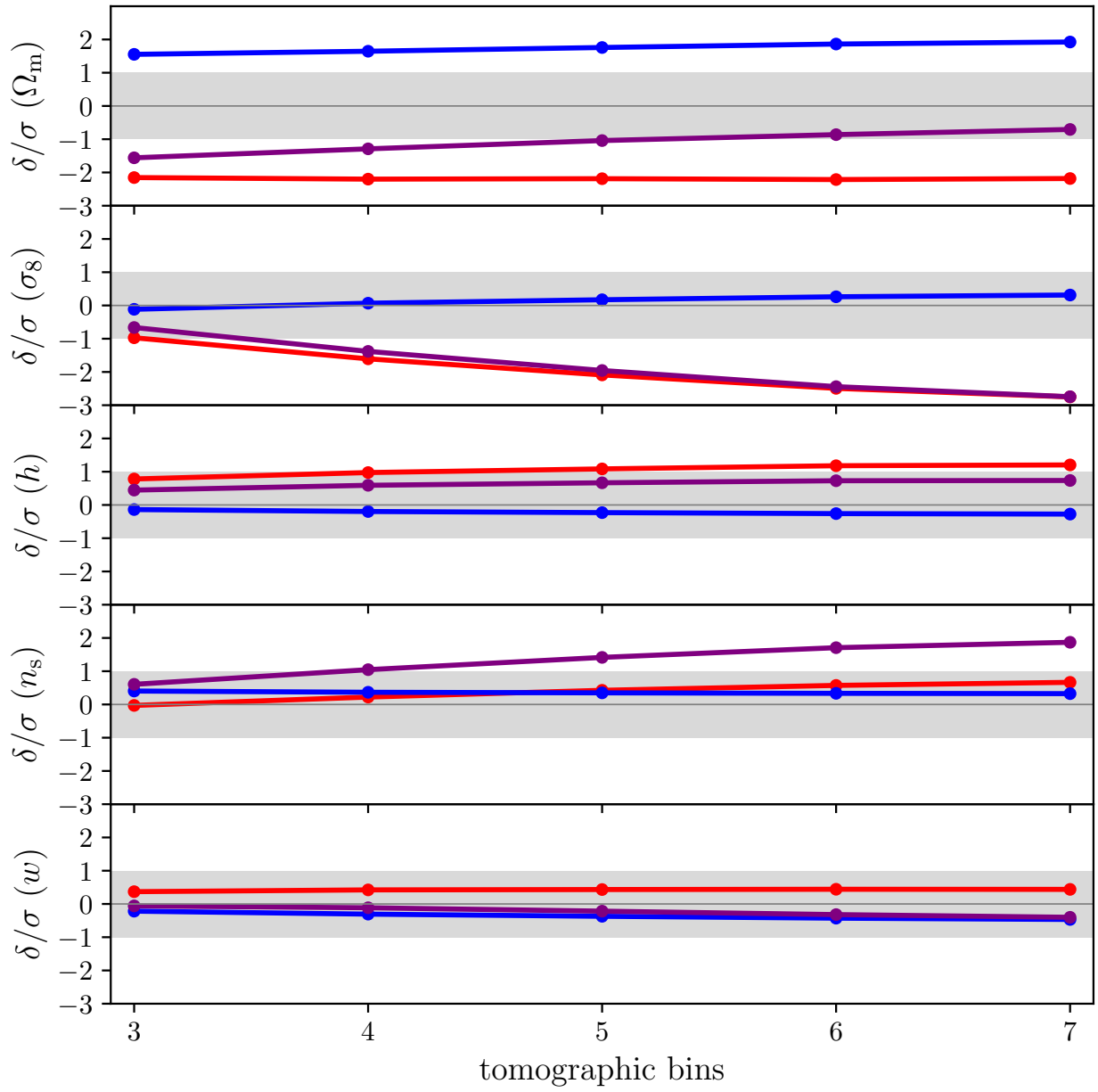

Figure 6.3: Parameter estimation biases for 3–7 tomographic bins in a Euclid–like survey for each parameter. The purple lines represent the bias normalised by its marginalised statistical standard deviation $\sigma = \sqrt{(F^{-1})_{\mu\mu}}$ when fitting a pure lensing–model to the true covariance with a mixed model, the red lines do the same for a pure elliptical galaxy model and the blue ones for an all spiral–alignment model.

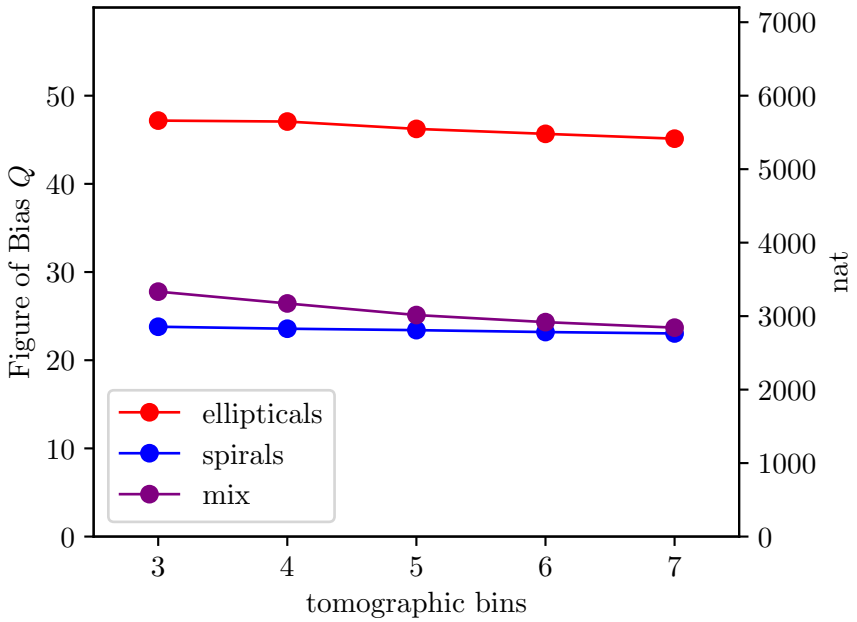

Figure 6.4: Figure of bias $Q^2 = \sum_{\mu,\nu} \delta_\mu F_{\mu\nu} \delta_\nu$ for the three models as a function of tomographic bins. On the right side, the axis is converted the natural units of the Kullback–Leibler–divergence, nat, quantifying the information or entropy using the natural logarithm.

seems to increase with the number of bins, such that close attention must be paid in the tradeoff between adding another tomographic bin and the change in bias. If intrinsic alignments can somehow be dealt with or modelled fairly well, this issue could be remedied. Thus, given a standard ΛCDM model, ignoring intrinsic alignments of the sort examined in this work in a Euclid–like survey would lead to strong doubts whether the model is actually correct, even though it would be correct.

To summarise, the figure of bias Q^2 gives a good quantification of the total bias induced by using a false model to fit the data, and can give an idea of the 'wrongness' of the model. This is constant with increasing bins. The Bayesian evidence compares two models to a prior, which can give dramatic results, like excluding the correct model just because of an untreated bias due to intrinsic alignments. The Bayesian evidence is also not stable with increasing bin number, making the need to deal with intrinsic alignments for a high-bin number survey trying to find evidence for or against e.g. ΛCDM more urgent.

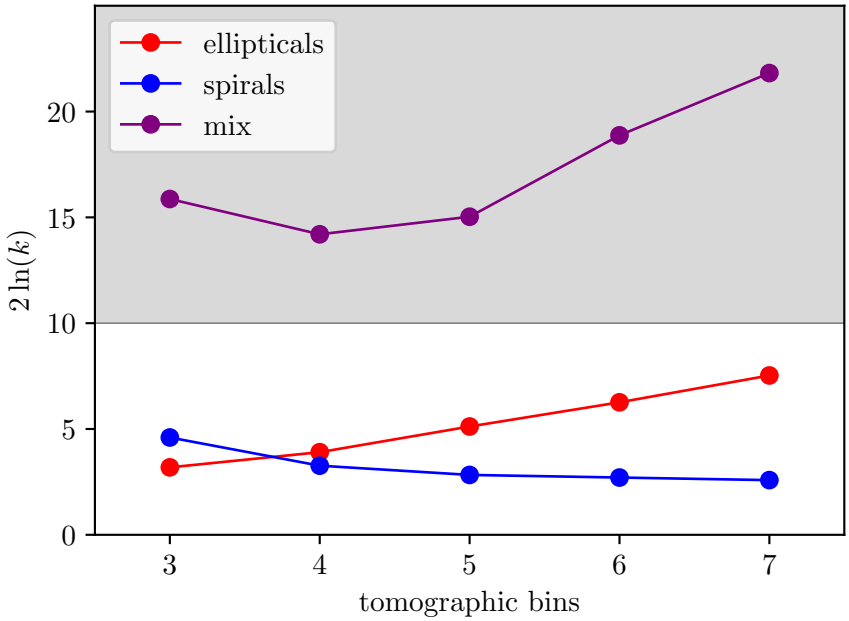

Figure 6.5: Bayesian evidence k of the different alignment models with respect to a CMB prior with increasing bin number. The grey area is what would be classified as 'very strong incompatibility' between the CMB prior and the false weak lensing covariance (Kass & Raftery, 1995; Nesseris & Garcia-Bellido, 2013).

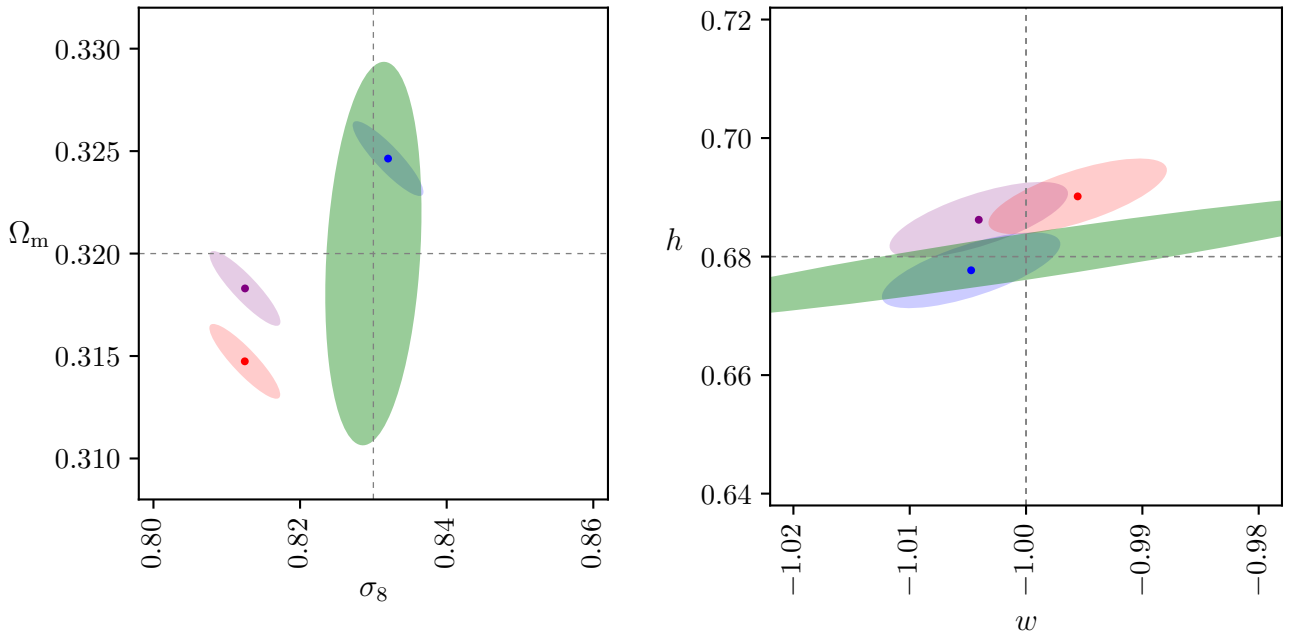

Figure 6.6: Same as Fig. (6.7), just a more detailed view and only showing the CMB prior. The blue ellipse (spiral model) is well contained within the CMB–ellipse, whereas the other two are shifted perpendicular to the direction of degeneracy, giving them a higher penalty in Bayesian evidence than if they were shifted in another direction.

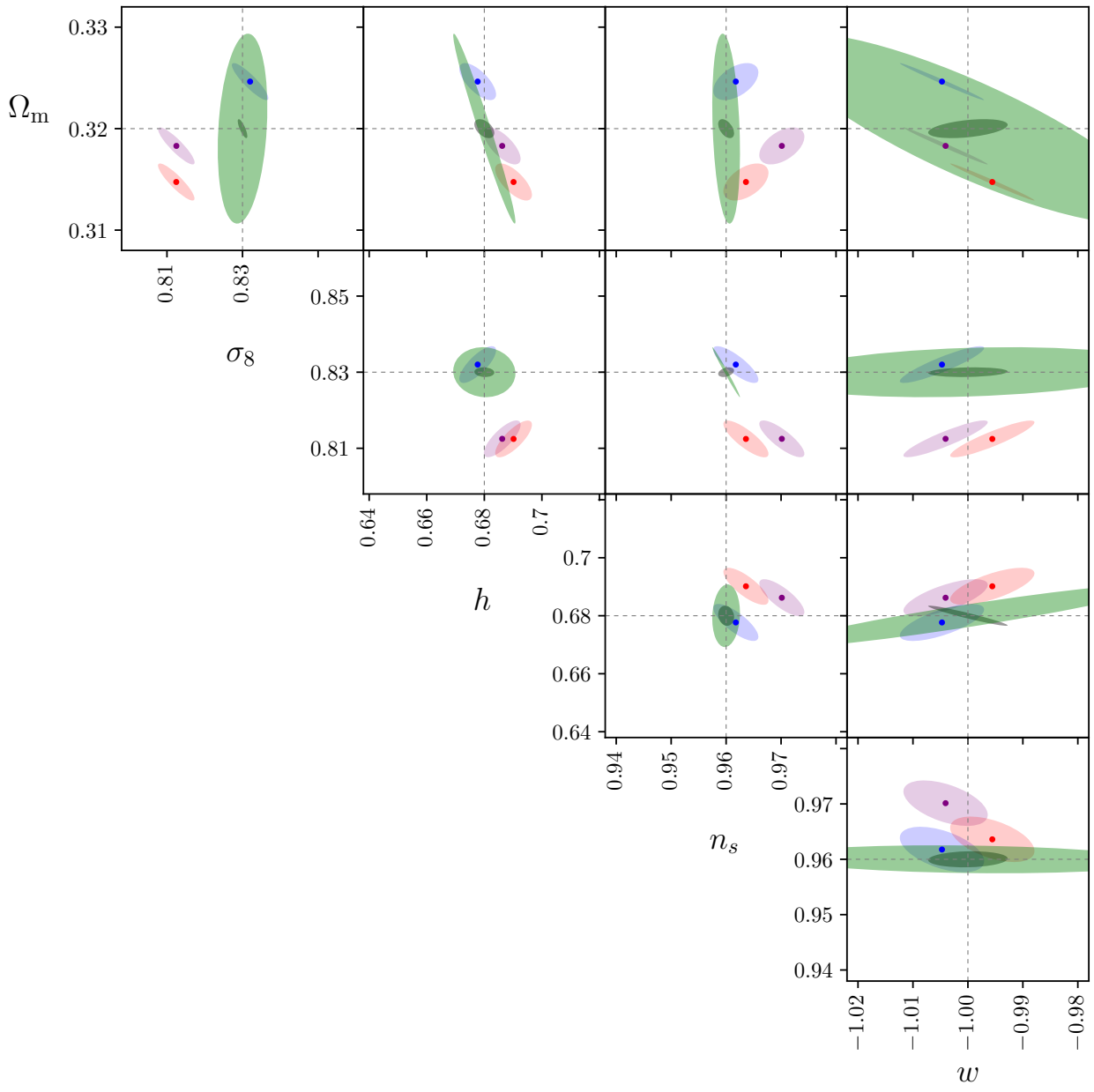

Figure 6.7: Error ellipses for all three IA models using 7 tomographic bins, shown with their respective error ellipse around them. In the middle (fiducial values) are the CMB–prior (green) and the BAO–pior (grey). The Bayesian evidence quantifies the overlap of the probabilities and finds the ratio of shifted vs. unshifted posterior.

7 Separation of Intrinsic Alignment and Weak Lensing Signals

In this chapter, I will present and review a method of splitting the galaxy sample according to galaxy colour (broadly called red and blue) and will show how this can be used to deal with intrinsic alignments of the kind that have been studied in this work so far. For one, one can maximise the lensing signal, minimising the bias induced by fitting the wrong model to the data, or one can completely eliminate the lensing covariance, making the measurement of pure intrinsic alignments possible, which would enable a fit of the alignment amplitude parameters A and D. I will also quantify the effects of misclassification of red and blue galaxies according to the two models for ellipticals and spirals respectively on this method. This chapter is based on a paper which will be released shortly, Tugendhat et al. (2018).

7.1 Idea and Method

A tomographic survey of ellipticities ε is separated by its colour information in two maps, $\varepsilon_{\mathrm{e},i}$ for ellipticals and $\varepsilon_{\mathrm{s},i}$ for spirals, where i stands for the ith tomographic bin. Both will experience lensing, such that

$$\varepsilon_{\mathrm{s},i} = \gamma_i + \epsilon_{\mathrm{s},i}, \tag{7.1}$$

$$\varepsilon_{\mathrm{e},i} = \gamma_i + \epsilon_{\mathrm{e},i}, \tag{7.2}$$

assuming that both galaxy types are affected the same by lensing. In practice, this might be more complicated, as their ellipticity measurements can differ systematically due to their structure or because of second order effects like lensing of pre-aligned galaxies (Giahi-Saravani & Schaefer, 2014). The overall covariance matrix of the data vector $(\varepsilon_{\mathrm{s},i},\varepsilon_{\mathrm{e},i'})$ with length $2n_{\mathrm{bin}}$ is then a $2n_{\mathrm{bin}} \times 2n_{\mathrm{bin}}$–matrix,

$$C_t(\ell) = \begin{pmatrix} C^{\mathrm{ss}}_{ij}(\ell) & C^{\mathrm{se}}_{ij'}(\ell) \\ C^{\mathrm{es}}_{i'j}(\ell) & C^{\mathrm{ee}}_{i'j'}(\ell) \end{pmatrix}, \tag{7.3}$$

where the four shown entries are each $n_{\mathrm{bin}} \times n_{\mathrm{bin}}$. The $C(\ell)$ can be split up in their signal and noise parts, $C_t(\ell) = S_t(\ell) + N_t(\ell)$. Then the signal–part is, including lensing and intrinsic alignments,

$$S_t(\ell) = \begin{pmatrix} n_s^2 \left(C^{\gamma}_{ij}(\ell) + C^{\mathrm{s},II}_{ij}(\ell)\right) & n_s n_e \left(C^{\gamma}_{ij'}(\ell) + C^{\mathrm{e},GI}_{ij'}(\ell)\right) \\ n_s n_e \left(C^{\gamma}_{i'j}(\ell) + C^{\mathrm{e},GI}_{i'j}(\ell)\right) & n_e^2 \left(C^{\gamma}_{i'j'}(\ell) + 2C^{\mathrm{e},GI}_{i'j'}(\ell) + C^{\mathrm{e},II}_{i'j'}(\ell)\right) \end{pmatrix}, \tag{7.4}$$

and the noise $N_t(\ell)$,

$$N_t(\ell) = \sigma_\epsilon^2 \, n_{\mathrm{bin}} \begin{pmatrix} n_{\mathrm{s}}\delta_{ij} & 0 \\ 0 & n_{\mathrm{e}}\delta_{i'j'} \end{pmatrix}. \tag{7.5}$$

The side-diagonals are zero here because a galaxy isn't at the same time of spiral and elliptical type, therefore there is no noise in the cross–correlations. As throughout this work σ_ϵ is set to 0.3. Note that n_s and n_e refers to the number of the spirals and ellipticals respectively, therefore, e.g. $n_e = (1-q)n$ with the spiral fraction q.

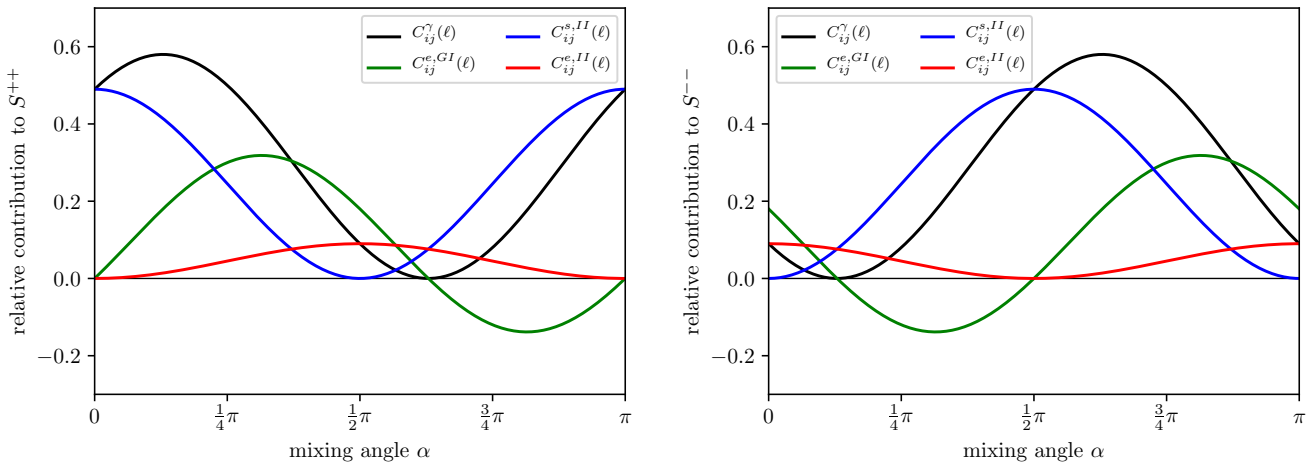

Figure 7.1: Relative contributions to separated spectra $S_{ij}^{++}(\ell)$ (left panel) and $S_{ij}^{--}(\ell)$ (right panel). Note that they are identical except for a phase difference of $\varphi = \pi/2$. As throughout this work, black is the weak lensing contribution, red the II–alignment of elliptical galaxies, green the ellipticals' GI contribution, and blue the spiral II-alignment. They have already been weighed by their respective spiral fraction factor, hence the much lower amplitude of ellipticals compared to spirals.

The two maps for spirals and ellipticals can be superposed in order to change the weight of the individual contributions of the spectra. The most convenient way to parametrise this is a mixing– or separation angle α:

$$\varepsilon_{+,i} = +\cos\alpha\,\varepsilon_{\mathrm{s},i} + \sin\alpha\,\varepsilon_{\mathrm{e},i}, \tag{7.6}$$

$$\varepsilon_{-,i} = -\sin\alpha\,\varepsilon_{\mathrm{s},i} + \cos\alpha\,\varepsilon_{\mathrm{e},i}\,. \tag{7.7}$$

Thus the covariance matrix $C_t(\ell)$ is transformed according to

$$C_{ij}^{\pm}(\ell) = UC_t(\ell)U^T, \quad \text{with} \quad U = \begin{pmatrix} \cos\alpha & \sin\alpha \\ -\sin\alpha & \cos\alpha \end{pmatrix}. \tag{7.8}$$

Since U is an orthogonal mapping ($U^T = U^{-1}$), which preserves the trace and the statistical quantities Σ and $F_{\mu\nu}$ are traces over a covariance, the statistical errors are not changed. Note that this is not the case for an individual $n_{\mathrm{bin}} \times n_{\mathrm{bin}}$–corner of $C_{ij}^{\pm}(\ell)$. Here, the statistical error can indeed change with α. The signal–part of the upper left corner of $C_{ij}^{++}(\ell)$, called $S_{ij}^{++}(\ell)$, is given by

$$\begin{aligned} S_{ij}^{++}(\ell) = \quad & (n_s\cos\alpha + n_e\sin\alpha)^2\, C_{ij}^{\gamma}(\ell) \\ & +2\left(n_s n_e\cos\alpha\sin\alpha + n_e^2\sin^2\alpha\right) C_{ij}^{\mathrm{e},GI}(\ell) \\ & +n_s^2\cos^2\alpha\, C_{ij}^{\mathrm{s},II}(\ell) \\ & +n_e^2\sin^2\alpha\, C_{ij}^{\mathrm{e},II}(\ell)\,. \end{aligned} \tag{7.9}$$

This can be used to set individual contributors to the spectrum to zero, e.g. for $n_s = n_e$, both II–contributions could be isolated from lensing and GI for $\alpha = 3\pi/4$. For a more complicated relation between n_s and n_e, the

roots wouldn't have such simple α. However, they can be found numerically. In fact, for $q = 0.7$, this point is at $\alpha' \approx 1.976$. Analogous to $S_{ij}^{++}(\ell)$, the noise becomes

$$N_{ij}^{++}(\ell) = \sigma_\epsilon^2 \, n_{\rm bin} \left(n_s \cos^2 \alpha + n_e \sin^2 \alpha \right) . \tag{7.10}$$

The total covariance is then $C_{ij}^{++}(\ell) = S_{ij}^{++}(\ell) + N_{ij}^{++}(\ell)$.

7.2 Misclassification

In the previous section, the split was denoted with e and s, however, the actual data will most conveniently be split according to colour information. This isn't a perfect method to classify galaxies. Therefore, there needs to be a measure of misclassification that contaminates the red galaxies with some that align due to the tidal torque model (i.e. spirals) and vice versa for the blue galaxies some that align with tidal shear (ellipticals). The number of blue and red galaxies can be expressed as

$$n_b = p(b|b)n_s + p(b|r)n_e, \tag{7.11}$$

$$n_r = p(r|b)n_s + p(r|r)n_e, \tag{7.12}$$

with the condition that $p(r|r) = 1 - p(b|r)$ and $p(b|b) = 1 - p(r|b)$, the total number of galaxies is conserved. Setting the $p(r|b) = p(b|r) = 0$ recovers the results of the previous section. A misclassification gives rise to different amplitudes than expected from a given q, as well as possible cross–correlations between blue and red. Analogous to equation (7.7), we now have

$$\varepsilon_{b,i} = \gamma_i + p(b|b)\epsilon_{s,i} + p(b|r)\epsilon_{e,i}, \tag{7.13}$$

$$\varepsilon_{r,i} = \gamma_i + p(r|b)\epsilon_{s,i} + p(r|r)\epsilon_{e,i}, \tag{7.14}$$

and a covariance matrix

$$C_f(\ell) = \begin{pmatrix} C_{ij}^{bb}(\ell) & C_{ij'}^{br}(\ell) \\ C_{i'j}^{rb}(\ell) & C_{i'j'}^{rr}(\ell). \end{pmatrix}, \tag{7.15}$$

with a signal parts $S_f(\ell)$

$$S_f^{bb}(\ell) = n_b^2[C_{ij}^{\gamma}(\ell) + 2p(b|r)C_{ij}^{e,GI}(\ell) + p(b|b)^2 C_{ij}^{s,II}(\ell) + p(b|r)^2 C_{ij}^{e,II}(\ell)], \tag{7.16}$$

$$S_f^{br}(\ell) = n_b n_r[C_{ij'}^{\gamma}(\ell) + C_{ij'}^{e,GI}(\ell) + p(b|b)p(r|b)C_{ij'}^{s,II}(\ell) + p(b|r)p(r|r)C_{ij'}^{e,II}(\ell)], \tag{7.17}$$

$$S_f^{rb}(\ell) = n_b n_r[C_{i'j}^{\gamma}(\ell) + C_{i'j}^{e,GI}(\ell) + p(b|b)p(r|b)C_{i'j}^{s,II}(\ell) + p(b|r)p(r|r)C_{i'j}^{e,II}(\ell)], \tag{7.18}$$

$$S_f^{rr}(\ell) = n_r^2[C_{i'j'}^{\gamma}(\ell) + 2p(r|r)C_{i'j'}^{e,GI}(\ell) + p(r|b)^2 C_{i'j'}^{s,II}(\ell) + p(r|r)^2 C_{i'j'}^{e,II}(\ell)], \tag{7.19}$$

and noise part $N_f(\ell)$,

$$N_f(\ell) = \sigma_\epsilon^2 \, n_{\rm bin} \begin{pmatrix} n_b\delta_{ij} & 0 \\ 0 & n_r\delta_{i'j'} \end{pmatrix}. \tag{7.20}$$

For the purpose of illustration, I will choose the misidentification probabilities to be rather high $p(b|r) = p(r|b) = 0.1$, i.e. 10 per cent of all galaxies get misclassified. The lensing part doesn't change, as lensing does not depend on galaxy type in this context (discussed in the previous section). Fig. (7.2) shows the relative contributions of the 4 constituents with $q = 0.7$ and misclassification rates as above for the dashed lines, and

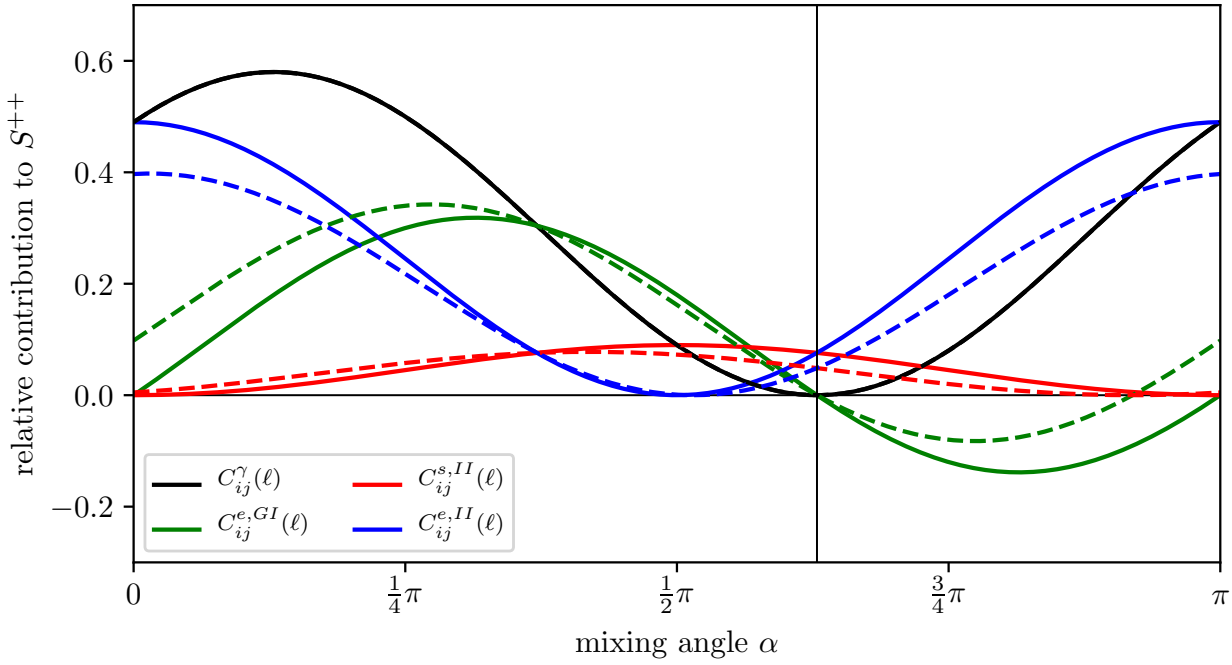

Figure 7.2: Relative contributions to C_t^{++} (solid lines) and C_f^{++} (dashed lines) Spectrum with Misclassification.

perfect classification ($p(b|r) = p(r|b) = 0$) for the solid lines. Most significantly, the root at $\alpha = \alpha'$ doesn't move, which makes it easier to deal with smaller misclassification rates in that case. The relative amplitudes of the II–alignments shrink, but lensing and GI–alignments are switched off safely.

7.3 Maximising the Intrinsic Alignment Signal

The difference between the correctly classified covariance and the misclassified one can be expressed as $\langle \Delta\chi^2 \rangle$ between the two models. Hence, if $C_{ij}^{++}(\ell)$ is the contribution from the α'-rotated $C_t(\ell)$ and $X_{ij}^{++}(\ell)$ is the one from the α'-rotated $C_f(\ell)$ including wrongly identified galaxies.

$\langle \chi^2 \rangle$ for the correctly identified and misclassified covariances is then, respectively,

$$\langle \chi_t^2 \rangle = f_{\text{sky}} \sum_{\ell} (2\ell + 1) \operatorname{tr} \left[\ln C^{++}(\ell) + \text{id} \right], \quad \text{and} \tag{7.21}$$

$$\langle \chi_f^2 \rangle = f_{\text{sky}} \sum_{\ell} (2\ell + 1) \operatorname{tr} \left[\ln X^{++}(\ell) + X_{++}^{-1}(\ell) C^{++}(\ell) \right]. \tag{7.22}$$

The difference $\langle \Delta\chi^2 \rangle = \langle \chi_f^2 - \chi_t^2 \rangle$ between the true and false model is then,

$$\langle \Delta\chi^2 \rangle = f_{\text{sky}} \sum_{\ell} (2\ell + 1) \left(\ln \left(\frac{\det X^{++}(\ell)}{\det C^{++}(\ell)} \right) + \operatorname{tr} \left[X_{++}^{-1}(\ell) C^{++}(\ell) \right) - n_{\text{bin}} \right], \tag{7.23}$$

where it was assumed that C_t yields the average expected data. In case of $X^{++} = C^{++}$, it is obvious from this that $\langle \Delta\chi^2 \rangle = 0$. The results for $\langle \Delta\chi^2 \rangle$ for $\alpha = \alpha'$ and $p(b|r) = p(r|b) = 0.1$ can be seen in Fig. (7.3). The difference between the two model adds up over ℓ, with a bit of a dip at intermediate redshifts, where the

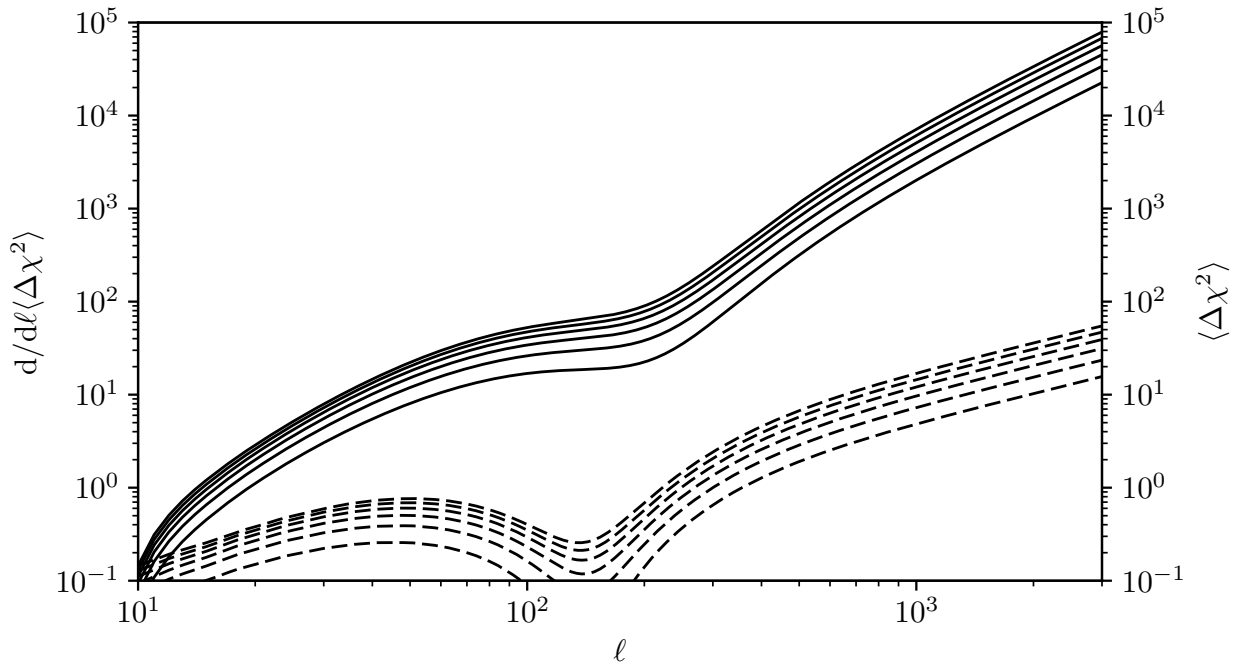

Figure 7.3: Difference $\langle\Delta\chi^2\rangle$ between $X_{++}(\ell)$ and $C_{++}(\ell)$ for $2-7$ tomographic bins assuming a misclassification rate of $p(b|r) = p(r|b) = 0.1$. Dashed lines show differential $\langle\Delta\chi^2\rangle$.

spiral E–modes are overtaking the ellpticals' E–mode. The difference is quite large, however, the estimate of $p(b|r) = p(r|b) = 0.1$ might be on the high end as well.

Isolating intrinsic alignments brings the chance of measuring the alignments alone without lensing 'contamination', making it possible to fit the models to data. The signal to noise-ratio

$$\Sigma^2 = f_{\mathrm{sky}} \sum_{\ell} \frac{2\ell+1}{2} \mathrm{tr}\left(C_{++}^{-1}(\ell) S^{++}(\ell)\, C_{++}^{-1}(\ell) S^{++}(\ell)\right). \tag{7.24}$$

is shown for a Eulcid–like survey in Fig. (7.4). For $n_{\mathrm{bin}} > 5$, a Σ of $\gtrsim 55$ is expected, which would be enough to consider fitting A and D to the data. A conditionalized Fisher–matrix between A and D is illustrated in Fig. (7.5) for 3 and 7 tomographic bins. The direction of degeneracy isn't surprising, as increasing one parameter would lead to a need to decrease the other to produce a similar amplitude. For this, every other parameter that intrinsic alignments are sensitive has been conditionalized, such that an ellipse with this size could only be possible with a strong prior on the rest of the cosmological parameters or would have to become larger as more parameters are varied. This would not be ideal, as the relatively low Σ wouldn't allow for many more than 2 parameters to be fitted, thus a strong prior would be preferable.

7.4 Reducing the Intrinsic Alignment Contamination

Other than eliminating lensing, this method can also be used to maximise the contribution that lensing has on the covariance, by setting $\alpha = \alpha_\gamma \approx 0.405$ for a spiral fraction of $q = 0.7$. Because of its different phases for different contributions, intrinsic alignments can never be completely set to zero. However, it is possible to calculate the figure of bias Q as a function of α to measure how large the systematic error due to intrinsic alignments is with respect to the statistical error. This is much more dependent on the misclassification rates,

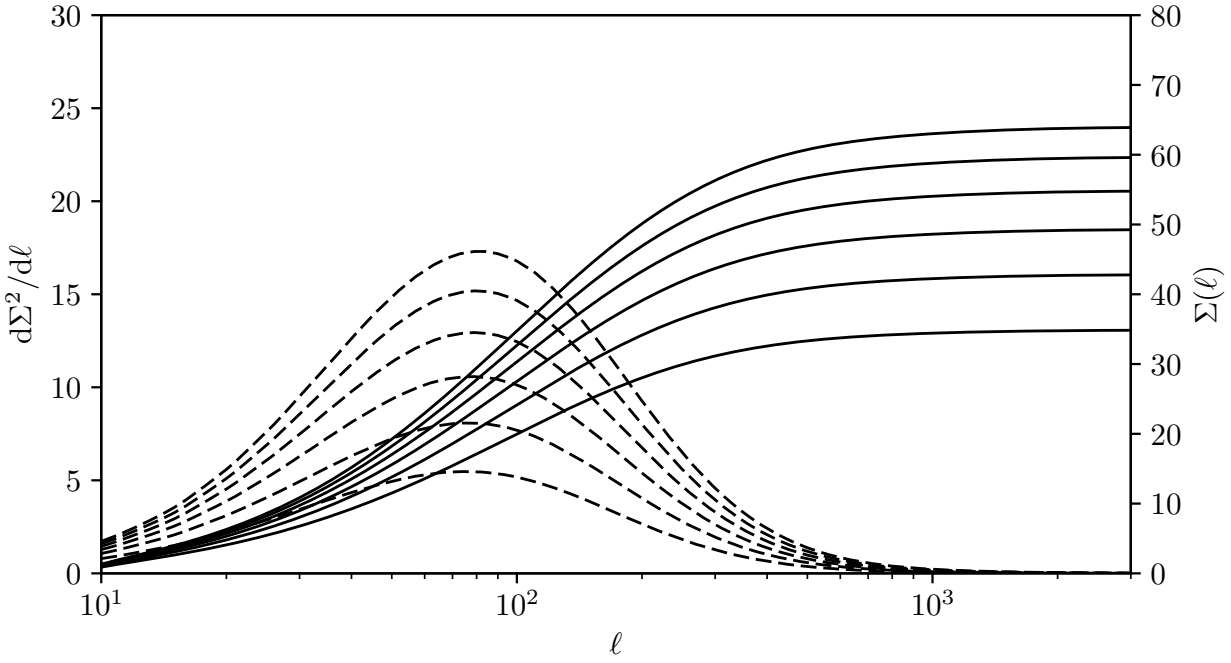

Figure 7.4: Signal to noise-ratio Σ for intrinsic alignment signals assuming no misclassification, for 2 − −7 tomographic bins. Dashed lines show the differential signal to noise–ratio.

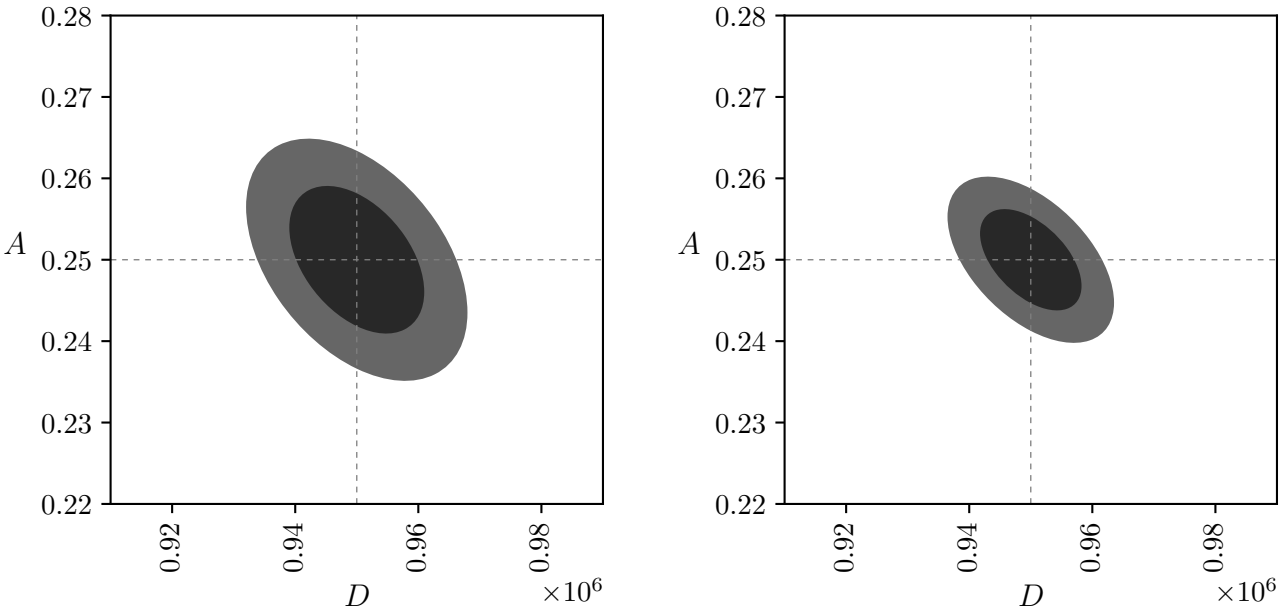

Figure 7.5: Fisher–ellipses of alignment parameters *A* and *D* fitted through eliminating lensing and measuring them directly, conditionalizing every other free parameter.

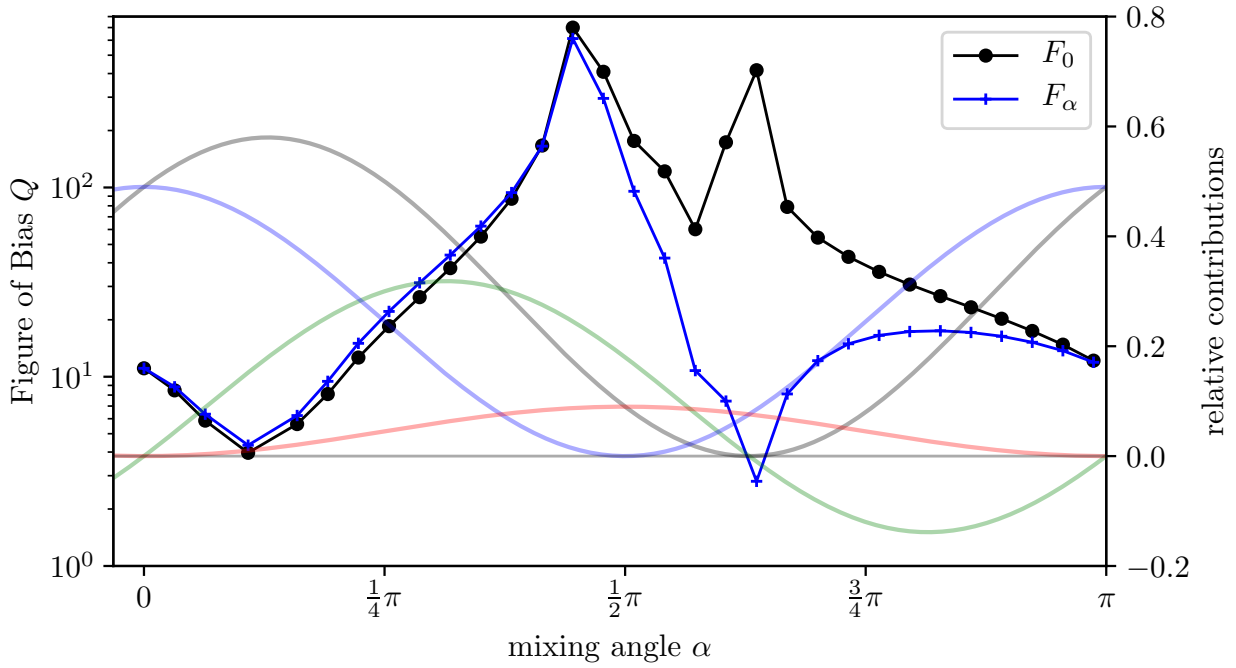

Figure 7.6: Figure of bias $Q(\alpha)$ for different mixing angles α The black curves measures δ_μ in the constant Fisher matrix $F_{\mu\nu}(\alpha = 0) = F_0$, whereas the blue curve calculates Q via the local lensing–only Fisher matrix F_α. In the background are the relative contributions to the covariance with the usual colour scheme from e.g. Fig. (7.1)

the individual model amplitudes, etc. than the previous case, where the lensing could just be eliminated for a given q. The figure of bias is calculated just like in section 6.2 with the exception that $C^{++,-1}(\ell, \alpha)$. The derivatives $\partial_\mu S^{++}(\ell, \alpha)$ are approximated as $\partial_\mu C^\gamma(\ell, \alpha)$ as weak lensing is dominating in the regions that we are interested in, which is the region around α_γ. For the bias vector $\delta_\mu(\alpha)$, the equations $\delta_\mu = \sum_\nu G^{-1}_{\mu\nu} a_\nu$ are solved without approximations, as the derivatives of the intrinsic alignment spectra aren't needed. The results (Fig. (7.6)) are encouraging, the figure of bias is cut by about 50 per cent between $\alpha = 0$ and $\alpha = \alpha_\gamma$. The similarity of the curves using two different Fisher–matrices is also encouraging the choice of approximation that was made. Of course, this breaks down when the lensing contribution starts to vanish and intrinsic alignments take over, once the lensing signal comes back around $\alpha \to \pi$, the approximation starts to work again. The blue F_α curve dips at $\alpha = \alpha'$ because the Fisher matrix becomes so large when the lensing goes to zero that the figure of bias is small no matter how large the bias vector. the constant F_0 shows a different behaviour, namely a relatively large figure of bias.

The method shown here has its drawbacks: the statistical accuracy is diminished in order to sub–sample different galaxy sets and the sampling itself (i.e. by colour) is known to be prone to misclassifications. If more sophisticated methods become available to distinguish between morphologies, this approach becomes ever more viable, at least to constrain certain alignment parameters. Of course this method can be used with any number and type of intrinsic alignment models, as long as they produce a known E– or B–mode spectrum. It became especially simple here because on of our models doesn't produce GI–alignments. However complicated the models are, however, a point can always be found that eliminates lensing.

8 Using Intrinsic Alignments to Test General Relativity

In this chapter, I would like to sketch how intrinsic alignments could be used to probe deviations from general relativity. The idea behind it is simply measuring the difference between the potentials $\Psi + \Phi$ and Ψ: as already stated in section 2.4, we can write the scalar perturbations of the metric with the Bardeen potentials Ψ and Φ as

$$\mathrm{d}s^2 = -\left(1 + \frac{2\Psi}{c^2}\right)\mathrm{d}t^2 + a^2\left(1 - \frac{2\Phi}{c^2}\right)\mathrm{d}\boldsymbol{x}^2. \tag{8.1}$$

In normal general relativity, $\Phi = \Psi$, i.e. there is no anisotropic stress. Now the challenge is to find different probes of the two potentials and cross-correlate them in order to constrain the difference between Φ and Ψ. This has been done with weak lensing before, together with redshift space distortions (e.g. Simpson et al., 2013) or other large-scale-structure probes (e.g. Blake et al., 2016), as well as using the cosmic microwave background (Planck Collaboration, 2015).

8.1 Gravitational Slip in Weak Lensing and Intrinsic Alignments

The idea is to use weak lensing to probe the sum of both potentials as has been done in the mentioned studies before, but not use a different probe for Ψ, but rather the intrinsic alignments of elliptical, galaxies, which are sensitive to the Newtonian potential Ψ alone, not unlike redshift space distortions or other large–scale structure probes. This would eliminate the fact that in those measurements, the systematics from two probes enter. However, for this to work, the galaxy sample needs to be separated similarly to chapter 7 into red and blue galaxies, whilst only the red ones are kept to be fitted to a combined covariance

$$C^{\mathrm{e}}_{ij}(\ell) = C^{\gamma}_{ij}(\ell) + C^{\mathrm{e},GI}_{ij}(\ell) + C^{\mathrm{e},II}_{ij}(\ell). \tag{8.2}$$

For this, all we need is the power spectra of the altered potentials (Newtonian Ψ and Weyl $\Psi + \Phi$); defining the first slip parameter

$$\eta(\boldsymbol{k},a) = \frac{\Phi}{\Psi}, \tag{8.3}$$

which evidently is $\eta = 1$ for general relativity, the three Poisson equations for the potentials and their sum can be written as (Amendola et al., 2008)

$$-k^2\frac{\Psi}{c^2} = 4\pi G a^2 \mu(\boldsymbol{k},a)\rho_{\mathrm{bg}}\delta, \tag{8.4}$$

$$-k^2\frac{\Phi}{c^2} = 4\pi G a^2 \eta(\boldsymbol{k},a)\mu(\boldsymbol{k},a)\rho_{\mathrm{bg}}\delta, \tag{8.5}$$

$$-k^2\frac{\Phi+\Psi}{c^2} = 4\pi G a^2 \left[\eta(\boldsymbol{k},a)\left(\mu(\boldsymbol{k},a)+1\right)\right]\rho_{\mathrm{bg}}\delta. \tag{8.6}$$

The resulting power spectra now end up with the factors

$$P_\Psi(k,a) = \mu(\boldsymbol{k},a)^2\, P_\Phi^{\mathrm{GR}}(k,a), \tag{8.7}$$

$$P_\Phi(k,a) = \eta(\boldsymbol{k},a)^2\, \mu(\boldsymbol{k},a)^2 P_\Phi^{\mathrm{GR}}(k,a), \tag{8.8}$$

$$P_{\Phi+\Psi}(k,a) = \frac{1}{4}\left[\eta(\boldsymbol{k},a)\,(\mu(\boldsymbol{k},a)+1)\right]^2 P_\Phi^{\mathrm{GR}}(k,a), \tag{8.9}$$

where $P_\Phi^{\mathrm{GR}}(k,a)$ means the power spectrum so far used in this work. Since the gravitational potentials only enter directly here in lensing and intrinsic alignments – i.e. via two point correlations, this can be used as a first proof of concept. Naturally, a modified gravity model would also change the way that the a–normalised growth function D_+/a behaves, it would change the normalisation of the power spectrum σ_8, and would change the transfer function for the non-linear end of the power spectrum. Since this is still working in the scope of a metric theory of gravity with little deviations from general relativity, the lensing formalism should stay the same. Furthermore, the tidal shear model might break down due to unforeseen consequences e.g. in galactic dynamics.

However, to mitigate the transfer function, I will use a cutoff for the nonlinear power spectra like in equation (5.30) at $m_{\mathrm{cut}} = 1\times10^{12}M_\odot/h$, for both lensing and the elliptical model, in order to minimise the influence of stark changes in this modified gravity of the behaviour of matter at small scales. I will still assume to be able to separate the a–dependency of the power spectrum in form the growth function.

The lensing shear then becomes

$$\gamma_i^{\mathrm{mg}}(\theta,\chi) = \int_0^{\chi_H} \mathrm{d}\chi W_i'(\chi)\left(\partial_{yy}^2 - \partial_{xx}^2 + 2\mathrm{i}\partial_{xy}\right)(\Phi+\Psi)\,. \tag{8.10}$$

with the new weighting function W_i',

$$W_i'(\chi) = \frac{D_+}{a}\frac{G(\chi)}{\chi}. \tag{8.11}$$

Note that the factor 2 doesn't appear here like in equation (3.35). The lensing power spectrum then ends up as

$$C_{ij}^{\gamma,\mathrm{mg}}(\ell) = \frac{\ell^4}{4}\int_0^{\chi_H}\frac{\mathrm{d}\chi}{\chi^2}W_i(\chi)W_j(\chi)\left[\eta(k=\ell/\chi,a)\,(\mu(k=\ell/\chi,a)+1)\right]^2 P_\Phi^{\mathrm{GR}}\left(k=\ell/\chi,\chi\right). \tag{8.12}$$

Where I went back to using the W_i from standard lensing. In case of the W_i', the prefactor would be $\ell^4/16$. This, of course, assumes that the Limber–approximation (see section 3.2) is still valid. But seeing as the parameters η and μ very likely do not vary wildly in χ, this can be done without worrying too much about it.

For intrinsic alignment, the power spectrum appears in the ζ-functions,

$$\zeta_n^{\mathrm{mg}}(r) = \frac{(-1)^n}{r^{4-n}}\int\frac{k^{n+2}\mathrm{d}k}{2\pi^2}P_\Psi(k)\,j_n(kr) = \mu(a)^2\,\zeta_n(r). \tag{8.13}$$

The last step is only valid if μ is not scale–dependent. For the II–alignments, this is enough to adapt them to the η and μ parameters. In the case of GI–alignments, the correlations become (cf. section 5.1)

$$\left\langle\gamma_a\epsilon_b'\right\rangle = \pm\int_0^{\chi_H}\mathrm{d}\chi\ \frac{W'(\chi)}{D}\left\langle\epsilon_a\,\epsilon_b'\right\rangle. \tag{8.14}$$

Therefore, the ζ used to maintain partial sensitivity to $\Phi + \Psi$ can be adapted to

$$\zeta_n^{\mathrm{mg},GI}(r) = \frac{(-1)^n}{r^{4-n}} \int \frac{k^{n+2}\mathrm{d}k}{2\pi^2} \sqrt{P_{\Phi+\Psi}(k)P_{\Psi}(k)}\, j_n(kr) = \mu(a)\ [\eta(a)\,(\mu(a)+1)]\,\frac{\zeta_n(r)}{2}. \tag{8.15}$$

Once again, the last step is only valid if μ and η are not scale–dependent. At this point, it becomes apparent that this approach does have one great advantage: It is possibly quite sensitive to the k–dependence of both μ and η. In trying to compare my results to Planck Collaboration (2015), I will however assume them to be constant in scale.

8.2 Results from a naïve approach

The new covariance matrix for the entire signal in this case becomes

$$C_{ij}^{\mathrm{mg}}(\ell) = C_{ij}^{\gamma,\mathrm{mg}}(\ell) + C_{ij}^{\epsilon,II,\mathrm{mg}}(\ell) + C_{ij}^{\epsilon,II,\mathrm{mg}}(\ell). \tag{8.16}$$

Here, I used the $\zeta_n^{\mathrm{mg}}(r)$ for II–alignment, and the $\zeta_n^{\mathrm{mg},GI}(r)$ for the GI–parts of the alignment model, explicitly in the scale–free case.

The Fisher–matrix becomes (cf. section 3.5)

$$F_{\sigma\rho} = f_{\mathrm{sky}} \sum_{\ell} \frac{2\ell+1}{2} \mathrm{tr}\left[(C^{\mathrm{mg}}(\ell))^{-1}\partial_\sigma C^{\mathrm{mg}}(\ell)\,(C^{\mathrm{mg}}(\ell))^{-1}\partial_\rho C^{\mathrm{mg}}(\ell)\right]. \tag{8.17}$$

I calculated the conditionalized Fisher–matrix for constant η and μ in scale and redshift for a survey like Euclid, to see the possibilities of constraining the two parameters with this approach. The derivatives take into account the change with η and μ for the full covariance, i.e. at each step, the ζ are calculated anew, which is why I assumed them to be constant, as to be able to pull them out of the integrals and become computationally more efficient.

Since the errors are already on the same order of magnitude (Fig. (8.1)) as the measurements from Planck (Fig. (8.2)) for constant η and μ, the errors for varying ones would be much larger.

Unfortunately, the direction of degeneracy is exactly the one from (Planck Collaboration, 2015), albeit not surprisingly; a decrease in lensing power must be countered by an increase of alignment power in order to produce the same power overall. A breaking of degeneracies is not possible in combination with the Planck–measurement.

It is doubtful that a full treatment with a fully modified gravity would produce any more accurate results; the biggest sources of uncertainties in this approach are surely not only the separation between red and blue galaxies, which has been discussed throughout this thesis, but also one needs to expect that the tidal shear model still holds for elliptical galaxies in the modified gravity context, and one has to have the alignment parameter D very well constrained, which is currently not the case (see section 5.3).

Nonetheless, this method has the potential to be powerful, if one constrains the dependencies of η and μ and if the alignment theory stands on firm ground. In principle, this can be done with any other alignment model that depends on the magnitude of local gravitational potentials, however it is particularly simple in this case as the linear alignment model is quite similar to lensing in dependency on the potential.

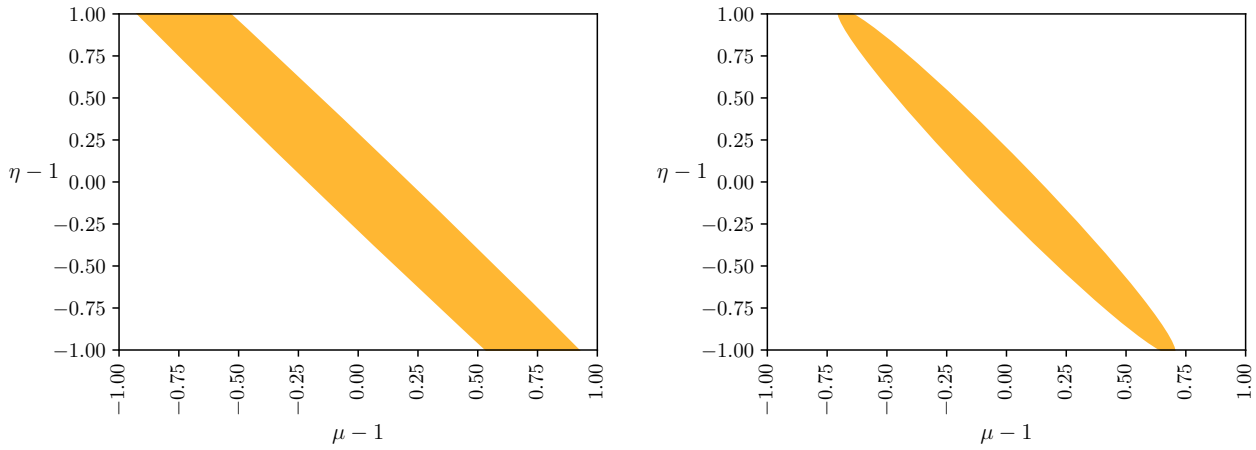

Figure 8.1: Fisher–matrix of slip parameters used here, η and μ, for 3 tomographic bins and 7 tomographic bins.

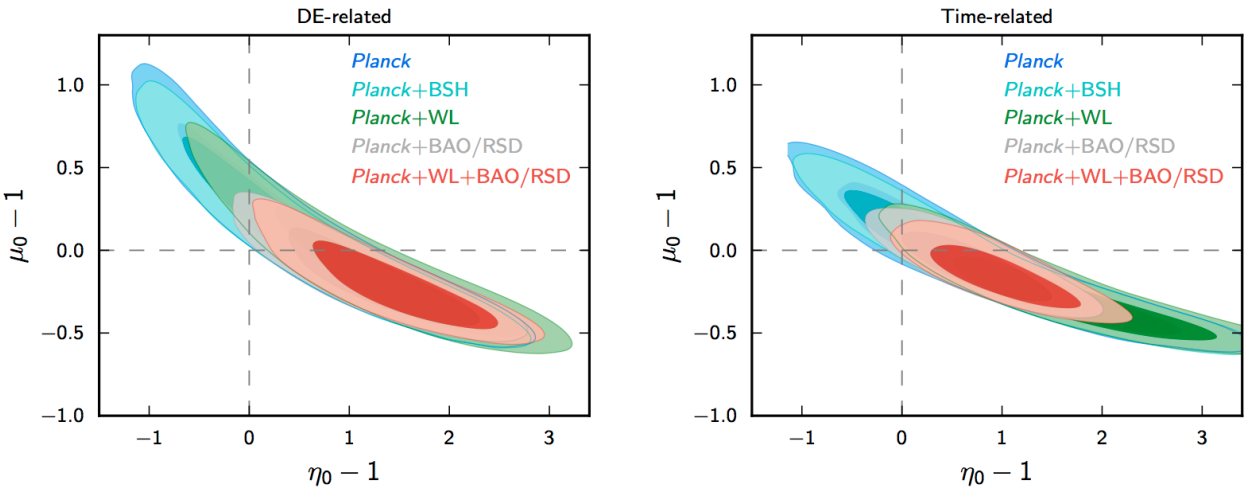

Figure 8.2: Degeneracies in dark energy–coupled (left panel) and time–dependent (right panel) η and μ from Planck, taken from Planck Collaboration (2015).

9 Conclusions

Within this thesis, I have presented the current and near–future state of tomographic weak gravitational lensing surveys and their limits with respect to intrinsic alignments in particular. The model for intrinsic alignments that was used was a physically motivated one, where the spiral galaxies exhibit alignment due to correlated angular momenta, whilst elliptical galaxies react to the current tidal shear. Hence, the spiral galaxies are strictly using the linear power spectrum to align themselves, Gaussianity prevents them from having a GI–alignment, as that would be a third moment, which is zero for Gaussian distributions. The elliptical galaxies exhibit both II– and GI–alignment, therefore filling the off-diagonals on the covariance matrix. The GI–alignments were shown to have B–modes, which were calculated and compared to the B–modes from the model used by spiral galaxies.

I motivated the use of a mixed model with a fixed spiral fraction q; a varying q could be implemented easily, however that would dilute the direct effects of the alignment models on lensing. Nevertheless, if q were measured to be wildly different from what I assumed and, against all evidence, varies extremely with e.g. redshift z, this could be remedied quickly and easily.

I also calculated the redundant S– and C– modes as consistency checks. From the E–modes, it was possible to determine the parameter estimation bias, i.e. systematic errors that a Euclid–like survey is likely to succumb to if it is not correcting for intrinsic alignments in its parameter inference. Instead of fitting one or two nuisance parameters (which are essentially equivalent to the alignment parameters), I tried to determine one of the parameters by using the CHFTLenS–alignment signal. As my value falls within the limits of other determinations (Hilbert et al., 2016) of the tidal shear amplitude parameter, I am confident that this approach is viable, given of course that the tidal shear is the only dominant alignment model for elliptical galaxies.

My results for the tidal shear and tidal torque model and their mix are similar to Blazek et al. (2017), who are taking a more mathematical approach – they are also working in Fourier space, whilst I am calculating the correlation functions in real space and then transform to Fourier–space. The advantage of Blazek et al. (2017) is that they find a spiral GI–alignment, which I am excluding from the start with arguing with Gaussianity. Their model comes at the cost of having spirals react to the absolute value of the gravitational potential, which is counterintuitive to the assumption that the alignment works via the angular momenta; the ellipticity thus observed cannot depend on the magnitude of the shear fields, only on its direction. Blazek et al. (2017) come to the same conclusion, namely that the models can be treated independently for different galaxy types. It would be interesting to see what the results were if one could calculate their model in Fourier space with a pure orientation-effect for spirals and how that would compare to the one presented in this work. Their predictions of the biases seem to match the ones from this work quite well, too. However their parameter set is not quite comparable to the one presented here, as they vary the alignment parameters as well as a few cosmological parameters.

In order to quantify the bias induced by not modelling intrinsic alignments in a Euclid–like survey, I calculated the figure of bias Q, which is also shown to be related to the Kullback–Leibler–divergence as $Q^2/2 = D_{\mathrm{KL}}$ for small biases and Gaussian likelihoods. Furthermore, I calculated the Bayesian evidence for a Planck–like CMB prior, which, if the mixed model is taken, would falsely exclude the model assumed for the prior (ΛCDM) to a high degree of confidence. Therefore, I conclude that especially for a probe like Euclid, it is vital to model

and constrain intrinsic alignments before inferring any cosmological information from the data. Other approaches, like excluding close pairs of galaxies (King & Schneider, 2002; Heymans & Heavens, 2003). The problem with discarding galaxies of small separation is that one still gets the intermediate E–mode from elliptical II alignment in my models, as well as the full force of the GI–alignment if both ℓ and z–separation is used to determine the distance of two galaxies: in fact, GIs aren't negligible at intermediate ℓ and large redshift–separation Δz. Small redshift–separation actually decreases GIs due to the waning lensing efficiency. Cross–correlating with other probes (e.g. Larsen & Challinor, 2016) can be promising, however they must give up statistical precision for systematic accuracy if the systematics of more than one probe need to be accounted for. This trade-off between unknown interactions as a source of noise in the data is somewhat reminiscent of WMAP, where secondary anisotropies such as the Zunyaev–Zel'dovich effect or the (integrated) Sachs–Wolfe effect needed –and still need– to be taken into account and corrected for with different measures, for example using masking certain regions for one effect, which might not be effective at all for the other.

Ultimately, it would be preferable to have models for intrinsic alignments that can be implemented in order to take full advantage of a survey like Euclid. As of today, I can see no way around multi-model adaption for different galaxy types. As of yet, I have not seen works on intrinsic alignments using neural networks; however, the danger in these is that the underlying physics can't be understood (if there is any), which is highly dissatisfactory for any physicist. The way for this might be via simulations (Hilbert et al., 2016), where our understanding of galaxy formation is being challenged and honed or through radio surveys and polarisation information (Brown & Battye, Brown & Battye).

I have presented another way of dealing with intrinsic alignments, which was to separate the galaxy sample by colour and then perform a orthogonal transformation in order to either maximise the lensing contribution (to the autocorrealtion of one of the two subsamples) or maximise the intrinsic alignment contribution in order to isolate and measure them separately, where their B–modes could offer a promising consistency check or could even be used for fitting as well if the models are sufficiently well understood and if the separation can be shown to be reliable. I examined the possibility of misclassification under this approach and came to the conclusion that even though the difference in $\langle \chi^2 \rangle$ can be large, the method could be feasible, as the misclassification rates were chosen to be quite large as well. One way or the other, this method hinges on the quality of being able to separate galaxies according to the applicable alignment model.

Within the same framework, I showed that maximising the lensing signal can lead to lower biases with respect to the statistical error, however, one sacrifices a large portion of the correlations by only using one 'corner' of the total covariance. Other mitigating techniques include avoiding galaxies that are too close (Catelan et al., 2001), but this doesn't work for GI–alignments, as I have argued before. Among others are nulling techniques (e.g. Joachimi & Schneider, 2010), or cross-correlating different probes, such as weak lensing and galaxy clustering (Bernstein, 2009; Zhang, 2010).

Lastly, I have shown how one could constrain the gravitational slip Ψ/Φ using only the pure ellipticity–signal from Euclid; in an admittedly artificial proof of concept, the degeneration shows to be the same of at least one other probe, namely Planck (Planck Collaboration, 2015). The advantage of this approach would be that one gets the information about the Weyl and Newtonian potentials directly from the same source and doesn't have to go through assumptions that might go in other probes. One rather large deficit here is, however, that the intrinsic alignment signal is purely sourced by the tidal shear model and furthermore that its amplitude variable D is known exactly – also, the separation of the sample into red and blue galaxies might be rather dicey. However, both of this can be mitigated by using any other alignment model (that depends on the gravitational

potential). Whether a model like the one presented in Blazek et al. (2017), where all galaxies apparently feel the magnitude of the Newtonian potential, is up for debate. Furthermore, a more computationally elaborate study could find how sensitive this method is to the k–dependence of η and μ, as I expect that to a be great asset of this approach: it probes both large–scale and small–scale interactions of both the Newtonian potential Φ as well as the Weyl potential $\Phi + \Psi$. In redshift space distortions, for example, only very small scale interactions between the Newtonian potantial is probed.

The next step for the here presented alignment model would be to find out what a GI–alignment for spirals could look like, as the three-point correlator contains one potentially non–Gaussian field. Another open question within this framework would be the cross-correlation between spirals and ellipticals. Furthermore, the validity of the Gaussianity–based investigations (the biased likelihoods and the shape of the Fisher–matrices) should be reproduced by Monte–Carlo Markov–chain runs, which hopefully will confirm the general predictions made here.

It would also be helpful to understand exactly how well a galaxy sample such as Euclid's could reliably be separated into ellipticals and spirals, or rather red and blue galaxies, and if the tradeoff with the statistical error is worth the effort, or if just fitting nuisance parameters is equivalent or even better in terms of statistical significance for inferring a cosmological parameter set. Maybe a mock observation/separation from large simulations with reliable baryonic physics (such as IllustrisTNG) could be attempted in order to assess the quality of separation of galaxies using rather incomplete photometric redshift information.

Intrinsic alignments have only been studied for a relatively short amount of time and there seems to be an ever–growing forest of models for them. I'm confident that, just like other sources of noise in people's data in the past, they will soon become a source of information about galaxy formation and evolution and the statistical properties of the large scale structure. Whether they can be modelled perfectly enough to probe Einstein's theory remains to be seen.

Part III

Appendix

A Derivation of the Fisher-Matrix and Estimation Bias

A.1 Fisher-Matrix

Let the data matrix

$$\mathcal{D} = (\boldsymbol{\theta} - \boldsymbol{\theta}_0)(\boldsymbol{\theta} - \boldsymbol{\theta}_0)^T, \tag{A.1}$$

then

$$2\mathcal{L} = n \ln(2\pi) + \mathrm{tr}\left[\ln(\det C) + C^{-1}\mathcal{D}\right]. \tag{A.2}$$

The first derivative of this is

$$2\,\partial_\mu \mathcal{L} = \mathrm{tr}\left[\partial_\mu(\ln C) + \left(\partial_\mu C^{-1}\right)\mathcal{D} + C^{-1}\partial_\mu \mathcal{D}\right], \tag{A.3}$$

using $\partial_\mu C^{-1} = -C^{-1}\left(\partial_\mu C\right)C^{-1}$,

$$2\partial_\mu \mathcal{L} = \mathrm{tr}\left[C^{-1}\left(\partial_\mu C\right) - C^{-1}\left(\partial_\mu C\right)C^{-1}\mathcal{D} + C^{-1}\partial_\mu \mathcal{D}\right]. \tag{A.4}$$

The second derivative of this should give us the Fisher matrix:

$$\begin{aligned} 2\partial_\mu\partial_\nu \mathcal{L} = \mathrm{tr}\Big[& - C^{-1}\left(\partial_\nu C\right)C^{-1}\left(\partial_\mu C\right) + C^{-1}\left(\partial_\mu\partial_\nu C\right) \\ & + C^{-1}\left\{\left(\partial_\nu C\right)C^{-1}\left(\partial_\mu C\right) + \left(\partial_\nu C\right)C^{-1}\left(\partial_\mu C\right)\right\}C^{-1}\mathcal{D} \\ & - C^{-1}\left\{\left(\partial_\mu C\right)C^{-1}\left(\partial_\nu \mathcal{D}\right) + \left(\partial_\nu C\right)C^{-1}\left(\partial_\mu \mathcal{D}\right)\right\} \\ & + C^{-1}\left(\partial_\mu\partial_\nu C\right)C^{-1}\mathcal{D} + C^{-1}\left(\partial_\mu\partial_\nu \mathcal{D}\right)\Big], \end{aligned} \tag{A.5}$$

which simplifies quickly once we take the expectation value, use the trace identity $\mathrm{tr}\,(AB) = \mathrm{tr}\,(BA)$ and remember that $\langle\mathcal{D}\rangle = C$, $\left\langle\partial_\mu D\right\rangle = 0$ by construction, and setting $\boldsymbol{\theta}_0 = 0$ sets $\left\langle\partial_\mu\partial_\nu D\right\rangle = 0$:

$$F_{ij} = \frac{1}{2}\mathrm{tr}\left[C^{-1}\partial_\mu C\; C^{-1}\partial_\nu C\right]. \tag{A.6}$$

A.2 Parameter Estimation Bias

This section follows the same arguments as Schaefer & Heisenberg (2012). The respective true and false log likelihoods are

$$\mathcal{L}^t \propto \mathrm{tr}\Big[\ln C_t + C_t^{-1}\mathcal{D}\Big], \tag{A.7}$$

and

$$\mathcal{L}^f \propto \mathrm{tr}\Big[\ln C_f + C_f^{-1}\mathcal{D}\Big]. \tag{A.8}$$

Note that the data $\mathcal{D}$ is only measured according to the true model:

$$\langle\mathcal{D}\rangle = C_t \tag{A.9}$$

Now, as the bias is thought to be small, we can find the false log likelihood by expanding the false model around the true maximum, which gives

$$\mathcal{L}^f(\boldsymbol{\theta}^f) = \mathcal{L}^t(\boldsymbol{\theta}^t) + \sum_\mu \partial_\mu \mathcal{L}^f(\boldsymbol{\theta}^t)\delta_\mu + \frac{1}{2}\sum_{\mu,\nu} \partial_\mu\partial_\nu \mathcal{L}^f(\boldsymbol{\theta}^t)\delta_\mu\delta_\nu, \tag{A.10}$$

where the bias vector was defined as $\boldsymbol{\delta} = (\boldsymbol{\theta}_f - \boldsymbol{\theta}_t)$. The best-fitting parameters for the false likelihood can now be found by minimising and ensemble averaging, i.e.

$$\left\langle \partial_\mu \mathcal{L}^f(\boldsymbol{\theta}^t) \right\rangle = -\sum_\nu \left\langle \partial_\mu\partial_\nu \mathcal{L}^f(\boldsymbol{\theta}^t) \right\rangle \delta_\nu. \tag{A.11}$$

Which is a set of linear equations of the form

$$a_\mu = \sum_\nu G_{\mu\nu}\delta_\nu \tag{A.12}$$

Both $\boldsymbol{a}$ and G can be constructed from derivatives of the covariance matrix for the false model and the covariance matrix for the true model (because of equation (A.9)). Since they also have multiplicity $2\ell + 1$, they are sums over ℓ,

$$G_{\mu\nu} = \sum_\ell \frac{2(\ell+1)}{2}\mathrm{tr}\left[\left(C_f^{-1}\left(\partial_\mu\partial_\nu C_f\right)\left(C_f^{-1}C_t - \mathrm{id}\right)\right) - \left(C_f^{-1}\left(\partial_\mu C_f\right)C_f^{-1}\left(\partial_\nu C_f\right)\left(2C_f^{-1}C_t - \mathrm{id}\right)\right)\right], \tag{A.13}$$

and

$$a_\mu = \sum_\ell \frac{2(\ell+1)}{2}\mathrm{tr}\left[C_f^{-1}\left(\partial_\mu C_f\right)\left(\mathrm{id} - C_f^{-1}C_t\right)\right]. \tag{A.14}$$

Since these can in principle be calculated from $C^\gamma(\ell)$ and $C^\gamma(\ell) + C^{\mathrm{e},II}(\ell) + C^{\mathrm{e},GI}(\ell) + C^{\mathrm{s},II}(\ell)$ for C_f and C_t respectively, the bias vector is obtained by

$$\delta_\mu = \sum_\nu G^{-1}_{\mu\nu}a_\nu. \tag{A.15}$$

Plugging in $C_f = C_t$ would make $G_{\mu\nu}$ reduce to the Fisher matrix (equation (3.43)) and would set a_μ to 0.

B Intrinsic Alignment Correlation Functions

B.1 Explicit Calculation of $C_{\alpha\beta\gamma\delta}$ for the Tidal Shear Model

The correlation function is

$$C_{\alpha\beta\gamma\delta}(\boldsymbol{r}) = \left\langle \Phi_{\alpha\beta}(\boldsymbol{x})\Phi_{\gamma\delta}(\boldsymbol{x}+\boldsymbol{r}) \right\rangle, \tag{B.1}$$

Going to Fourier space in order to express $C_{\alpha\beta\gamma\delta}$ in terms of the power spectrum $P(k)$,

$$\begin{aligned} C_{\alpha\beta\gamma\delta}(\boldsymbol{r}) &= \partial_\alpha\partial_\beta\partial_\gamma\partial_\delta \int \frac{\mathrm{d}^3k}{(2\pi)^3} \int \frac{\mathrm{d}^3k'}{(2\pi)^3} \left\langle \hat{\Phi}(\boldsymbol{k})\hat{\Phi}'(\boldsymbol{k}') \right\rangle \mathrm{e}^{-\mathrm{i}\boldsymbol{k}\cdot\boldsymbol{x}}\, \mathrm{e}^{+\mathrm{i}\boldsymbol{k}'\cdot\boldsymbol{x}'} \\ &= \partial_\alpha\partial_\beta\partial_\gamma\partial_\delta \int \frac{\mathrm{d}^3k}{(2\pi)^3} \int \mathrm{d}^3k'\, \delta_\mathrm{D}(\boldsymbol{k}-\boldsymbol{k}') P_\Phi(k) \mathrm{e}^{+\mathrm{i}\boldsymbol{k}'\cdot\boldsymbol{x}'}\, \mathrm{e}^{-\mathrm{i}\boldsymbol{k}\cdot\boldsymbol{x}} \\ &= \partial_\alpha\partial_\beta\partial_\gamma\partial_\delta \int \frac{\mathrm{d}^3k}{(2\pi)^3} P_\Phi(k) \mathrm{e}^{+\mathrm{i}\boldsymbol{k}\cdot\boldsymbol{r}}\,. \end{aligned} \tag{B.2}$$

This can be written in cylindrical coordinates as

$$C_{\alpha\beta\gamma\delta}(\boldsymbol{r}) = \partial_\alpha\partial_\beta\partial_\gamma\partial_\delta \int \frac{k^2\mathrm{d}k}{2\pi^2} j_0(kr) P_\Phi(k), \tag{B.3}$$

where j_0 is the spherical Bessel function.

Re-writing $\partial_\alpha = (\mathrm{d}r/\mathrm{d}x_\alpha)(\mathrm{d}/\mathrm{d}r) = (x_\alpha/r)(\mathrm{d}/\mathrm{d}r)$ and defining $D := (1/r)(\mathrm{d}/\mathrm{d}r)$, we can pull in the first two derivatives into the integral (cf. Crittenden et al. (2001) equation 32)

$$C_{\alpha\beta\gamma\delta}(\boldsymbol{r}) = \partial_\alpha\partial_\beta \int \frac{k^2\mathrm{d}k}{2\pi^2} P_\Phi(k) \left[\partial_\gamma x_\delta D j_0(kr) + x_\gamma x_\delta D^2 j_0(kr) \right]. \tag{B.4}$$

The derivative $\partial_\alpha x_\beta$ can be written as the Kronecker delta $\delta_{\alpha\beta}$. Pulling in the last two derivatives gives four terms:

$$\begin{aligned} C_{\alpha\beta\gamma\delta}(\boldsymbol{r}) = &\left(\delta_{\alpha\beta}\delta_{\gamma\delta} + \delta_{\alpha\gamma}\delta_{\beta\delta} + \delta_{\alpha\delta}\delta_{\beta\gamma}\right) \int \frac{k^2\mathrm{d}k}{2\pi^2} P_\Phi(k) D^2 j_0(kr) \\ &+ \left(\delta_{\alpha\beta}r_\gamma r_\delta + \delta_{\alpha\gamma}r_\beta r_\delta + \delta_{\alpha\delta}r_\beta r_\gamma + \delta_{\beta\gamma}r_\alpha r_\delta + \delta_{\beta\delta}r_\alpha r_\gamma + \delta_{\gamma\delta}r_\alpha r_\beta\right) \int \frac{k^2\mathrm{d}k}{2\pi^2} P_\Phi(k) D^3 j_0(kr) \\ &+ \left(r_\alpha r_\beta r_\gamma r_\delta\right) \int \frac{k^2\mathrm{d}k}{2\pi^2} P_\Phi(k) D^4 j_0(kr). \end{aligned}$$

If we now define

$$\zeta_n(r) = r^{-4} \int \frac{k^2\mathrm{d}k}{2\pi^2} P_\Phi(k) D^n j_0(kr) = \frac{(-1)^n}{r^{4-n}} \int \frac{k^{n+2}\mathrm{d}k}{2\pi^2} P_\Phi(k) j_n(kr), \tag{B.5}$$

where in the last step $D^n j_0(r) = (-1)^n r^{-n} j_n(r)$ was used, which is true by construction of the spherical Bessel functions by Rayleigh's formulas, the correlation becomes, using the normalised $\hat{r}_\alpha = r_\alpha / r$

$$\begin{aligned} C_{\alpha\beta\gamma\delta}(r,\theta) = &\left(\delta_{\alpha\beta}\delta_{\gamma\delta} + \delta_{\alpha\gamma}\delta_{\beta\delta} + \delta_{\alpha\delta}\delta_{\beta\gamma}\right)\zeta_2(r) \\ &+ \left(\delta_{\alpha\beta}\hat{r}_\gamma\hat{r}_\delta + \delta_{\alpha\gamma}\hat{r}_\beta\hat{r}_\delta + \delta_{\alpha\delta}\hat{r}_\beta\hat{r}_\gamma + \delta_{\beta\gamma}\hat{r}_\alpha\hat{r}_\delta + \delta_{\beta\delta}\hat{r}_\alpha\hat{r}_\gamma + \delta_{\gamma\delta}\hat{r}_\alpha\hat{r}_\beta\right)\zeta_3(r) \\ &+ \left(\hat{r}_\alpha\hat{r}_\beta\hat{r}_\gamma\hat{r}_\delta\right)\zeta_4(r). \end{aligned} \tag{B.6}$$

Due to isotropy the vector $\boldsymbol{r}$ can be expressed using just r and α, such that $\boldsymbol{r} = r\,(\sin(\alpha), 0, \cos(\alpha))^T$.

In order to now find the ellipticity correlation functions $\langle \epsilon_a \epsilon_a \rangle$, from equation (4.17), we have

$$\epsilon_+ = D\left(\Phi_{xx} - \Phi_{yy}\right) \quad \text{and} \quad \epsilon_\times = D\,2\Phi_{xy}, \tag{B.7}$$

as well as $\epsilon_\mathrm{s} = D\left(\Phi_{xx} + \Phi_{yy}\right)$, the ellipticity correlations for II-alignment become

$$C^{II}_{ab}(r,\alpha) = \left\langle \epsilon_a\ \epsilon'_b \right\rangle, \quad a,b \in \{+, \times, \mathrm{s}\} \tag{B.8}$$

become

$$\begin{aligned} C^{II}_{++}(r,\alpha) = \langle \epsilon_+ \epsilon'_+ \rangle &= D^2\left(C_{xxxx} - C_{xxyy} - C_{yyxx} + C_{yyyy}\right) \\ &= D^2\left(4\zeta_2(r) + 4\sin^2(\alpha)\zeta_3(r) + \sin^4(\alpha)\zeta_4(r)\right), \end{aligned} \tag{B.9}$$

$$\begin{aligned} C^{II}_{\times\times}(r,\alpha) = \langle \epsilon_\times \epsilon'_\times \rangle &= 4D^2 C_{xyxy} \\ &= 4D^2\left(\zeta_2(r) + \sin^2(\alpha)\zeta_3(r)\right), \end{aligned} \tag{B.10}$$

$$\begin{aligned} C^{II}_{+\times}(r,\alpha) = \langle \epsilon_+ \epsilon'_\times \rangle &= 2D^2\left(C_{xxxy} - C_{yyxy}\right) \\ &= 0, \end{aligned} \tag{B.11}$$

$$\begin{aligned} C^{II}_{\mathrm{ss}}(r,\alpha) = \langle \epsilon_\mathrm{s} \epsilon'_\mathrm{s} \rangle &= D^2\left(C_{xxxx} + C_{xxyy} + C_{yyxx} + C_{yyyy}\right) \\ &= D^2\left(8\zeta_2(r) + 8\sin^2(\alpha)\zeta_3(r) + \sin^4(\alpha)\zeta_4(r)\right), \end{aligned} \tag{B.12}$$

$$\begin{aligned} C^{II}_{\mathrm{s}+}(r,\alpha) = \langle \epsilon_\mathrm{s} \epsilon'_+ \rangle &= D^2\left(C_{xxxx} - C_{xxyy} + C_{yyxx} - C_{yyyy}\right) \\ &= D^2\left(-6\zeta_3(r) - \sin^4(\alpha)\zeta_4(r)\right), \end{aligned} \tag{B.13}$$

$$\begin{aligned} C^{II}_{\mathrm{s}\times}(r,\alpha) = \langle \epsilon_\mathrm{s} \epsilon'_\times \rangle &= 2D^2\left(C_{xxxy} + C_{yyxy}\right) \\ &= 0. \end{aligned} \tag{B.14}$$

For the GI-alignments the spectra are very similar. Remembering that

$$\gamma_+ = \left(\Phi_{yy} - \Phi_{xx}\right) \quad \text{and} \quad \gamma_\times = 2\Phi_{xy}, \tag{B.15}$$

and that equally $\gamma_s = \Phi_{xx} + \Phi_{yy}$ the respective spectra $C_{ab}^{GI}(r,\alpha)$ can easily be found as the $gamma_a$ can easily be re-written as

$$\gamma_+ = -\frac{\epsilon_+}{D} \quad \text{and} \quad \gamma_\times = \frac{\epsilon_\times}{D}. \tag{B.16}$$

This leads to a factor of D instead of D^2 as well as a sign flip whenever γ_+ is involved,

$$\begin{aligned} C_{++}^{GI}(r,\alpha) = \langle \gamma_+ \epsilon'_+ \rangle &= -D\Big(C_{xxxx} - C_{xxyy} - C_{yyxx} + C_{yyyy}\Big) \\ &= -D\Big(4\zeta_2(r) + 4\sin^2(\alpha)\zeta_3(r) + \sin^4(\alpha)\zeta_4(r)\Big), \end{aligned} \tag{B.17}$$

$$\begin{aligned} C_{\times\times}^{GI}(r,\alpha) = \langle \gamma_\times \epsilon'_\times \rangle &= 4DC_{xyxy} \\ &= 4D\Big(\zeta_2(r) + \sin^2(\alpha)\zeta_3(r)\Big), \end{aligned} \tag{B.18}$$

$$\begin{aligned} C_{+\times}^{GI}(r,\alpha) = \langle \gamma_+ \epsilon'_\times \rangle &= -2D\Big(C_{xxxy} - C_{yyxy}\Big) \\ &= 0, \end{aligned} \tag{B.19}$$

$$\begin{aligned} C_{\mathrm{ss}}^{GI}(r,\alpha) = \langle \gamma_\mathrm{s} \epsilon'_\mathrm{s} \rangle &= D\Big(C_{xxxx} + C_{xxyy} + C_{yyxx} + C_{yyyy}\Big) \\ &= D\Big(8\zeta_2(r) + 8\sin^2(\alpha)\zeta_3(r) + \sin^4(\alpha)\zeta_4(r)\Big), \end{aligned} \tag{B.20}$$

$$\begin{aligned} C_{\mathrm{s}+}^{GI}(r,\alpha) = \langle \gamma_\mathrm{s} \epsilon'_+ \rangle &= -D\Big(C_{xxxx} - C_{xxyy} + C_{yyxx} - C_{yyyy}\Big) \\ &= -D\Big(-6\zeta_3(r) - \sin^4(\alpha)\zeta_4(r)\Big), \end{aligned} \tag{B.21}$$

$$\begin{aligned} C_{\mathrm{s}\times}^{GI}(r,\alpha) = \langle \gamma_\mathrm{s} \epsilon'_\times \rangle &= 2D\Big(C_{xxxy} + C_{yyxy}\Big) \\ &= 0. \end{aligned} \tag{B.22}$$

The same exercise can be done for the tidal torque model, but there the correlations become much more complicated as the ellipticities are quadratic in $\hat{\Phi}_{\alpha\beta}$, such that the correlations end up with higher orders of ζ_n and a normalisation due to the dependence on the normalised potential.

B.2 $C_{\alpha\beta\gamma\delta}$ for the Tidal Torque Model

The two point correlation function,

$$\begin{aligned} \Big\langle \Phi_{\alpha\beta}(\boldsymbol{x})\Phi_{\gamma\delta}(\boldsymbol{x'}) \Big\rangle = C_{\alpha\beta\gamma\delta}(r) = &\Big(\delta_{\alpha\beta}\delta_{\gamma\delta} + \delta_{\alpha\gamma}\delta_{\beta\delta} + \delta_{\alpha\delta}\delta_{\beta\gamma}\Big)\zeta_2(r) \\ &+ \Big(\delta_{\alpha\beta}\hat{r}_\gamma\hat{r}_\delta + \delta_{\alpha\gamma}\hat{r}_\beta\hat{r}_\delta + \delta_{\alpha\delta}\hat{r}_\beta\hat{r}_\gamma + \delta_{\beta\gamma}\hat{r}_\alpha\hat{r}_\delta + \delta_{\beta\delta}\hat{r}_\alpha\hat{r}_\gamma + \delta_{\gamma\delta}\hat{r}_\alpha\hat{r}_\beta\Big)\zeta_3(r) \\ &+ \Big(\hat{r}_\alpha\hat{r}_\beta\hat{r}_\gamma\hat{r}_\delta\Big)\zeta_4(r), \end{aligned} \tag{B.23}$$

is the base for the traceless tidal shear correlation function $\tilde{\Phi}_{\alpha\beta} = \Phi_{\alpha\beta} - \delta_{\alpha\beta}\nabla^2\Phi/3$ (Schaefer & Merkel, 2015):

$$\begin{aligned}\tilde{C}_{\alpha\beta\gamma\delta}(r) = C_{\alpha\beta\gamma\delta}(r)&\\ &- \frac{1}{3}\left(\delta_{\gamma\delta}\left(5\zeta_2(r) + \zeta_3(r)\right) + \hat{r}_\gamma\hat{r}_\delta\left(7\zeta_3(r) + \zeta_4(r)\right)\right)\delta_{\alpha\beta}\\ &- \frac{1}{3}\left(\delta_{\alpha\beta}\left(5\zeta_2(r) + \zeta_3(r)\right) + \hat{r}_\alpha\hat{r}_\beta\left(7\zeta_3(r) + \zeta_4(r)\right)\right)\delta_{\gamma\delta}\\ &+ \frac{1}{9}\left(15\zeta_2(r) + 10\zeta_3(r) + \zeta_4(r)\right)\delta_{\alpha\beta}\delta_{\gamma\delta}. \end{aligned} \tag{B.24}$$

The ζ-functions are the same as in the previous section. Since the tidal torque model is dependent on the square of the tidal shear, the correlations will end up being four-point correlators (Crittenden et al., 2001), but can be expressed with help of the Wick-theorem (which also implicitly needs Gaussianity) as

$$\left\langle\hat{\Phi}_A(\boldsymbol{x})\hat{\Phi}_B(\boldsymbol{x})\,\hat{\Phi}_C(\boldsymbol{x}')\hat{\Phi}'_D(\boldsymbol{x}')\right\rangle = \frac{1}{(14\zeta_2(0))^2}\left(\tilde{C}_{AC}\tilde{C}_{BD} + \tilde{C}_{AD}\tilde{C}_{BC}\right), \tag{B.25}$$

where the letters indicate pairs of indices. Now the four non-zero correlation functions of the ellipticities as defined in section 4.2, one arrives at the non-zero correlations (Schaefer & Merkel, 2015):

$$\langle\epsilon_+\epsilon'_+\rangle = \frac{1}{144}\left(\frac{A\alpha}{14\zeta_2}\right)^2\left(A_{++}\cos(4\alpha) + B_{++}\cos(2\alpha) + C_{++}\right), \tag{B.26}$$

$$\langle\epsilon_\times\epsilon'_\times\rangle = \frac{1}{18}\left(\frac{A\alpha}{14\zeta_2}\right)^2\left(B_{\times\times}\cos(2\alpha) + C_{\times\times}\right), \tag{B.27}$$

$$\langle\epsilon_+\epsilon_s\rangle = \frac{1}{324}\left(\frac{A\alpha}{14\zeta_2}\right)^2\left(A_{+s}\cos(4\alpha) + B_{+s}\cos(2\alpha) + C_{+s}\right), \tag{B.28}$$

$$\langle\epsilon_s\epsilon_s\rangle = \frac{1}{108}\left(\frac{A\alpha}{14\zeta_2}\right)^2\left(A_{ss}\cos(4\alpha) + B_{ss}\cos(2\alpha) + C_{ss}\right). \tag{B.29}$$

with the lengthy summands

$$A_{++} = \zeta_4^2 + 6(\zeta_3 + \zeta_2)\zeta_4 + 17\zeta_3^2, \tag{B.30}$$

$$B_{++} = -4\zeta_4^2 - 32\zeta_3\zeta_4 - 28\zeta_3^2 + 72\zeta_2\zeta_3, \tag{B.31}$$

$$C_{++} = 3\zeta_4^2 + (26\zeta_3 + 58\zeta_2)\zeta_4 + 155\zeta_3^2 + 472\zeta_2\zeta_3 + 336\zeta_2^2, \tag{B.32}$$

$$A_{\times\times} = 0 \tag{B.33}$$

$$B_{\times\times} = (\zeta_3 - 3\zeta_2)\zeta_4 - 5\zeta_3^2 - 9\zeta_2\zeta_3, \tag{B.34}$$

$$C_{\times\times} = (-\zeta_3 - 5\zeta_2)\zeta_4 - 13\zeta_3^2 - 59\zeta_2\zeta_3 - 42\zeta_2^2, \tag{B.35}$$

$$A_{+s} = -3\zeta_4^2 + 18(\zeta_3 + \zeta_2)\zeta_4 + 51\zeta_3^2, \tag{B.36}$$

$$B_{+s} = 4\zeta_4^2 + (32\zeta_3 + 48\zeta_2)\zeta_4 + 172\zeta_3^2 + 408\zeta_2\zeta_3, \tag{B.37}$$

$$C_{+s} = 7\zeta_4^2 + (-50\zeta_3 - 66\zeta_2)\zeta_4 - 233\zeta_3^2 - 408\zeta_2\zeta_3, \tag{B.38}$$

$$A_{ss} = 9\zeta_4^2 + (54\zeta_3 + 54\zeta_2)\zeta_4 + 153\zeta_3^2, \tag{B.39}$$

$$B_{ss} = 60\zeta_4^2 + (480\zeta_3 + 288\zeta_2)\zeta_4 + 1284\zeta_3^2 + 1800\zeta_2\zeta_3, \tag{B.40}$$

$$C_{ss} = 59\zeta_4^2 + (490\zeta_3 + 426\zeta_2)\zeta_4 + 1907\zeta_3^2 + 3864\zeta_2\zeta_3 + 2448\zeta_2^2. \tag{B.41}$$

List of Figures

List of Tables

Bibliography

Abbott et mult. B. P., 2016, Phys. Rev. Lett., 116, 061102

Adamek J., Daverio D., Durrer R., Kunz M., 2013, Physical Review D, 88, 103527

Aghanim N., Majumdar S., Silk J., 2008, Reports on Progress in Physics, 71, 066902

Aharonian et mult. F., 2013, preprint, (arXiv:1301.4124)

Amara A., Réfrégier A., 2008, MNRAS, 391, 228

Amendola L., Tsujikawa S., 2010, Dark energy. Cambridge University Press, Cambridge

Amendola L., Kunz M., Sapone D., 2008, Journal of Cosmology and Astroparticle Physics, 4, 013

Aprile et mult. E., 2017, Phys. Rev. Lett., 119, 181301

Bacon D. J., Schaefer B. M., 2009, Monthly Notices of the Royal Astronomical Society, 396, 2167

Bardeen J. M., 1980, Phys. Rev. D, 22, 1882

Bardeen J. M., Bond J. R., Kaiser N., Szalay A. S., 1986, Astrophysical Journal, 304, 15

Bartelmann M., 2010, Reviews of Modern Physics, 82, 331

Bartelmann M., Maturi M., 2017, Scholarpedia, 12, 32440

Bartelmann M., Schneider P., 2001a, Physics Reports, 340, 291

Bartelmann M., Schneider P., 2001b, Phys.Rept., 340, 291

Bartelmann M., Fabis F., Berg D., Kozlikin E., Lilow R., Viermann C., 2016, New Journal of Physics, 18, 043020

Baumann D., 2007, preprint, (arXiv:0710.3187)

Bellini E., Sawicki I., 2014, Journal of Cosmology and Astroparticle Physics, 7, 050

Bernstein G. M., 2009, ApJ, 695, 652

Blake C., et al., 2016, Monthly Notices of the Royal Astronomical Society, 456, 2806

Blas D., Garny M., Ivanov M. M., Sibiryakov S., 2016, JCAP, 1607, 052

Blazek J., McQuinn M., Seljak U., 2011, JCAP, 2011, 010

Blazek J., Vlah Z., Seljak U., 2015, JCAP, 08, 15

Blazek J., MacCrann N., Troxel M. A., Fang X., 2017, ArXiv e-prints 1708.09247

Blumenthal G. R., Faber S. M., Primack J. R., Rees M. J., 1984, Nature, 311, 517 EP

Bradač M., Lombardi M., Schneider P., 2004, Astronomy and Astrophysics, 424, 13

Brown M. L., Battye R. A., , Monthly Notices of the Royal Astronomical Society, 410, 2057

Brown M., et al., 2015, Advancing Astrophysics with the Square Kilometre Array (AASKA14), p. 23

Camelio G., Lombardi M., 2015, Astronomy and Astrophysics, 575, A113

Capranico F., Merkel P. M., Schaefer B. M., 2013, MNRAS, 435, 194

Catelan P., Kamionkowski M., Blandford R. D., 2001, MNRAS, 320, L7

Chiara Guzzetti M., Bartolo N., Liguori M., Matarrese S., 2016, preprint, (arXiv:1605.01615)

Clowe D., Bradac M., Gonzalez A. H., Markevitch M., Randall S. W., et al., 2006, Astrophys.J., 648, L109

Conselice C. J., 2014, Annual Review of Astronomy and Astrophysics, 52, 291

Crittenden R. G., Natarajan P., Pen U.-L., Theuns T., 2001, ApJ, 559, 552

Crittenden R. G., Natarajan P., Pen U.-L., Theuns T., 2002, ApJ, 568, 20

Davis M., Efstathiou G., Frenk C. S., White S. D. M., 1985, Astrophysical Journal, 292, 371

Dicke R. H., Peebles P. J. E., Roll P. G., Wilkinson D. T., 1965, Astrophysical Journal, 142, 414

Dodelson S., 2006, Modern cosmology, 4. [print.] edn. Academic Press, Amsterdam

Doroshkevich A. G., 1970, Astrofizika, 6, 581

Dressler A., et al., 1997, Astrophysical Journal, 490, 577

Durrer R., 2008, The Cosmic Microwave Background. Cambridge University Press, doi:10.1017/CBO9780511817205

Dvornik A., et al., 2018

Dyer C. C., Shaver E. G., 1992, Astrophysical Journal Letters, 390, L5

Dyson F. W., Eddington A. S., Davidson C., 1920, Royal Society of London Philosophical Transactions Series A, 220, 291

Einstein A., 1911, Annalen der Physik, 340, 898

Einstein A., 1915, Sitzungsberichte der Königlich Preußischen Akademie der Wissenschaften (Berlin), Seite 844-847.,

Einstein A., 1916, Annalen der Physik, 354, 769

Einstein A., 1917, in Sitzungsberichte der Königlich-Preußischen Akademie der Wissenschaften. pp 142–152

Falco E. E., Gorenstein M. V., Shapiro I. I., 1985, Astrophysical Journal Letters, 289, L1

Faraoni V., 1993, Astronomy and Astrophysics, 272, 385

Finlay-Freundlich E., 1954, The London, Edinburgh, and Dublin Philosophical Magazine and Journal of Science, 45, 303

Friedmann A., 1922, Zeitschrift fur Physik, 10, 377

Gamow G., 1961, The creation of the universe.

Giahi-Saravani A., Schaefer B. M., 2014, MNRAS, 437, 1847

Gott III J. R., Colley W. N., 2017, preprint, (arXiv:1707.06755)

Grützbauch R., Conselice C. J., Varela J., Bundy K., Cooper M. C., Skibba R., Willmer C. N. A., 2011, Monthly Notices of the Royal Astronomical Society, 411, 929

Guth A. H., 1981, Phys. Rev. D, 23, 347

Hao J., Kubo J. M., Feldmann R., Annis J., Johnston D. E., Lin H., McKay T. A., 2011, ApJ, 740, 39

Harrison I., Camera S., Zuntz J., Brown M. L., 2016, Monthly Notices of the Royal Astronomical Society, 463, 3674

Hentschel K., 1994, Archive for History of Exact Sciences, 47, 143

Heymans C., Heavens A., 2003, MNRAS, 339, 711

Heymans C., et al., 2013, MNRAS, 432, 2433

Hilbert S., Xu D., Schneider P., Springel V., Vogelsberger M., Hernquist L., 2016, MNRAS, 468, 790

Hirata C. M., Seljak U., 2004, PRD, 70, 063526

Horndeski G. W., 1974, International Journal of Theoretical Physics, 10, 363

Hu W., 1999, ApJL, 522, L21

Hubble E., 1926, Contributions from the Mount Wilson Observatory / Carnegie Institution of Washington, 324, 1

Hubble E., 1929, Proceedings of the National Academy of Science, 15, 168

Joachimi B., Schneider P., 2010, ArXiv e-prints 1009.2024

Joachimi B., Mandelbaum R., Abdalla F. B., Bridle S. L., 2011, A & A, 527, A26

Joudaki S., et al., 2016, ArXiv e-prints 1610.04606,

Kaiser N., 1992, Astrophysical Journal, 388, 272

Kaiser N., Squires G., Broadhurst T., 1995, Astrophysical Journal, 449, 460

Kamionkowski M., Kosowsky A., Stebbins A., 1997, Phys. Rev., D55, 7368

Kass R. E., Raftery A. E., 1995, Journal of the American Statistical Association, 90, 773

Kiessling A., et al., 2015a, preprint, (arXiv:1504.05546)

Kiessling A., et al., 2015b, Space Science Reviews, 193, 67

King L., Schneider P., 2002, A & A, 396, 411

Kirk D., Bridle S., Schneider M., 2010, MNRAS, 408, 1502

Kullback S., Leibler R. A., 1951, Ann. Math. Statist., 22, 79

Larsen P., Challinor A., 2016, MNRAS, 461, 4343

Laureijs R., et al., 2011, ArXiv e-prints 1110.3193

Lee J., Pen U., 2000, ApJL, 532, L5

Lee J., Pen U.-L., 2001, ApJ, 555, 106

Lemaître G., 1927, Annales de la Societe Scietifique de Bruxelles, 47, 49

Libeskind N. I., Hoffman Y., Steinmetz M., Gottloeber S., Knebe A., Hess S., 2013, ApJL, 766

Liddle A. R., 1999, in Masiero A., Senjanovic G., Smirnov A., eds, High Energy Physics and Cosmology, 1998 Summer School. p. 260 (arXiv:astro-ph/9901124)

Limber D. N., 1954, ApJ, 119, 655

Linder E. V., Jenkins A., 2003, Monthly Notices of the Royal Astronomical Society, 346, 573

Lovelock D., 1971, Journal of Mathematical Physics, 12, 498

Lovelock D., 1972, Journal of Mathematical Physics, 13, 874

Loverde M., Afshordi N., 2008, PRD, 78, 123506

Maldacena J., 2003, Journal of High Energy Physics, 5, 013

McIntosh D. H., et al., 2014, Mon. Not. Roy. Astron. Soc., 442, 533

Menanteau F., et al., 2012, Astrophysical Journal, 748, 7

Miller L., Kitching T. D., Heymans C., Heavens A. F., van Waerbeke L., 2007, Monthly Notices of the Royal Astronomical Society, 382, 315

Natarajan P., Crittenden R. G., Pen U.-L., Theuns T., 2001, PASA, 18, 198

Navarro J. F., Frenk C. S., White S. D. M., 1996, Astrophysical Journal, 462, 563

Nesseris S., Garcia-Bellido J., 2013, JCAP, 2013, 036

Oesch P. A., et al., 2016, The Astrophysical Journal, 819, 129

Peacock J. A., 2003, Cosmological physics, repr. (with corr.) edn. Cambridge Univ. Press, Cambridge

Peebles P. J. E., 1969, Astrophysical Journal, 155, 393

Penzias A. A., Wilson R. W., 1965, Astrophys. J., 142, 419

Perlmutter S., et al., 1999, Astrophys. J., 517, 565

Pillepich A., et al., 2018, Monthly Notices of the Royal Astronomical Society, 475, 648

Piras D., Joachimi B., Schäfer B. M., Bonamigo M., Hilbert S., van Uitert E., 2017, ArXiv e-prints 1707.06559

Planck Collaboration 2013, arXiv:1303.5062,

Planck Collaboration 2015, preprint, (arXiv:1502.01590)

Planck Collaboration Ade et mult. P. A. R., 2016a, Astronomy and Astrophysics, 594, A13

Planck Collaboration Ade et mult. P. A. R., 2016b, Astronomy and Astrophysics, 594, A17

Pritchard J. R., Loeb A., 2012, Reports on Progress in Physics, 75, 086901

Ratra B., Peebles P. J. E., 1988, Phys. Rev. D, 37, 3406

Rees M. J., Sciama D. W., 1968, Nature, 217, 511 EP

Refregier A., Bacon D., 2003, Monthly Notices of the Royal Astronomical Society, 338, 48

Regener E., 1933, Zeitschrift für Physik, 80, 666

Riess A. G., et al., 1998, Astron. J., 116, 1009

Robertson H. P., 1935, Astrophysical Journal, 82, 284

Rubin V. C., Ford Jr. W. K., 1970, Astrophys. J., 159, 379

Saltas I. D., Sawicki I., Amendola L., Kunz M., 2014, Physical Review Letters, 113, 191101

Schaefer B. M., 2009, IJMPD, 18, 173

Schaefer B. M., Heisenberg L., 2012, MNRAS, 423, 3445

Schaefer B. M., Merkel P. M., 2015, ArXiv e-prints 1506.07366

Schaefer B. M., Reischke R., 2016, Monthly Notices of the Royal Astronomical Society, 460, 3398

Schneider P., 2015, Extragalactic astronomy and cosmology, 2. ed. edn. Springer, Berlin ; Heidelberg [u.a.]

Schneider P., Kilbinger M., 2007, Astronomy and Astrophysics, 462, 841

Schwarzschild K., 1916, Abh. Konigl. Preuss. Akad. Wissenschaften Jahre 1906, 92, Berlin, 1907, pp 189–196

Seitz C., Schneider P., 1997, Astronomy and Astrophysics, 318, 687

Sellentin E., 2015, Monthly Notices of the Royal Astronomical Society, 453, 893

Shapiro I. I., 1964, Phys. Rev. Lett., 13, 789

Simpson F., et al., 2013, Mon. Not. Roy. Astron. Soc., 429, 2249

Smith R. E., et al., 2003, MNRAS, 341, 1311

Springel V., et al., 2005, Nature, 435, 629

Springel V., et al., 2018, Monthly Notices of the Royal Astronomical Society, 475, 676

Stebbins A., 1996, ArXiv Astrophysics e-prints,

Sunyaev R. A., Zeldovich Y. B., 1970, Astrophysics and Space Science, 7, 3

Sunyaev R. A., Zeldovich I. B., 1980, Annual Review of Astronomy and Astrophysics, 18, 537

Taburet N., Aghanim N., Douspis M., Langer M., 2009, MNRAS, 392, 1153

Takada M., Jain B., 2004, Monthly Notices of the Royal Astronomical Society, 348, 897

Takada M., White M., 2004, Astrophysical Journal Letters, 601, L1

Tasca et mult. L. A. M., 2009, Astronomy and Astrophysics, 503, 379

Tegmark M., Taylor A., Heavens A., 1997, Astrophys.J., 480, 22

Teklu A. F., Remus R.-S., Dolag K., Beck A. M., Burkert A., Schmidt A. S., Schulze F., Steinborn L. K., 2015, Astrophysical Journal, 812, 29

Tenneti A., Mandelbaum R., Di Matteo T., 2016, Monthly Notices of the Royal Astronomical Society, 462, 2668

Theuns T., Catelan P., 1997, in Persic M., Salucci P., eds, Astronomical Society of the Pacific Conference Series Vol. 117, Dark and Visible Matter in Galaxies and Cosmological Implications. pp 431–+

Tojeiro R., et al., 2013, Monthly Notices of the Royal Astronomical Society, 432, 359

Tugendhat T. M., Schaefer B. M., 2018, Monthly Notices of the Royal Astronomical Society, p. sty323

Tugendhat T. M., Reischke R., Schaefer B. M., 2018, in prep.

Tyson J. A., Valdes F., Wenk R. A., 1990, Astrophysical Journal Letters, 349, L1

Viola M., Melchior P., Bartelmann M., 2011, Monthly Notices of the Royal Astronomical Society, 410, 2156

Walker A. G., 1937, Proceedings of the London Mathematical Society, s2-42, 90

Walsh D., Carswell R. F., Weymann R. J., 1979, Nature, 279, 381 EP

Weller J., Frieman J., Lahav O., Ma Z., 2008, Proceedings of Cosmology, Galaxy Formation and Astroparticle Physics on the Pathway to the SKA, HR Klöckner editor

Wetterich C., 1988, Nuclear Physics B, 302, 668

White S. D. M., 1984, ApJ, 286, 38

Yanagisawa C., 2014, Frontiers in Physics, 2, 30

Zahn O., Zaldarriaga M., 2006, The Astrophysical Journal, 653, 922

Zel'dovich Y. B., 1970, Astronomy and Astrophysics, 5, 84

Zhang P., 2010, MNRAS, 406, L95

Zwicky F., 1933, Helvetica Physica Acta, 6, 110

von Hoerner S., 1960, Z. Astrophys., 50

von Hoerner S., 1963, Z. Astrophys., 57

von Soldner J. G., 1804, Berliner Astronomisches Jahrbuch, Jahrgang 29, 161

Acknowledgements

This past decade of physics in will be the time which I will most fondly look back on in my life.
I have many kind people to thank for their love, time, skill, company, patience, and trust.
First and foremost, Björn Schäfer: Thank you for absolutely everything, including all of the above. You opened all the doors you could for me and kept your own door open most of all.
During my time as a PhD student, I received financial support from a stipend of the Astronomische Rechen-Institut, for which I am very grateful.
I am very grateful to Volker Springel for agreeing to be in my IMPRS committee and for taking it upon himself to be referee for both this thesis and the exam, and for his patience.
Selim Jochim and Peter Bachert, thank you for completing my thesis committee.
Thanks to Martin Kunz for being my supervisor during the time in Geneva.
I owe gratitude to my friend Robert Reischke for supplying the CMB– and BAO–priors used in this work and for many discussions.
I am deeply thankful for the company of everyone with whom I had the fortune to share an office or workspace in the last 6 years: Korbinian Huber and Steffen Hagstotz, who knew that office 219 is a mindset rather than a mere room. I hope some of this 219 experience I could share in office 210 with Johannes Schwinn and Michael Kretschmer, Lennart Kiehl, Philipp Umstätter, Santiago Casas (in Geneva), Dennis Chia among others.
A general thank you goes to my friends Christian Angrick, Jonas Frings, Robert Lilow, Carsten Littek, Elena Kozlikin, Celia Viermann, Felix Fabis, Matthias Bartelmann, Anna Zacheus.

"I should like to say two things. One intellectual and one moral. The intellectual thing I should want to say to them is this:
'When you are studying any matter, or considering any philosophy, ask yourself only: What are the facts, and what is the truth that the facts bear out. Never let yourself be diverted, either by what you wish to believe, or by what you think would have beneficent social effects if it were believed; but look only and solely at what are the facts.'
That is the intellectual thing that I should wish to say. The moral thing I should wish to say to them is very simple; I should say:
'Love is wise – Hatred is foolish.'
In this world, which is getting more and more closely interconnected, we have to learn to tolerate each other. We have to learn to put up with the fact, that some people say things we don't like. We can only live together in that way. But if we are to live together, and not die together, we must learn a kind of charity and a kind of tolerance which is absolutely vital, to the continuation of human life on this planet."

Betrand Russell, 1959,
responding to the question what advice he would leave future generations in a BBC interview.